

EMISSION CHARACTERISTICS OF A LIQUID SPRAY SUDDEN EXPANSION  
COMBUSTOR USING COMPUTATIONAL FLUID DYNAMICS

by

Daniel Rodriguez

A Thesis Submitted to the Faculty of  
The College of Engineering and Computer Science  
in Partial Fulfillment of the Requirements for the Degree of  
Master of Science

Florida Atlantic University

Boca Raton, Florida

August 2013

EMISSION CHARACTERISTICS OF A LIQUID SPRAY SUDDEN EXPANSION  
COMBUSTOR USING COMPUTATIONAL FLUID DYNAMICS

by

Daniel Rodriguez

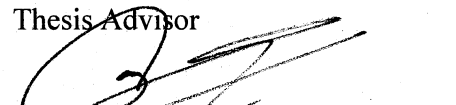
This thesis was prepared under the direction of the candidate's thesis advisor, Dr. Davood Moslemian, Department of Ocean and Mechanical Engineering, and has been approved by the members of his supervisory committee. It was submitted to the faculty of the College of Engineering and Computer Science and was accepted in partial fulfillment of the requirements for the degree of Master of Science.

SUPERVISORY COMMITTEE:

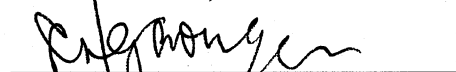


Davood Moslemian, Ph.D.

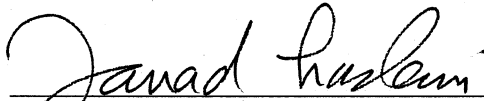
Thesis Advisor



Chaouki Ghenaï, Ph.D.



Gopal Gaonkar, Ph.D.



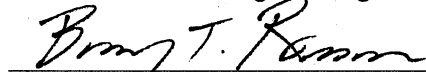
Javad Hashemi, Ph.D.

Chair, Department of Ocean and Mechanical Engineering



Mohammad Ilyas, Ph.D.

Interim Dean, College of Engineering and Computer Science



Barry T. Rosson, Ph.D.

Dean, Graduate College

July 18, 2013  
Date

## ACKNOWLEDGEMENTS

I would like to take some time to thank the wonderful people in my life who have made this thesis possible. I would first like to thank Dr. Davood Moslemian for introducing me to the fascinating world of gas turbine engines, and for directing my thesis. Dr. Moslemian spent a lot of time helping me complete this thesis and I could not have done it without him. I am looking forward to working with him on future research endeavors.

I would also like to thank Dr. Marco Egoavil and Richard Puster for their assistance with completing this research. Their years of experience in the field of combustion were invaluable to the completion of the project, and I appreciate them taking the time to answer my questions. A special thanks also goes to Dr. Ghenai and Dr. Gaonkar for their support and participation as members on my thesis supervisory committee.

I had many colleagues who helped me in the graduate program at FAU. Among them, I would like to acknowledge Rammone Bartlett for helping me become an effective teaching assistant. I would also like to thank Arturo Betancourt and Isabel Portal for constructive comments in writing and defending my thesis.

The College of Engineering and Computer Science has provided me with funding for my master's degree. This funding has given me a chance at higher education and has made me a better person overall. For this, I am grateful.

## ABSTRACT

Author: Daniel Rodriguez

Title: Emission Characteristics of a Liquid Spray Sudden Expansion Combustor Using Computational Fluid Dynamics

Institution: Florida Atlantic University

Thesis Advisor: Dr. Davood Moslemian

Degree: Master of Science

Year: 2013

A sudden expansion combustor (SUE) is analyzed using computation fluid dynamics (CFD). CO emissions and NO<sub>x</sub> emissions are computed for various operating conditions of the SUE combustor using a can type and an annular type geometrical configurations. The goal of this thesis is to see if the SUE combustor is a viable alternative to conventional combustors which utilize swirlers. It is found that for the can type combustor the NO<sub>x</sub> emissions were quite low compared to other combustor types but the CO emissions were fairly high. The annular combustor shows better CO emissions compared to the can type, but the CO emissions are still high compared to other combustors. Emissions can be improved by providing better mixing in the primary combustion zone. The SUE combustor design needs to be further refined in order for it to be a viable alternative to conventional combustors with swirlers.

## DEDICATION

Learning about, and eventually conducting research in chemically reacting turbulent multiphase flow has required the vast majority of my time over the past two years. Over these two years, I have not spent as much time with my family as I would have liked. All the while, they have been very supportive, and very patient. Dedicating my thesis to them is how I can show my gratitude.

EMISSION CHARACTERISTICS OF A LIQUID SPRAY SUDDEN EXPANSION  
COMBUSTOR USING COMPUTATIONAL FLUID DYNAMICS

LIST OF TABLES .....	vii
LIST OF FIGURES .....	viii
1. INTRODUCTION .....	1
2. BACKGROUND THEORY .....	5
2.1 Turbulence Modeling.....	5
2.2 Combustion Fundamentals.....	11
2.3 Turbulent Combustion Modeling.....	17
2.4 Discrete Phase Modeling .....	21
2.5 Radiation Modeling .....	28
2.6 Pollutant Formation .....	30
2.7 Compressibility Effects and Performance Parameters.....	32
2.8 Combustor Fundamentals .....	34
2.9 Solver Theory.....	36
2.10 Literature Review.....	38
3. GEOMETRY, MESH, AND BOUNDARY CONDITIONS .....	44

3.1 Geometry.....	44
3.2 Mesh.....	49
3.3 Boundary Conditions .....	53
4. RESULTS .....	57
4.1 Reacting Flow Fields of the Can Type and Annular Type Combustors .....	57
4.2 Comparison of Results for Various Models.....	76
4.3 Results of the Parametric Study .....	82
5. CONCLUSIONS AND RECCOMENDATIONS .....	91
REFERENCES .....	93

## LIST OF TABLES

Table 1: Boundary conditions common to both combustors .....	54
Table 2: Can Type Combustor Inlet Velocities .....	56
Table 3: Annular type Combustor inlet velocities .....	56
Table 4: Comparison between annular type combustor and can type combustor for an operating pressure of 300 psi (20.7 bar) and a global equivalence ratio of 0.7 ....	75
Table 5: Summary of results from various models .....	82



## LIST OF FIGURES

Figure 1: SUE Can Combustor .....	2
Figure 2: Diagram of a plain-orifice atomizer .....	22
Figure 3: Prefilming airblast atomizer .....	23
Figure 4: Conventional can combustor .....	34
Figure 5: Conventional annular combustor.....	35
Figure 6: Primary combustion zone for can type combustor .....	44
Figure 7: Can combustor picture showing the dilution holes and primary air slot.....	45
Figure 8: Backside of can combustor.....	46
Figure 9: Scale drawing of the can type combustor.....	46
Figure 10: Side view of liquid droplet trajectories .....	47
Figure 11: Downstream view of droplet trajectories .....	47
Figure 12: Annular combustor isometric view .....	47
Figure 13: Annular combustor side view.....	47
Figure 14: Scale drawing of the annular type combustor .....	48
Figure 15: Annular combustor fuel injection arrangement.....	48
Figure 16: Can combustor mesh side view .....	49

Figure 17: Contours of velocity magnitude depicting mesh independence for the can type combustor.....	50
Figure 18: Contours of temperature depicting mesh independence for the can type combustor.....	51
Figure 19: Annular combustor mesh.....	52
Figure 20: Contours of velocity magnitude depicting mesh independence for the annular type combustor.....	52
Figure 21: Contours of temperature depicting mesh independence for the annular type combustor.....	53
Figure 22: Fuel injection diagram.....	55
Figure 23: Contours of velocity magnitude for both combustors. ....	58
Figure 24: Vector field colored by velocity magnitude .....	59
Figure 25: Primary zone velocity vectors. ....	60
Figure 26: Contours of turbulent kinetic energy.....	61
Figure 27: Vector field for cooling vanes. ....	62
Figure 28: Contours of local equivalence ratio.....	63
Figure 29: Iso-surface of equivalence ratio equal to unity. ....	64
Figure 30: Contours of $C_{12}H_{23}$ mass fraction. ....	65
Figure 31: Contours of temperature.....	67
Figure 32: Temperature contours of the full can type combustor.....	68
Figure 33: Fuel droplet residence time .....	69

Figure 34: Contours of O <sub>2</sub> mass fraction.....	70
Figure 35: Contours of CO. ....	71
Figure 36: Contours of dry NO <sub>x</sub> .....	72
Figure 37: Contours of dry NO <sub>x</sub> concentrations (ppm) with an iso-surface of equivalence ratio equal to unity .....	73
Figure 38: Contours of CO <sub>2</sub> mass fraction.....	74
Figure 39: Contours of H <sub>2</sub> O mass fraction. ....	75
Figure 40: Contours of temperature for the eddy dissipation model. ....	78
Figure 41: Contours of NO <sub>x</sub> concentration for the eddy dissipation model. ....	79
Figure 42: Temperature contours for the RSM model.....	80
Figure 43: Contours of NO <sub>x</sub> concentration for the RSM model. ....	81
Figure 44: NO <sub>x</sub> exit concentration variation with operating pressure and equivalence ratio for the can type combustor. ....	83
Figure 45: Variation of NO emission index with operating pressure and equivalence ratio for the can type combustor. ....	83
Figure 46: NO <sub>x</sub> exit concentration variation with equivalence ratio and operating pressure for the annular type combustor.....	84
Figure 47: Variation of NO emission index with operating pressure and equivalence ratio for the annular type combustor.....	85
Figure 48: CO exit concentration variation with equivalence ratio and operating pressure for the can type combustor .....	86

Figure 49: Variation in CO emission index concentration with operating pressure and equivalence ratio for the can type combustor .....	86
Figure 50: Variation in CO exit plane concentration with operating pressure and equivalence ratio .....	87
Figure 51: Variation in CO emission index concentration with operating pressure and equivalence ratio .....	88
Figure 52: Can combustor combustion efficiency variation with operating conditions ...	89
Figure 53: Annular combustor combustion efficiency variation with operating conditions.....	89

## 1. INTRODUCTION

Gas Turbine engines produce harmful pollutants that can cause irreparable damage to the environment. In light of this, strict standards have been put in place to limit the amount of  $\text{NO}_x$ , CO, unburned hydrocarbons, and other harmful products of combustion. These standards make it necessary for engineers to come up with ways to reduce emissions while maintaining, acceptable levels of performance such as the thermal efficiency, combustor stability, and pattern factor. There are several different combustor designs that have been implemented over the years that have been successful in reducing emissions, such as lean direct injection (LDI), lean premixed prevaporized (LPP), and rich-burn/quick-quench/lean-burn (RQL) combustors. However, none of the aforementioned combustor designs are without flaw. Much research is currently under way to improve the design of such combustors to reduce emissions. This thesis seeks to present performance characteristics of a high pressure RQL combustor called the sudden expansion combustor (SUE) that is being designed to produce low emissions [1]. The SUE combustor does not use any swirlers to produce a recirculating region to stabilize the flame necessary for combustion. Rather, it uses a sudden expansion and jets of air and the fuel to create the recirculation region necessary to anchor the flame. The SUE combustor is

shown schematically in Figure 1. Two different variants of the SUE combustor are considered: a can type combustor and an annular type combustor. Parametric studies are performed to see how each combustor's  $\text{NO}_x$  and CO levels vary with operational pressure and equivalence ratio within the combustor.

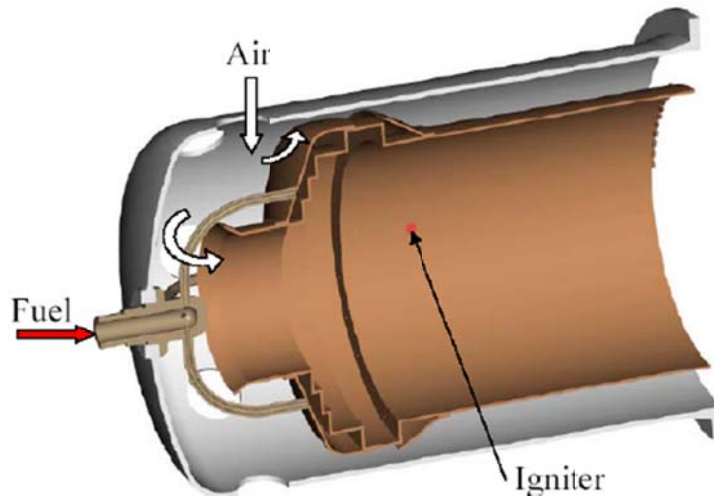


Figure 1: SUE Can Combustor. The cooling vanes are not shown in this figure.

The SUE combustor is analyzed using computational fluid dynamics (CFD) through the commercial code FLUENT. The geometry is modeled in Solidworks and meshed in ICEM CFD utilizing an unstructured mesh. Due to restrictions in computational power, only an angular sector of each combustor is modeled. Symmetric boundary conditions are used to approximate the flow in a full 360 degree combustor. Modeling the geometry that surrounds the liner and the liner itself is also computationally very expensive. Thus, only the flow within the combustor liner is simulated. Jets of air into the liner are modeled as velocity inlet boundary conditions. This way, different

proportions of air flow rates are controlled to see which ones are optimal for low emissions. Once the correct proportions of air are determined, the geometry surrounding the liner can later be designed and simulated for a better representation of the flow field.

The flow turbulence is modeled using the  $k$ - $\epsilon$  model with wall functions to approximate the flow within the boundary layer region. Selected non-premixed combustion is handled by using a beta probability density function ( $\beta$ -PDF) model [2]. Since the fuel used by the SUE combustor is liquid kerosene, FLUENT's discrete phase model is used to simulate the fuel injection and evaporation processes. The complex processes of primary and secondary atomization of the injected fuel are neglected in the analysis as suggested in reference 3. Kerosene droplets are injected into the computational domain in the shape of a cone with specified initial conditions such as, initial velocity, droplet diameter, cone angle, and cone radius. The fuel droplets are tracked in the computational domain using the Euler-Lagrange formulation. The effects of mass transfer, heat transfer, and momentum transfer between the gas and liquid phases are handled by empirical relations in the liquid phase and source terms in the gas phase equations. To compute the  $\text{NO}_x$  levels, a species conservation equation is written for the  $\text{NO}_x$  with the source terms calculated from chemical kinetics. The Zeldovich mechanism [2] is used to predict thermal  $\text{NO}_x$  while the Fenimore mechanism is used for prompt  $\text{NO}_x$  formation.

This thesis goes over some of the background theory necessary to appreciate the complex phenomena that occur inside a typical gas turbine combustor. The background

theory shows how complicated the physics to justify the need for approximations in order to bring the required computational effort to a manageable level. The time averaged equations of motion are presented first. Then some turbulence models are discussed that are needed for the solution of the time averaged equations of motion. Combustion fundamentals are presented next, such as chemical kinetics, spray processes, and the mixture fraction concept. Some turbulent combustion models are presented and the  $\beta$ -PDF model is explained in detail, with some basic combustor design practices to follow in the subsequent section. This review highlights what is required of all combustors in order to achieve complete, stable combustion without any harm to other engine components. Various combustor designs are presented as to show how they achieve low emissions.

After the background theory, the geometry of the SUE combustor is presented. Then, the numerical methods that are used to solve the governing equations are reviewed along with the appropriate boundary conditions. Two different combustors are simulated operating at five different operating pressures, from 300 psi (20.7 bar) to 100 psi (6.9 bar). For each operating pressure, the global equivalence ratio is also varied from 0.9 to 0.5. The  $\text{NO}_x$  and CO levels are mass-averaged at the exit plane of the combustor and plotted against the equivalence ratio with the operating pressure as a parameter. Results of various cases are shown and any trends found are reported in the results section.



## 2. BACKGROUND THEORY

Turbulence and combustion models used in the CFD analysis are briefly reviewed first. Then some theory on atomization and its modeling is discussed, followed by a discussion on radiation modeling and pollutant formations. Some performance parameters are outlined to compare different operating conditions within the combustors. How these parameters are calculated and their meaning are discussed in the “Compressibility and Performance Parameters section”. The “Combustor Fundamentals” section describes a typical combustor’s geometry and reviews some basic low emission combustor designs. The techniques used to discretize and solve the governing equations of motion are described in the “Solver Theory” section. This chapter concludes with the literature review on low emission combustors with a focus on aircraft combustors.

### *2.1 Turbulence Modeling*

Small perturbations appear in all flows due surface roughness, random changes in the operating conditions, and so on. In laminar flows, the viscous forces are sufficient to dampen these perturbations which eventually die out. However, if the inertial forces exceed the viscous forces by a certain amount, the small perturbations start to grow and eventually the whole flow becomes unstable. The flow becomes highly irregular and flow variables start to randomly fluctuate with time [4]. The governing Navier-Stokes equations can no longer be solved directly for all practical configurations; an averaging or filtering process needs to be performed on the variables in order to obtain a solution.

The most common approach to turbulence modeling is to decompose each flow variable into a mean component and fluctuating component, which is referred to as the Reynolds decomposition. For instance, the velocity  $u_i(\mathbf{x}, t)$  after Reynolds decomposition becomes:

$$u_i(\mathbf{x}, t) = \bar{u}_i(\mathbf{x}, t) + u_i'(\mathbf{x}, t)$$

Equation 1: Reynolds decomposition

The mean component is obtained by time averaging the flow variable. For instance, the time average of velocity  $\bar{u}_i$  is shown below [5]:

$$\bar{u}_i(\mathbf{x}, t) = \frac{1}{T} \int_{t_0}^{t_0+T} u_i(\mathbf{x}, t) dt$$

Equation 2: Time average of velocity

where T is the averaging period. Equations similar to Equation 1 for all the variables are substituted into the governing equations of motion and time averaging is performed on all the equations. The results are the Reynolds averaged Navier-Stokes equations (RANS). For illustrative purposes, the Reynolds averaged momentum equation for a steady incompressible fluid is shown below in Equation 3:

$$\bar{u}_j \frac{\partial \bar{u}_i}{\partial x_j} = \frac{1}{\rho} \frac{\partial}{\partial x_j} (-\bar{P} \delta_{ij} + 2\mu \bar{S}_{ij} - \rho \overline{u_i' u_j'})$$

Equation 3: Reynolds averaged momentum equation for steady incompressible flow

Where  $\rho$  is the fluid density,  $\bar{P}$  is the time averaged pressure,  $\mu$  is the dynamic viscosity,  $\delta_{ij}$  is the kronecker delta, and  $\bar{S}_{ij}$  is the mean rate of strain given by:

$$\bar{S}_{ij} = \frac{1}{2} \left( \frac{\partial \bar{u}_i}{\partial x_j} + \frac{\partial \bar{u}_j}{\partial x_i} \right)$$

Equation 4: Rate of strain tensor

$\overline{\rho u_i' u_j'}$  is called the Reynolds stress and has six independent components that are unknown a priori. These stresses must be modeled in order to obtain a solution to the Navier-Stokes Equations. Typically a combination of theoretical and experimental methods are used to model them. A very common approach is to assume that the Reynolds stresses are related to the mean velocity gradients by using the Boussinesq hypothesis [2]:

$$-\overline{\rho u_i' u_j'} = \mu_t \left( \frac{\partial \bar{u}_i}{\partial x_j} + \frac{\partial \bar{u}_j}{\partial x_i} \right) - \frac{2}{3} \left( \rho k + \mu_t \frac{\partial \bar{u}_k}{\partial x_k} \right) \delta_{ij}$$

Equation 5: Boussinesq hypothesis

Where  $k$  is the average turbulent kinetic energy given by

$$k = \frac{1}{2} \overline{u_i' u_i'}$$

Equation 6: Average turbulent kinetic energy

and  $\mu_t$  is the turbulent viscosity. The turbulent kinetic energy and turbulent viscosity need to be specified in order to obtain a solution. Perhaps the most popular technique is to solve the transport equations for the turbulent kinetic energy and for the turbulent dissipation rate  $\varepsilon$ . Subsequently from  $k$  and  $\varepsilon$ , the turbulent viscosity is calculated from Equation 7.

$$\mu_t = \rho C_\mu \frac{k^2}{\varepsilon}$$

Equation 7: Turbulent viscosity

where  $C_\mu$  is a constant taken equal to 0.09.  $C_\mu$  has been calculated from direct numerical simulation (DNS) results in turbulent channel flows [4]. There are additional terms in the turbulent kinetic energy and turbulent dissipation rate equation that still require modeling. The exact equation for the transport of turbulent kinetic energy is [6]:

$$\rho \frac{\partial k}{\partial t} + \rho \bar{u}_j \frac{\partial k}{\partial x_j} = -\rho \overline{u_i' u_j'} \frac{\partial \bar{u}_i}{\partial x_j} - \rho \varepsilon + \frac{\partial}{\partial x_j} \left[ \mu \frac{\partial k}{\partial x_j} - \frac{1}{2} \overline{\rho u_i' u_i' u_j'} - \overline{p' u_j'} \right]$$

Equation 8: Transport of turbulent kinetic energy

The last two terms on the right hand side of Equation 8 are grouped together and modeled as:

$$\frac{1}{2} \overline{\rho u_i' u_i' u_j'} - \overline{p' u_j'} = -\frac{\mu_t}{\sigma_k} \frac{\partial k}{\partial x_j}$$

Equation 9: Modeling of triple velocity correlations and pressure velocity correlation where  $\sigma_k$  is the turbulent Prandtl number for kinetic energy and its value is taken to be 1 from DNS results [4]. With the above assumptions, the incompressible form of the turbulent kinetic energy equations becomes:

$$\rho \frac{\partial k}{\partial t} + \rho \bar{u}_j \frac{\partial k}{\partial x_j} = \left[ \mu_t \left( \frac{\partial \bar{u}_i}{\partial x_j} + \frac{\partial \bar{u}_j}{\partial x_i} \right) - \frac{2}{3} \left( \rho k + \mu_t \frac{\partial \bar{u}_k}{\partial x_k} \right) \delta_{ij} \right] \frac{\partial \bar{u}_i}{\partial x_j} - \rho \varepsilon + \frac{\partial}{\partial x_j} \left[ \left( \mu + \frac{\mu_t}{\sigma_k} \right) \frac{\partial k}{\partial x_j} \right]$$

Equation 10: Modeled equation for turbulent kinetic energy

The exact equation for the turbulent dissipation rate is very complex and can be found in reference 6; only its modeled form is presented below:

$$\begin{aligned} \rho \frac{\partial \varepsilon}{\partial t} + \rho \bar{u}_j \frac{\partial \varepsilon}{\partial x_j} = & C_{\varepsilon 1} \frac{\varepsilon}{k} \left[ \mu_t \left( \frac{\partial \bar{u}_i}{\partial x_j} + \frac{\partial \bar{u}_j}{\partial x_i} \right) - \frac{2}{3} \left( \rho k + \mu_t \frac{\partial \bar{u}_k}{\partial x_k} \right) \delta_{ij} \right] \frac{\partial \bar{u}_i}{\partial x_j} - C_{\varepsilon 2} \rho \frac{\varepsilon^2}{k} \\ & + \frac{\partial}{\partial x_j} \left[ \left( \mu + \frac{\mu_t}{\sigma_\varepsilon} \right) \frac{\partial \varepsilon}{\partial x_j} \right] \end{aligned}$$

Equation 11: Modeled equation for turbulent dissipation rate

With  $C_{\varepsilon 1} = 1.44$ ,  $C_{\varepsilon 2} = 1.92$ ,  $\sigma_k = 1$ , and  $\sigma_\varepsilon = 1.3$  determined from experiments of simple turbulent flows [2]. With Equations 3, 5, 7, 10, and 11, along with the continuity equation, the flow field is solved.

The above  $k$ - $\epsilon$  model constants are used for many CFD analyses, including the analyses presented in this thesis. These constants are chosen so that they are reasonable for the most common flows. Ideally, these constants should be changed so that the CFD results agree best with any available experimental results. Since there are no available results for the geometry considered in this thesis, the default values are retained.

The  $k$ - $\epsilon$  model is generally valid for high Reynolds number flows that are fully turbulent. The  $k$ - $\epsilon$  model also assumes the Reynolds stresses are isotropic. In flows with strong swirl, such as the flow found in combustors, the Reynolds stresses are highly anisotropic and the  $k$ - $\epsilon$  model may prove to be inadequate. (The Boussinesq hypothesis is another source of uncertainty in CFD analysis, for it is not valid in all flows. It fails, for example, when the shearing rate changes suddenly) [4, 6].

Despite the apparent disadvantages, the  $k$ - $\epsilon$  model is predominantly used in this thesis, since it is computationally inexpensive and fairly stable. This is especially important when simultaneously solving a large number of equations present when running combustion simulations. The  $k$ - $\epsilon$  model is used in many numerical simulations in combustion [7-9] thus it is used here to stay consistent with the literature

When the strain exceeds a certain value, the  $k$ - $\epsilon$  model predicts negative value for the normal stresses, which is not physically possible [2]. The realizable  $k$ - $\epsilon$  model fixes this problem by using an expression involving mean strain and mean rotation rates to calculate  $C_\mu$  instead of treating it as a constant. One case is computed with the realizable  $k$ - $\epsilon$  model to compare with the  $k$ - $\epsilon$  model.

The Reynolds-stress model (RSM) is another turbulent viscosity model that is widely used in which a transport equation for each of the Reynolds-stresses is solved. As

a result, seven equations must be solved as opposed to two equations in  $k$ - $\epsilon$  models. Thus it requires more computational effort when compared to the  $k$ - $\epsilon$  model. In exchange for longer running times, one can model highly anisotropic flows with reasonable accuracy. The RSM is not the “silver bullet” to the turbulence problem, however, like many turbulent viscosity models, the RSM utilizes semi-empirical methods in order to model its correlation terms. These methods are not valid for all flow configurations and must be used with caution. The Reynolds-stress model is compared with the  $k$ - $\epsilon$  model in this thesis for one case study; the differences between the two models are presented in the results section.

Special care needs to be taken when computing flow variables in the vicinity of the combustor wall. There exist large gradients at the wall which needs to be handled properly in order to obtain an accurate solution. The approach taken here is to use the law of the wall to compute the flow adjacent to the walls. Within a turbulent boundary layer, there exist three regions: the viscous sublayer, the buffer layer, and the log-law region. The law of the wall is used so that the flow in the viscous sublayer and the buffer region need not be resolved. Instead, an empirical formula is used to calculate the mean velocity, the dissipation rate, turbulent production, and the temperature of the first near wall node. The equations for these quantities can be found in the FLUENT theory guide [2]. Using the law of the wall reduces computational costs when compared to modeling all three regions because the first computational cell can be placed further away from the wall, which results in less cells overall.

An alternative to the turbulent viscosity models is a scale resolving simulation (SRS) model. In a turbulent viscosity model, all scales of turbulence are modeled and the

equations of motion are time averaged so that only mean variables are solved for. On the other hand, the SRS method models only the small scales of turbulence and resolves the large scales [10]. The advantage of SRS is that the large eddies, which are dependent upon geometry, and are resolved while the small eddies, which are more uniform and do not depend much upon the flow geometry are modeled. Because the small scales are uniform in nature, they can be modeled by a theory which is applicable to a wide variety of flow problems. Furthermore, SRS are transient: they can capture instabilities found in gas turbine combustors such as the vortex bubble breakdown formed in flows with strong swirl. SRS can therefore yield much more information than a RANS simulation can provide.

Unfortunately, SRS model is computationally extremely expensive, even more so than the RSM model. The grid size must be small enough to capture the turbulent structures of interest. Ideally, eddies in the inertial subrange should be resolved. To accomplish this, Fluent recommends that 40-50 computational cells should span a length equal to the integral length scale [11]. In addition, the time step has to be sufficiently small enough such that a Courant Friedrich Levi number of 1 is obtained throughout the computational domain. These requirements are also too stringent for this thesis, so the SRS model was not implemented.

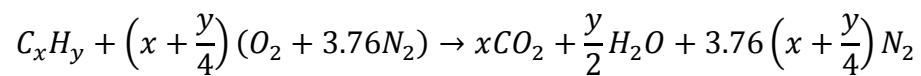
## *2.2 Combustion Fundamentals*

Combustion consists of several heat-releasing chemical reactions between a fuel and an oxidizer. If the reactants are mixed before the reaction takes place, then the combustion that ensues is categorized as premixed combustion. Once ignited, the flammable mixture propagates within the combustion chamber constantly consuming

fresh gases. The fresh gases heat up as they pass through the flame and the heat causes the fresh gases to chemically react, thereby releasing more heat. The flame propagates at a speed called the flame speed, and when the flame speed is equal to the speed of the incoming gases, the flame remains stationary. It is the propagating nature of a premixed flame that restricts its universal use in combustion devices. If the fuel supply is shut off unexpectedly, the flame can propagate back to the fuel supply and possibly cause an explosion [12]. It is for this reason that aircraft combustion chambers generally use a nonpremixed flame or partially premixed flame. Premixed flames are predominately used in stationary gas turbines because of their potential for low NO<sub>x</sub> emissions.

A nonpremixed flame occurs when fuel and oxidizer are not mixed before combustion takes place. A mixture of fuel and oxidizer within the combustion chamber must be given enough time in order for the chemical reactions to take place completely. Nonpremixed flames are more stable and easier to control than premixed flames. The sudden expansion type combustor utilizes a nonpremixed flame and, combustion, and its various configurations, are the focus of this project report.

Before various available nonpremixed combustion models are reviewed, some general combustion terms and equations are explained. A global reaction considers the reactants that initiate combustion, and the final products of combustion in one step. If there is just the right amount of hydrocarbon fuel and oxidizer so that only CO<sub>2</sub> and H<sub>2</sub>O remain after combustion, then such a global reaction is a stoichiometric reaction. A stoichiometric reaction for a generalized hydrocarbon fuel is given as:



Equation 12: Generalized hydrocarbon stoichiometric reaction



The stoichiometric air-fuel ratio can be calculated as follows

$$AF_{stoic} = \frac{4.76 \left( x + \frac{y}{4} \right) MW_{air}}{MW_{fuel}}$$

Equation 13: Stoichiometric air-fuel ratio

where  $AF_{stoic}$  is the stoichiometric air-fuel ratio,  $MW_{air}$  is the molecular weight of air (28.85 kg/kmol) and  $MW_{fuel}$  is the molecular weight of fuel. FLUENT materials library has  $C_{12}H_{23}$  as the molecular formula for kerosene (JP-5), which yields  $AF_{stoic} = 14.4$ .

The local equivalence ratio,  $\phi_L$ , is a measure of how fuel rich, or fuel lean a mixture is at a point. The local equivalence ratio is defined as:

$$\phi_L = \frac{AF_{stoic}}{AF_L}$$

Equation 14: Local equivalence ratio

where  $AF_L$  is the local mass ratio of air to fuel at a point. When  $\phi_L$  is unity, the mixture is stoichiometric. When  $\phi_L$  is greater than unity, then the mixture is fuel rich and when  $\phi_L$  is less than unity, the mixture is fuel lean. The equivalence ratio can also be established on a global basis for a combustor as:

$$\phi_G = \frac{AF_{stoic}}{AF_G}$$

Equation 15: Global equivalence ratio

where  $\phi_G$  is the global equivalence ratio, and  $AF_G$  is the ratio of the total mass flow rate of air to the total mass flow rate of the fuel entering the combustor.

Equation 12 shows the initial and final states of combustion for the reactant and product species. What is not shown, however, are the intermediate species formed during the combustion process. Combustion takes place in a number of steps forming intermediate species with each step. Those intermediate species then form other

intermediate species until combustion is complete. Each elementary reaction shows one of the many chemical reactions that occur during the combustion process, and the collections of all elementary reactions is called the reaction mechanism. The number of elementary reactions in a reaction mechanism can range from 40 to several thousand [13]. Often, a reduced mechanism is used to approximate the reaction mechanism. There are several techniques used to obtain a reduced mechanism, two of which are worth mentioning here. One technique is to use the steady-state assumption on intermediate species that are produced and consumed in the reactions that take place very quickly. Since production and consumption rates of a species are approximately equal, time rate of change of concentration is approximately zero. The other technique is to evoke the partial-equilibrium assumption. The partial-equilibrium assumption is used when a reaction is very fast in the forward and reverse direction. The fast reaction can then be assumed to be in chemical equilibrium so that rate equation need not be solved for the fast species. Both the partial-equilibrium and steady-state equations are used to calculate  $\text{NO}_x$  formation in this thesis.

In order to mathematically model flows with combustion, the species conservations equations must be solved along with the Navier-Stokes and the energy equations. The species conservation equation for the  $i$ th species is [12]:

$$\frac{\partial}{\partial t}(\rho Y_i) + \frac{\partial}{\partial x_j}(\rho \bar{u}_j Y_i) = \frac{\partial}{\partial x_j}(m''_j) + \dot{\omega}_i$$

Equation 16: Species conservation equation

where  $Y_i$  is the mass fraction of species  $i$ ,  $m''_j$  is the mass flux of species  $i$  in the  $j$ th direction, and  $\dot{\omega}_i$  is the rate of production of species  $i$  due to chemical reactions. The species mass flux poses modeling problems due to concentration gradients, thermal

gradients, pressure gradients, and other effects (see reference 12 and 14 for more details).

The equations that describe these effects are quite complex. The mass flux term will be further discussed in the turbulent combustion section.

The chemical production term poses a difficult challenge to model as well. It is shown the following two equations [15]

$$\dot{\omega}_i = MW_i \sum_{j=1}^M (v''_{ij} - v'_{ij}) Q_j$$

Equation 17: Reaction rate term

$$Q_j = K_{fj} \prod_{k=1}^N \left( \frac{\rho Y_k}{MW_k} \right)^{v'_{kj}} - K_{rj} \prod_{k=1}^N \left( \frac{\rho Y_k}{MW_k} \right)^{v''_{kj}}$$

Equation 18: Progress Rate

where M is the number of reactions, N is the number of species,  $v''_{ij}$  and  $v'_{kj}$  is the stoichiometric coefficient of the products and reactants respectively, and  $Q_j$  is the progress rate of the jth reaction.  $K_{fj}$  is called the forward reaction rate and is calculated from an Arrhenius expression:

$$K_{fj} = A_{fj} T^{\beta_j} \exp \left( -\frac{T_{\alpha j}}{T} \right)$$

Equation 19: Arrhenius law

where  $A_{fj}$ ,  $\beta_j$ , and  $T_{\alpha j}$  are the pre-exponential constant, the temperature exponent, and the activation temperature respectively, and T is the temperature.  $K_{rj}$  is the reverse reaction rate and can be calculated similarly from chemical equilibrium and  $K_{fj}$ . The species conservation equation is written for N-1 species and even when complete reaction mechanism is used, the calculations would require vast computational resources.

Furthermore, computing the time-average of the reaction rate for turbulent flows is

extremely difficult because of nonlinearity of the Arrhenius expression. These complications force the use of reduced mechanisms in various combustion models as well as some alternate methods. One such alternative method is the mixture fraction approach, in which instead of working with individual species mass fractions, one deals with a variable called the mixture fraction. The mixture fraction is the ratio of mass of species that originated in the fuel to the total mass of the mixture. If it is assumed that all diffusion coefficients of species are equal and the corresponding Lewis number (defined as the ratio of thermal diffusivity to mass diffusivity) is unity, which is a good assumption in turbulent flow. Then the N-1 mass fraction equations can be replaced with the mixture fraction equation as shown below [12]:

$$\frac{\partial}{\partial t}(\rho f) + \frac{\partial}{\partial x_j}(\rho \bar{u}_j f) = \frac{\partial}{\partial x_j} \left( \rho D \frac{\partial f}{\partial x_j} \right)$$

Equation 20: Mixture fraction transport equation

where  $f$  is the mixture fraction and  $D$  is the mass diffusion coefficient. This equation contains no source terms, which is its major strength. One must then find relations between the mixture fraction and the various species mass fractions, temperature, and density. One method to obtain such a relationship is to assume the species are in chemical equilibrium. The species mass fractions, temperature, and density can then be found from a thermodynamic database for a given value of mixture fraction.

With the mixture fraction field known, the local equivalence ratio can be computed from:

$$\phi_L = AF_{stoic} * f(1 - f)$$

Equation 21: Equivalence ratio as a function of mixture fraction

Equation 21 can be used to compute contours of constant equivalence ratios to see where the rich regions of the flame reside.

One very important theoretical parameter in combustion is the corresponding adiabatic flame temperature. It is the temperature that the products of combustion reach if all the chemical energy in the fuel is used solely to raise the temperature of the products. In reality, the flame loses heat due to radiation heat transfer. Complete combustion does not take place in practice as well; these two effects lower the flame's temperature. Therefore, the adiabatic flame temperature is an upper bound that the flame can ever reach. This could be used as a check against numerical calculations and is done so in this thesis.

### *2.3 Turbulent Combustion Modeling*

Time-averaging the governing equations is a widely used technique in predicting turbulent flows. This technique, however, is not so straight forward when applied to the species conservation equations due to the nonlinear Arrhenius expression. The mean reaction rate must be modeled, or another equation that accounts for chemical effects must be used in place of the species conservation equation. Two turbulent combustion models are presented here: the eddy dissipation model (EDM) and the presumed probability density function (PPDF).

In the EDM model, it is assumed that chemistry is much faster than the rate at which eddies can mix the reactants. This assumption is reasonable when the operating pressure is high, since chemical reaction rates increase with pressure [15]. The mean reaction rate can then be taken to be proportional to the turbulent mixing rate,  $\epsilon/k$ . For a

one step irreversible reaction, the mean reaction rate  $\bar{\omega}$  can be found from the minimum of the following three equations [16]:

$$\bar{\omega}_f = \bar{\rho} A \bar{Y}_f \frac{\varepsilon}{k}$$

Equation 22: Fuel reaction rate

$$\bar{\omega}_{O_2} = \frac{\bar{\rho}}{s} A \bar{Y}_{O_2} \frac{\varepsilon}{k}$$

Equation 23: Oxidizer reaction rate

$$\bar{\omega}_p = \frac{\bar{\rho}}{s + 1} A B \bar{Y}_p \frac{\varepsilon}{k}$$

Equation 24: Product reaction rate

where  $s$  is the oxygen stoichiometric coefficient, and  $A$  and  $B$  are empirical constants. In FLUENT,  $A$  and  $B$  are taken to be 4 and 0.5 respectively. The EDM model must account for dissociation, or else the predicted temperatures would be far too high. To account for dissociation without considering additional reactions, a modified polynomial for the specific heats for each species can be used. This technique is used in this thesis when a case is computed using the EDM model

In the presumed probability density function (PPDF) approach, the mixture fraction is used to obtain the mean density, mean temperature, and means species mass fractions from:

$$\bar{\psi} = \int_0^1 p(f) \psi(f) df$$

Equation 25: Mean scalar calculated from PDF

where  $\psi$  represents the temperature, density, and species mass fractions and the relation  $\psi(f)$  is found from a thermodynamic database.  $p(f)$  is the probability density function

of the mixture fraction for a turbulent flow. In a PPDF model,  $p(f)$  is assumed to be an analytical function of one or more of its moments. This thesis uses a  $\beta$ -PDF for  $p(f)$  as given by the following three equations [2]:

$$p(f) = \frac{f^{\alpha-1}(1-f)^{\beta-1}}{\int f^{\alpha-1}(1-f)^{\beta-1}df}$$

Equation 26: Equation for  $p(f)$

with  $\alpha$  as:

$$\alpha = \bar{f} \left[ \frac{\bar{f}(1-\bar{f})}{\bar{f}'^2} - 1 \right]$$

Equation 27: Equation for  $\alpha$

and  $\beta$  as:

$$\beta = (1-\bar{f}) \left[ \frac{\bar{f}(1-\bar{f})}{\bar{f}'^2} - 1 \right]$$

Equation 28: Equation for  $\beta$

The  $\beta$ -PDF is a function of its first two moments, the mean mixture fraction and the mixture fraction variance. To compute the mean mixture fraction, Equation 20 is time-averaged and in order to close the turbulent terms, a gradient diffusion hypothesis is utilized. The resulting mean mixture fraction equation is [2]:

$$\frac{\partial}{\partial t}(\rho \bar{f}) + \frac{\partial}{\partial x_j}(\rho \bar{u}_j \bar{f}) = \frac{\partial}{\partial x_j} \left( \frac{\mu_t}{\sigma_t} \frac{\partial \bar{f}}{\partial x_j} \right)$$

Equation 29: Mean mixture fraction transport equation

The mixture fraction variance equation can be derived from the mean mixture fraction equation; its modeled form is [2]:

$$\frac{\partial}{\partial t}(\rho \overline{f'^2}) + \frac{\partial}{\partial x_j}(\rho \overline{u_j f'^2}) = \frac{\partial}{\partial x_j} \left( \frac{\mu_t}{\sigma_t} \frac{\partial \overline{f}}{\partial x_j} \right) + C_g \mu_t \left( \frac{\partial \overline{f}}{\partial x_j} \frac{\partial \overline{f}}{\partial x_j} \right) - C_d \rho \frac{\epsilon}{k} \overline{f'^2}$$

Equation 30: Mean mixture fraction variance

$\sigma_t$ ,  $C_g$ , and  $C_d$  are model constants; their values are as 0.85, 2.86, and 2 respectively.

Equation 25 for each scalar variable  $\psi$  is valid only for adiabatic flows. For non-adiabatic flows,  $\psi$  is a function of the mean enthalpy  $\overline{H}$  and the mixture fraction. The following transport equation for the mean enthalpy must also be solved [2]:

$$\frac{\partial}{\partial t}(\rho \overline{H}) + \frac{\partial}{\partial x_i}(\rho \overline{u_i H}) = \frac{\partial}{\partial x_i} \left( \frac{k_t}{c_p} \frac{\partial \overline{H}}{\partial x_i} \right)$$

Equation 31: Transport of mean enthalpy

Thus a joint PDF of the mixture fraction and the enthalpy must be considered. An assumption employed by FLUENT is that the enthalpy fluctuations are independent of the enthalpy level, and  $\overline{\psi}$  then becomes:

$$\overline{\psi} = \int_0^1 p(f) \psi(f, \overline{H}) df$$

Equation 32: Equation for a mean scalar for a non-adiabatic system using the PPDF model

This equation is computed for various values of mean mixture fraction, mixture fraction variance, and mean enthalpy, and stored in look up tables that are used to calculate the temperature, density, and species mass fractions during the CFD computations.

Since for fuel rich mixtures the chemical equilibrium assumption is invalid, one must take into account chemical non-equilibrium. One method to take chemical non-equilibrium into account is the use of the rich flammability limit (RFL) concept. In the RFL model, chemical equilibrium calculations cease when the mixture fraction goes above twice the stoichiometric mixture fraction. Temperature, density, and species mass



fractions are calculated based on mixing and not burning, which is because a mixture at an equivalence ratio of about 2 simply mixes without burning [18].

#### *2.4 Discrete Phase Modeling*

Gas turbines employed in aircraft differ from stationary gas turbines because aircraft must carry their fuel with them. This restricts aircraft combustors to use liquid fuel. Liquid fuel is injected into the combustion chamber via an atomizer. The atomizer breaks up the fuel into droplets and injects them into the combustor to evaporate. The atomization process of the liquid fuel and the subsequent combustion process of the fuel droplets are summarized in this section as justification of the idealization of the discrete liquid phase. Then the corresponding discrete phase models are presented to show how the liquid phase processes are computed.

The atomization process consists of primary atomization and secondary atomization. Primary atomization consists of forming droplets from a jet or sheet of liquid fuel. This is accomplished by a high relative velocity between the fuel and the atomizing fluid (which is usually air). The relative motion between the fuel and the atomizing fluid creates instabilities which cause some of the fuel to break away from the jet which then forms into droplets. The mechanism which creates the relative motion between the fuel and air differs between different atomizer designs. One of the simplest atomizers is the plain-orifice atomizer, which consists of fuel exiting a circular hole as shown below

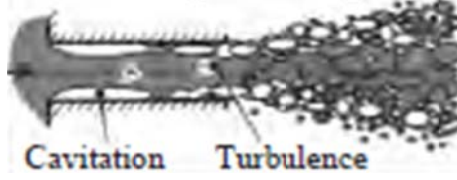


Figure 2: Diagram of a plain-orifice atomizer [19]

As one can see from Figure 2, the flow inside an atomizer is quite complex, even for the simplest of cases. Complex multiphase flow effects dominate the internal flow within atomizers which requires the use of empirical correlations to predict performance parameters such as spray angle and mean droplet diameters [2]. The flow field and corresponding droplet distribution out of an atomizer is strongly dependent on both air and fuel properties as well as atomizer geometry [20]. One very important parameter governing the atomization process is the Weber number which is the ratio of the dynamic pressure to the surface tension on a droplet:

$$We = \frac{\frac{1}{2}\rho U_R^2}{\sigma/D}$$

Equation 33: Weber number

where  $\rho$  is the density of either the gas phase or the liquid phase,  $\sigma$  is the surface tension,  $U_R$  is the relative velocity between the liquid phase and the gas phase. Another important dimensionless parameter that appears frequently in the literature is the Ohnesorge number, which accounts for the fuel viscosity:

$$Oh = \frac{\sqrt{We}}{Re}$$

Equation 34: Ohnesorge number

The empirical correlations in the literature are often a function of these dimensionless parameters as well as the nozzle geometry. The Weber number and Ohnesorge number

are also used to categorize different atomization regimes that exist over different operating conditions. In the case of the plain-orifice atomizer injecting fuel into stagnant air, there are four atomization regimes that exist: Rayleigh breakup, first wind-induced breakup, second wind-induced breakup, and atomization regime. Each regime produces a different droplet distribution [19].

The plain-orifice atomizer was presented to show that even the simplest atomizer geometry is still very challenging to model. In practice, plain-orifice atomizers are not used because their spray angle is far too narrow. The prefilming airblast atomizer is one alternative atomizer that is used in gas turbine combustors as shown below

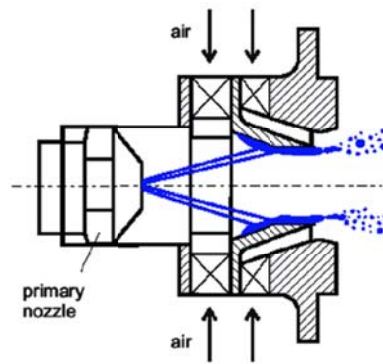


Figure 3: Prefilming airblast atomizer [21]

Here, liquid fuel is injected as a hollow cone spray where it impacts a solid wall called the prefilmer. A liquid film forms on the wall which is exposed to a high velocity airstream which breaks the liquid film into droplets. The atomization of the hollow cone, film formation on the prefilmer, and the final atomization of the liquid film must be accurately predicted to obtain an accurate droplet distribution. Opfer et. al [21] performed a theoretical analysis on an idealized airblast atomizer similar to that shown in Figure 3. They used Rayleigh-Taylor stability analysis to predict the primary atomization of the liquid jet. Once the droplets broke away from the jet, they used a force balance to

compute the trajectory of a large number of droplets. Once the droplets impacted the prefilmer surface, they used a simplified version of the Navier-Stokes equations to predict the height of the film that would form on the prefilmer surface. The film height was then used to calculate the Sauter mean diameter (to be defined later in this section) at the atomizing lip. Their analysis agreed quite well with experimental data.

Secondary atomization occurs when droplets break up into smaller droplets. There are several regimes of secondary atomization that occur under different operating conditions. Each regime occurs with different relevant mechanisms for break up. Different theoretical models to treat secondary atomization can be applied depending on the Weber number and the primary mechanism of breakup. For instance, FLUENT offers a droplet breakup model called the Wave breakup model which predicts newly formed droplets based upon the fastest growing Kelvin-Helmholtz instability [2].

Different atomizers produce a different distribution of droplets sizes. There are different mathematical distribution functions in the literature which can be used to represent empirical data from an atomizer. One very common distribution is the Rosin-Rammler distribution, which is shown below

$$1 - Q = \exp \left[ - \left( \frac{D}{X} \right)^q \right]$$

Equation 35: Rosin-Rammler distribution

where Q is the fraction of volume of droplets less than D, and q and X are constants used to fit the data. The Rosin-Rammler distribution is used in CFD analysis to represent a polydisperse spray without modeling the dense spray region close to the injector. If no empirical data is available for an atomizer, then one can approximate the polydisperse spray with a monodisperse spray with an equivalent average diameter. The most

commonly used average diameter is the Sauter mean diameter, which is the “diameter of a drop whose surface-to-volume ratio is equal to that of the entire spray” [20].

To model the liquid phase, the approach taken here is to use an Euler-Lagrange formulation. In this approach, the gas phase is treated as a continuum by solving the Navier-Stokes equations, energy equation, species equation, and so on. The liquid phase, however, is written in a Lagrangian frame of reference for each droplet, and each droplet is tracked within the computational domain. Instead of modeling the flow around a droplet, empirical correlations are used to account for the effect of the gas phase on the liquid phase. To account for the effect of the liquid phase on the gas phase, source terms are used in the momentum equations to account for drag, mean enthalpy equation to account for heat transfer, and mean mixture fraction to account for evaporation. The main assumption used in the Euler-Lagrange model is dilute spray approximation. Near the injector, the volume fraction of the liquid phase is high, and particle collisions and coalescence effects occur frequently. Moreover, the evaporation rate of a droplet in the dense spray region is affected by its neighboring droplets. Away from the injector, however, droplets rarely collide and the evaporation of one droplet does not affect another droplet’s evaporation rate. The dilute spray assumption assumes the droplets tracked within the computational domain are far away from each other so that empirical correlations based off of a single evaporating droplet may be used.

To track a droplet within the computational domain, a force balance is written on each droplet in the  $i$ th direction [2]:

$$\frac{du_{i,p}}{dt} = F_{i,D}(u_i - u_{i,p}) + \frac{g_i(\rho_p - \rho)}{\rho_p} + \sum F$$

Equation 36: Force balance on a droplet

where  $u_{i,p}$  is the velocity of a droplet in the  $i$ th direction,  $u_i$  is the gas velocity in the  $i$ th direction,  $g_i$  is the gravitational acceleration component in the  $i$ th direction,  $\rho$  is the gas density, and  $\rho_p$  is the density of the liquid phase. The  $\sum F$  term represents forces that are usually neglected in spray combustion models such as forces due to pressure gradients, the thermophoretic force, and Saffman's Lift force, to name a few [2]. The second term on the RHS of Equation X represents the gravity force, and is neglected in the current analysis.  $F_{i,D}$  is the drag force on the droplet in the  $i$ th direction and is calculated as follows [2]

$$F_{i,D} = \frac{18\mu}{\rho_p d_p^2} \frac{C_D Re_d}{24}$$

Equation 37: Drag force on a droplet

with:

$$Re_d = \frac{\rho d_p |u_i - u_{i,p}|}{\mu}$$

Equation 38: Droplet Reynolds number

$d_p$  and  $C_D$  are the droplet diameter and droplet drag coefficient respectively. To calculate the drag on the droplet, it is assumed that the droplet is spherical throughout its trajectory. Then the drag coefficient is calculated from [2]:

$$C_D = a_1 + \frac{a_2}{Re_d} + \frac{a_3}{Re_d^2}$$

Equation 39: Drag coefficient for a spherical droplet

where  $a_1$ ,  $a_2$ , and  $a_3$  are constants found from reference 22. Equation 36 is solved for the velocity and the droplet trajectory using a trapezoidal discretization technique. For further details, see the FLUENT theory guide [2].

To model the evaporation of a droplet, FLUENT uses several laws which employ different equations depending upon the droplet's current temperature. When the droplet is below the vaporization temperature of kerosene, which is taken to be 341 K, FLUENT assumes no evaporation takes place, and the temperature of the droplet is calculated from:

$$m_p c_p \frac{dT_p}{dt} = h A_p (T_\infty - T_p)$$

Equation 40: Heating of a droplet

Here, radiation heat transfer of the liquid phase is neglected and the droplet is always assumed to be at a constant temperature  $T_p$ .  $c_p$ ,  $m_p$ ,  $h$ ,  $A_p$ , and  $T_\infty$  are the specific heat of the droplet, mass of the droplet, heat transfer coefficient, droplet surface area, and local gas phase temperature respectively.

When the droplet temperature is at the boiling point of kerosene, which is taken to be 477 K, FLUENT uses a boiling rate controlled evaporation equation:

$$\frac{dd_p}{dt} = \frac{4k_\infty}{\rho_p c_{p,\infty} d_p} (1 + 0.23\sqrt{Re_d}) \ln \left[ 1 + \frac{c_{p,\infty}(T_\infty - T_p)}{h_{fg}} \right]$$

Equation 41: Boiling controlled evaporation rate

where  $c_{p,\infty}$  and  $k_\infty$  is the specific heat and thermal conductivity of the gas phase respectively. It is assumed that the droplet's temperature is at the boiling point throughout the evaporation process.

## 2.5 Radiation Modeling

Radiation heat transfer can be a dominate mode of heat transfer in combustng flows due to the high temperatures of the products of combustion. Furthermore, radiation effects can alter the species concentrations present in the combustor [23]. To account for radiation heat transfer, one must solve the radiative transfer equation (RTE):

$$\frac{dI(\mathbf{r}, \mathbf{s})}{ds} + (a + \sigma_s)I(\mathbf{r}, \mathbf{s}) = an^2 \frac{\sigma T^4}{\pi} + \frac{\sigma_s}{4\pi} \int_0^{4\pi} I(\mathbf{r}, \mathbf{s}') \Phi(\mathbf{s}, \mathbf{s}') d\Omega$$

Equation 42: Radiative transfer equation

$I$  is the radiation intensity at a position  $\mathbf{r}$  in the direction of the vector  $\mathbf{s}$ .  $\frac{dI}{ds}$  is the change in intensity along a ray path.  $\Phi(\mathbf{s}, \mathbf{s}')$  and  $\sigma_s$  are the scattering phase function and scattering coefficient respectively, and are generally a function of temperature, frequency range, chemical concentration, and chemical composition [24].  $a$  is the absorption coefficient which is dependent on temperature, pressure, frequency range, and chemical concentration.  $n$  is the refractive index, and represents the ratio of the speed of light in a medium to the speed of light in a vacuum.  $\sigma$  is the Stefan-Boltzman constant.

The RTE equation differs from the other governing equations in that its dependent variable is a function of direction and position, and it is an integro-differential equation. The RTE has to be further simplified in order to be implemented into a finite volume scheme. There are several techniques in the literature to simplify the RTE equation, two of which are discussed here: the P-1 model and the discrete ordinates (DO) model.

The radiative properties of a fluid are also a source of complexity when modeling radiative flows because they depend on many variables. The emissivity of walls, for example, varies with surface roughness and the amount of oxidation present [25].



Simplification of the properties of the radiating gases and its enclosure must be made in order to obtain a solution to the governing equations. Some of the common simplifications used in the literature are briefly reviewed and are also employed in this report. The scattering coefficient is assumed to be zero throughout the computational domain. All walls are assumed to be grey blackbody emitters, and they also reflect incident radiation in an isotropic manner. The index of refraction is taken to be unity. To model the non-grey behavior of the absorption coefficient and emissivity, the weighted – sum-of-grey-gases (WSGG) model is used. For further details, see the FLUENT theory guide [2].

The P-1 model is a very common simplification to the RTE that is employed in this thesis. The P-1 model expands the radiation intensity into a series of spherical harmonics and retains the first four terms of the series [26]. As a result, one only needs to solve a transport equation for the incident radiation  $G$  [2]:

$$\frac{\partial}{\partial x_i} \left( \frac{1}{3a} \frac{\partial G}{\partial x_i} \right) - aG = -4an^2\sigma T^4$$

Equation 43: P-1 equation (with a zero scattering coefficient)

From the solution of the radiation intensity, one can compute the source term for the mean enthalpy equation,  $S_R$ , due to radiation heat transfer from the expression shown below:

$$S_R = -\frac{\partial q_i}{\partial x_i} = aG - 4an^2\sigma T^4$$

Equation 44: Source term for mean enthalpy equation due to radiation heat transfer where  $q_i$  is the heat flux in the  $i$ th direction. The boundary condition for the incident radiation is given below:

$$q_w = -\frac{1}{3a} \frac{\partial G}{\partial n} = -\frac{\varepsilon_w}{2(2 - \varepsilon_w)} (4an^2\sigma T^4 - G_w)$$

Equation 45: P-1 Boundary Conditions

where  $q_w$ ,  $\varepsilon_w$ , and  $G_w$  is the wall heat transfer due to radiation, wall emissivity, and incident radiation at the wall respectively.

The DO model solves the RTE in  $n$  discrete directions that span a solid angle of  $4\pi$  steradians [26]. As a result, there are  $n$  RTE's that are solved along with the other governing equations. For methods of angular discretization, and boundary conditions of for the discrete ordinates model, see the FLUENT theory guide [2].

## 2.6 Pollutant Formation

This section reviews the effect of  $\text{NO}_x$  and CO on human health and the environment. Then it discusses some general trends found in gas turbine combustors. The section concludes with how  $\text{NO}_x$  formation is modeled in this thesis.

CO is formed in the rich regions of a flame when there is insufficient oxygen to react with the fuel to complete combustion [27]. It can also be formed under lean conditions due to dissociation of  $\text{CO}_2$ . CO is toxic to the human body and can cause asphyxiation if large amounts are inhaled. CO production is minimal towards the leaner side of stoichiometry ( $0.8 < \phi < 1$ ) and rises quickly when the equivalence ratio is outside of that range [28]. Increasing the operating pressure has shown to decrease the CO emissions. An increase in residence time has also shown to decrease CO emissions because more time is available to complete combustion [29].

$\text{NO}_x$  is the term used to collectively refer to oxides of nitrogen; some of the common oxides of nitrogen found in combustion systems are NO,  $\text{NO}_2$ , and  $\text{N}_2\text{O}$ .

Among these three, NO is the most abundant species in a combustor. At lower altitudes, NO forms ozone and NO<sub>2</sub>. Ozone in lower altitudes can cause various illnesses [28]. NO<sub>2</sub> can react with water in the atmosphere to form acid rain which is highly corrosive. NO<sub>2</sub> can also react with unburned hydrocarbons in the atmosphere and sunlight to produce smog. In very high altitudes, NO can react with ozone to deplete the ozone layer that is responsible for blocking harmful ultraviolet rays.

For fuels with no nitrogen content, there are three mechanisms which produce NO<sub>x</sub>: the Zeldovich mechanism, the Fenimore mechanism, and the N<sub>2</sub>O mechanism [28]. NO<sub>x</sub> formed by the Zeldovich mechanism is called thermal NO<sub>x</sub>; it increases exponentially with flame temperature and linearly with an increase in residence time [29]. NO<sub>x</sub> produced by the Fenimore mechanism is referred to as prompt NO<sub>x</sub> and is dependent upon the amount of carbon atoms present in the fuel [2]. NO<sub>x</sub> produced by the N<sub>2</sub>O mechanism involves a reaction between N<sub>2</sub>, O, and a third body molecule [13]. It occurs under oxygen rich conditions and high operating pressures and can occur at lower temperatures as compared to thermal NO<sub>x</sub> due to its lower activation energy [2]. Pressure seems to have a varied effect on NO<sub>x</sub> production which varies with each combustor. NO<sub>x</sub> can be insensitive to pressure, or it can vary with pressure raised to some power between 0.5 and 0.8 [27].

To compute the NO<sub>x</sub> in FLUENT, a NO<sub>x</sub> post processor is used. Once the flow field has been computed, the NO<sub>x</sub> post processor solves a species transport equation for the NO and N<sub>2</sub>O mass fractions. Since the NO<sub>x</sub> calculations are decoupled from the governing equations, it is assumed that the NO<sub>x</sub> has a negligible impact on the rest of the

flow. In modeling the reaction rate term, the quasi-steady state assumption is made for the N atoms and the partial equilibrium assumption is used for O and OH.

To compare NO<sub>x</sub> and CO emissions among the different combustor configurations, a mass weighted average of the NO<sub>x</sub> and CO mole fractions are computed at the exit plane of the combustor. The mole fractions are calculated in parts per million (ppm) on a dry basis as follows [12]:

$$\chi_{i,ppm} = \frac{1,000,000 * \chi_i}{(1 - \chi_{H_2O})}$$

Equation 46: NO and CO in parts per million on a dry basis

where  $\chi_{i,ppm}$  is NO or CO in parts per million on a dry basis,  $\chi_i$  is the NO or CO mole fraction, and  $\chi_{H_2O}$  is the mole fraction of H<sub>2</sub>O. Another indicator of emissions is the emission index, which is the amount of a pollutant emitted in grams per kilogram of fuel. The emission index is calculated as shown below [30]:

$$EI_i = \frac{Y_i \dot{m} * 1000g/kg}{\dot{m}_f}$$

Equation 47: Emission index for pollutant i

where  $EI_i$  is the emission index of either NO or CO, and  $\dot{m}_f$  is the mass flow rate of fuel.

## 2.7 Compressibility Effects and Performance Parameters

An incompressible flow solver is used to solve for the flow field within the combustor. To check the condition of incompressibility, the Mach number must be checked in the exit plane. The Mach number is computed as shown below:

$$Ma = \frac{V_e}{\sqrt{\gamma RT}}$$

Equation 48: Mach number

where  $V_e$  and  $T$  are the mass-weighted axial velocity at the exit and mass-weighted temperature respectively.  $R$  is the gas constant which is taken to be the gas constant of air ( $0.287 \frac{kJ}{kg \cdot K}$ ) since combustion gases have a molecular weight close to air.  $\gamma$  is the ratio of specific heats and its value is taken to be 1.33 which is representative of combustion gases [29].

One important parameter in combustor design which measures losses in the combustor is the ratio of the stagnation pressure drop across the combustor,  $P_{o,e} - P_{o,i}$ , to the inlet stagnation pressure  $P_{o,i}$ . Assuming incompressible flow, the pressure loss,  $\frac{\Delta P_o}{P_{o,i}}$  can be found from:

$$\frac{\Delta P_o}{P_{o,i}} = \frac{\left(P_e + \frac{1}{2}\rho_e V_e^2\right) - \left(P_i + \frac{1}{2}\rho_i V_i^2\right)}{\left(P_i + \frac{1}{2}\rho_i V_i^2\right)}$$

Equation 49: Pressure loss

Another important performance parameter is the combustion efficiency,  $\eta$ , which represents the fraction of fuel that is burned in the combustor to the total fuel mass flow rate. It can be calculated from:

$$\eta = 1 - \frac{Y_f \dot{m}}{\dot{m}_f}$$

Equation 50: Combustion efficiency

where  $\dot{m}_f$  is the fuel flow rate,  $\dot{m}$  is the mass flow rate of the combustion gasses, and  $Y_f$  is the mass-weighted average of the fuel mass fraction in the exit plane.

Residence time is defined as the ratio of the combustor length to the inlet velocity. Physically, it represents the average time a fluid particle spends inside the combustor; it is used in emission calculations in the results section.

## 2.8 Combustor Fundamentals

This section reviews some of the basic combustor configurations used in industry and presents some combustor types used to achieve low  $\text{NO}_x$  emissions.

A conventional can type combustor is shown below:

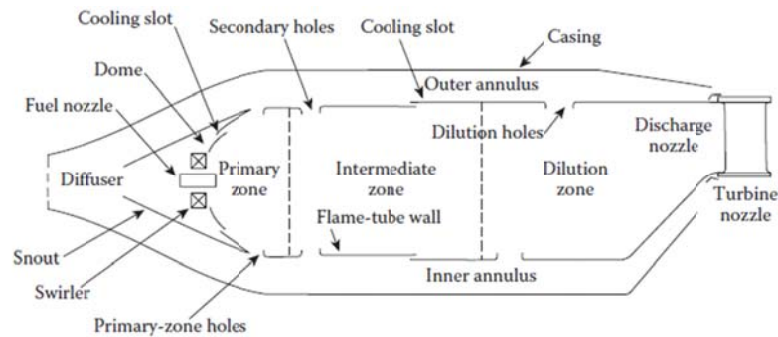


Figure 4: Conventional can combustor [30]

The air exiting the compressor is split between the inner annulus, also called the liner, and the outer annulus. The air entering the liner is sent through a swirler which adds a tangential component to the velocity. If the swirl is strong enough, an adverse axial pressure gradient forms that is strong enough to cause some of the air to reverse direction. This causes some of the hot combustion products to recirculate and ignite fresh air and fuel. The region where air and fuel initially mix is referred to the primary zone. The recirculation of combustion products causes a stable flame. Within the liner walls there are holes that admit air from the outer annulus to complete combustion and to lower the air temperature to a level that can be tolerated by the turbine blades. The region where air is admitted to lower the gas temperature is referred to the dilution zone.

Ideally, the temperature in the exit plane of a combustor should be as uniform as possible to preserve the life of the turbine blades. Nonuniform regions of temperature present in the turbine section due to poor mixing in a combustor can cause high thermal

stresses in the turbine blades [15]. The exit temperature distribution should also be coolest in the periphery because stresses are highest at the blade root, and also because the seals present at the blade tip needs to be protected [28].

An annular combustor is shown in Figure 6

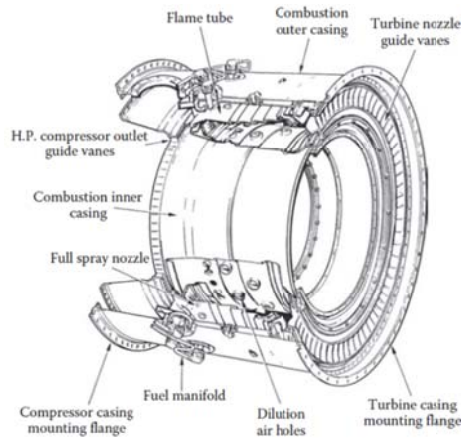


Figure 5: Conventional annular combustor [28]

Instead of combustion taking place within several cylindrical tubes, combustion takes place within the entire annular space. Annular combustors tend to be lighter, more compact, and suffer a smaller pressure loss as compared to the can type combustor. [29,31]. However, can combustors are easier to develop, service, and are structurally more rugged as compared to the annular type combustors. Typical pressure drops for a can type combustor and an annular type combustor are 7% and 5% respectively [31]. Aircraft in service today usually use an annular type combustor.

In addition to their geometrical layout, combustors can be also categorized by the manner in which they achieve low emissions. One such low emission combustor is the rich-burn/quick-quench/lean-burn. In a RQL combustor, combustion takes place in a fuel-rich primary zone. The lack of oxygen and the reduced temperatures in the primary zone retard  $\text{NO}_x$  production. Additional air needed to complete combustion is quickly

added and mixed uniformly with the primary zone gases to achieve a lean equivalence ratio (about 0.5 to 0.7) and a low exit temperature [28].

Another type of combustor used to achieve low  $\text{NO}_x$  is the lean direct injection (LDI) combustor. In an LDI combustor, all the air from the compressor is sent to the primary zone except that which was needed for liner cooling. Fuel and air are mixed via one swirler, or many smaller swirlers. Combustion takes place at a low equivalence ratio throughout the combustor as to keep the flame temperature low to discourage  $\text{NO}_x$  production [32].

## 2.9 Solver Theory

This report utilizes the finite volume method (FVM) to solve for the reacting flow field. In the FVM, the computational domain is subdivided into a finite number of control volumes. The integral forms of the governing equations are written for each control volume and the resulting equations are solved. The steady form of the governing equations in general form is

$$\int_A \rho \phi \mathbf{u} \cdot d\mathbf{A} = \int_A \Gamma_\phi \nabla \phi \cdot d\mathbf{A} + \int_V S_\phi dV$$

Equation 51: Transport equation for a general scalar  $\phi$

where  $\phi$  is a general scalar that represents mass flux, mean enthalpy, mixture fraction, and other relevant variables,  $d\mathbf{A}$  is a surface element of the area A, V is the volume of the control volume,  $\Gamma_\phi$  is a diffusion coefficient of  $\phi$ , and  $S_\phi$  is a source term. The integral and gradient term must be discretized in order to obtain a solution. The discretized form of Equation 51 is:



$$\sum_f^{N_f} \rho_f \mathbf{u}_f \phi_f \cdot \mathbf{A}_f = \sum_f^{N_f} \Gamma_{\phi f} \nabla \phi \cdot \mathbf{A}_f + S_\phi V$$

Equation 52: Discretized form of governing equations

where  $N_f$  is the number of faces of a control volume, and the subscript  $f$  denotes the face value of the control volume. The scalar values are stored in the center of each control volume. To obtain the scalar values at the cell faces, a second order upwind scheme is used for the can type combustor geometry. When the second order upwind scheme was used for the annular type combustor geometry, the solution did not converge. To remedy this, a first to higher order blending scheme is used. Its accuracy is midway between that of a first order upwind scheme and a second order upwind scheme. For further details, refer to the FLUENT theory guide [2]. The gradient term is computed using the least squares cell based method.

FLUENT's segregated solver is used to solve the governing equations. Each equation is solved sequentially and uncoupled from one another. After guessing an initial solution, the momentum equations are solved. Then, a pressure correction equation is solved that corrects the mass fluxes at each face so that the continuity equation is satisfied. The SIMPLE algorithm is used to obtain the pressure correction equation. After the mass fluxes are corrected, equations for turbulent quantities, mixture fraction, mixture fraction variance, and radiation intensity are solved. Then the source terms are updated from the discrete phase quantities. If convergence is not obtained after the source terms are updated, then this process repeats until one has a converged solution.

Convergence is judged by monitoring the residuals. Once the residuals stop changing, contours of temperature, velocity, species, and other relevant variables are

monitored while running more iterations. If the contours do not exhibit any noticeable changes, then the solution is considered converged.

### *2.10 Literature Review*

Some of the research work regarding  $\text{NO}_x$  reduction in gas turbine combustors are presented in this section, focusing is on aircraft combustors. Representative  $\text{NO}_x$  and CO emission levels and trends for various combustors are presented for comparison with the results presented in this thesis. Also presented in this section are reported maximum flame temperatures from studies which used  $\text{C}_{12}\text{H}_{23}$  as the molecular formula for kerosene. This serves as a form of validation for the results in this thesis since there is no experimental data presented for the SUE combustor as of yet.

Rosfjord et al. [33] conducted an experimental study on a scale model of a LDI stationary gas turbine which utilized the RQL concepts for different liquid synthetic fuels which contained fuel-bound nitrogen. They varied the operating pressure and residence time and studied their effect on  $\text{NO}_x$  and smoke emissions. They found the  $\text{NO}_x$  emissions to be insensitive to fuel bound nitrogen content, operating pressure, and residence time. They have quoted  $\text{NO}_x$  levels as low as 37 ppm could be achieved with the RQL concept.

Hussain et. al [34] performed experiments on a jet type mixing combustor that uses jets of air, rather than a swirler to achieve mixing of fuel and air. About 10 ppm of  $\text{NO}_x$  in the exit plane was achieved because the jets of air were able to mix with the fuel in a rapid and efficient manner. Good combustion efficiency and flame stability was also achieved. It was reported that the jet type mixing combustor had  $\text{NO}_x$  emissions on par with premixed systems without the stability issues

Tancia [35] presented results from experimental studies performed on RQL, LPP, and LDI combustors with the intent to find correlations for  $\text{NO}_x$ . He reported that the LPP and LDI combustors had the lowest  $\text{NO}_x$  emissions compared to the RQL combustors, but the LPP suffered from instability issues. It was claimed that the RQL combustors could approach the emission levels of the LPP combustor if the quench step was improved. He reported that there was no definite pressure dependence on  $\text{NO}_x$  production for the three combustor types.

Valachovic [36] performed CFD calculations on a turbofan combustor at idle power conditions to see the effects of the variation of liner-wall cooling on CO and UCH emissions. It was found that UCH and CO emissions increased with liner wall cooling. The highest CO emission index value found from experiment is 100 g/kg fuel.

Talpallikar et. al [7] performed a parametric study using CFD on a relatively simple combustor to see how the design of the quick mix section of an RQL combustor effects  $\text{NO}_x$  emissions. They varied the slot aspect ratio of the jets that are responsible for quickly bringing the equivalence ratio from rich to lean as well as the momentum flux ratio between the quick-mix jets and the liner air flow. They found that the  $\text{NO}_x$  levels were very sensitive to both momentum flux ratio and slot aspect ratio. The study showed that the quick mix section must be carefully designed in order to obtain low  $\text{NO}_x$  emissions.

Meisl et. al. [37] studied the effect of operating pressure and primary equivalence ratio on  $\text{NO}_x$  formation in an RQL combustor using the perfectly stirred reactor (PSR) concept and by experiment. Three conditions were studied, a low power condition, medium power condition, and high power condition and totally fixed nitrogen (TFN)

concentrations were taken in the primary zone, and in the exhaust gases. It was found that for each condition, there existed an optimal equivalence primary equivalence ratio which produced the lowest  $\text{NO}_x$ . This optimum equivalence ratio decreased with increasing pressure. Furthermore, the increase in pressure did not affect the TFN concentration in the rich primary zone, but had a significant effect in the lean zone.

Datta and Som [38] performed numerical studies on a Lean Direct Injection (LDI) combustor which uses liquid n-hexane as the fuel. They studied effect of pressure and swirl number on  $\text{NO}_x$  emissions. The air was at a temperature of 1060 R (589 K) and an equivalence ratio of approximately 0.25 was used. They performed calculations with the pressure at 14.5 psi (1 bar) and at 87 psi (6 bar) and found the  $\text{NO}_x$  levels at the exit to be 19.16 ppm and 203 ppm respectively. These values were at a swirl number of 0.76, which is considered to be moderately swirling flow.

Zarzas et. al. [39] performed an experimental study on an RQL combustor which utilized a conventional swirler to stabilize the flame. They performed a parametric study to see how  $\text{NO}_x$  and soot values vary with operating pressure and air-fuel ratio (AFR). The inlet air temperature was 1300 R (722 K) and the pressure was varied from 87 psi (6 bar) to 275 psi (19 bar). The  $\text{NO}_x$  production increased with operating pressure for all cases. The  $\text{NO}_x$  levels also rose with AFR up to stoichiometric conditions then decreased for rich fuel conditions.

Tancia et. al. [40] performed an experimental study on a lean-direct injection combustor using various inlet temperatures, swirler configurations, operating pressures, and flame temperatures. For an inlet temperature of 810K, an inlet pressure of 400 psi (27.6 bar), and a flame temperature of 1800 K the  $\text{NO}_x$  emission index is less than 6.

They were also able to find correlation between inlet temperature, inlet pressure, fuel-air ratio, and swirler pressure drop which fit well for their cases.

Bank et. al. [41] describes the development of an axially staged lean-premixed partially-pre-vaporized (LP(P)) combustor. The residence time of the fuel in the prevaporizer is much smaller than the auto-ignition delay time, which prevents auto-ignition and flashback. The  $\text{NO}_x$  emission index never exceeded 4 g/kg fuel at high temperature and pressure conditions, but the combustor suffered stability issues close to lean blow out (LBO) conditions. To remedy this, a RQL pilot burner was added, which improved stability, but raised  $\text{NO}_x$  levels. At an operating pressure of 72 psi (5 bar) and a temperature ranging from 400K to 535K, the  $\text{NO}_x$  emission index for only the RQL pilot burner ranged from 0.1 to 7.1 g/kg fuel, and the CO emission index ranged from 38 to 66 g/kg fuel for

Straub et. al. [42] performed experimental and numerical simulation of a stationary RQL Trapped Vortex Combustor (TVC). Studies were conducted with the inlet temperature at 700 F (644 K), the pressure at 147 psi (10.1 bar), and the fuel as gaseous methane. It was found that the  $\text{NO}_x$  levels decreased with increasing cavity equivalence ratio up to about an equivalence ratio of about 1.6 then the  $\text{NO}_x$  levels very slowly increased after that. The CO levels did not increase with cavity equivalence ratio up to about a value of 2 then the CO levels slowly increased after that. They claimed that their TVC combustor can obtain a theoretical lower limit of 10 ppm of  $\text{NO}_x$  levels if the mixing is perfect.

Puster et. al. [1] has performed some numerical studies on the SUE combustor presented in this thesis, although the combustor in this thesis contains some slight

modifications to the geometry. They have reported that the sudden expansion combustor produced about 45 parts per million (ppm) of  $\text{NO}_x$  at the exit plane of the combustor for high power conditions (equivalence ratio is about 1) and about 4 ppm of  $\text{NO}_x$  at moderate power conditions. They used two types of liquid fuels. This thesis extends their work to provide  $\text{NO}_x$  and CO characteristics for a wide range of operating conditions.

Patel et. al. [43] performed an experimental and CFD study on a LDI combustor using  $\text{C}_{12}\text{H}_{23}$  as their fuel. The air inlet conditions are 294 K and 1 atm. It was found that they had a maximum temperature of 2350 K and 2646 K. The  $\text{NO}_x$  and CO maximum at the centerline are 700 ppm and about 650 ppm respectively.

Frassoldati et. al. [8] performed an experimental and CFD analysis of a LPP combustor for a turbofan engine. Their CFD model used a 20 degree angular sector which captured a section of the fuel injector/swirler assembly. They used  $\text{C}_{12}\text{H}_{23}$  as the fuel and reported a maximum temperature between 2300 K to 2500 K. They also provided plots of radially averaged NO and CO as a function of the azimuthal angle of the combustor. The peak NO concentration encountered in the combustor was around 500 ppm to 600 ppm while the CO concentrating peaked at around 600 ppm.

Yamamoto et. al. [44] performed experiments on a combustor which utilized a triple swirler which can create a nonpremixed flame and/or a premixed flame, depending upon the power conditions. The fuel utilized is kerosene; their reported maximum flame temperature is 2286 K. They performed a parametric study on how  $\text{NO}_x$ , CO, smoke, and unburned hydrocarbons (UHC) varied as a function of operating points during a landing take off cycle (LTO). It was found that 100% maximum take-off thrust (a combustor pressure of 380 psi (26.2 bar) and an inlet temperature of 787 K), the  $\text{NO}_x$  emission index

was no more than 9 g/kg fuel and the CO was no more than 60 g/kg of fuel. When only the nonpremixed mode of the swirler was used, the NO<sub>x</sub> emissions were no more than 16 g/kg fuel.

### 3. GEOMETRY, MESH, AND BOUNDARY CONDITIONS

This section describes the geometry of both the can type and the annular type combustors. Then it discusses some of the geometrical simplifications needed to bring the computational efforts down to a manageable level. Then the mesh for both combustors is described. Finally, the boundary conditions for the various cases are presented.

#### 3.1 Geometry

The can type combustor is shown in Figure 1 and also in Figure 7

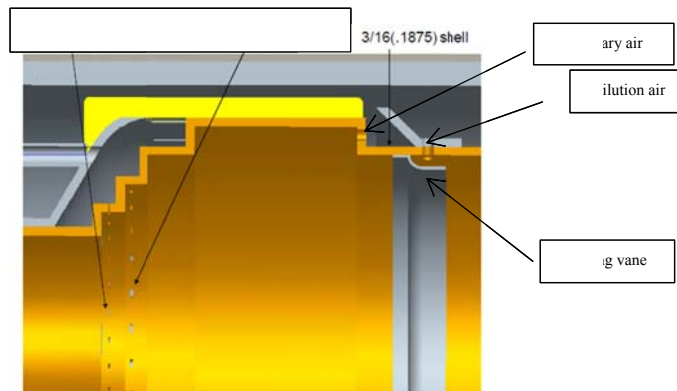


Figure 6: Primary combustion zone for can type combustor.

The sudden expansion combustor contains no swirler. This has the added advantage of being easier to manufacture and it has a lower pressure loss compared to combustors with swirlers. Its operation is as follows: air enters the liner inlet plane at around 200 ft/s to 300 ft/s. The air passes through the step region and undergoes a sudden expansion. This sudden expansion creates a low speed recirculation region that stabilizes the flame. The



slots shown in Figure 7 are for fuel injection. Fuel is injected in a direction normal to the incoming flow in the first and second steps. Also shown in Figure 7 is secondary air that is injected opposite to the incoming airflow to create the recirculating flow region. The dilution holes lower the temperature of the hot gases so that the  $\text{NO}_x$  emissions can be reduced. The dilution air is directed by cooling vanes as to keep the liner wall from overheating.

If the flow within the inner and outer annulus is computed, the number of elements in the mesh would be on the order of 10 million elements. Performing an analysis with that many elements requires vast computational resources that renders a parametric study impractical. In light of this, the combustor geometry is simplified. The first simplification is the removal of the outer annulus. This reduces the computational effort to a manageable level. The interaction between the outer annulus and the liner is approximated by using boundary conditions on the dilution holes. This has the added advantage of being able to control the optimal amount of flow through the dilution holes to reduce  $\text{NO}_x$ . The second simplification made to the geometry was to only model an angular sector of the combustor. A 30 degree sector of the can combustor is modeled in place of the whole combustor. The computational domain for the can combustor is shown in Figures 8 and 9:

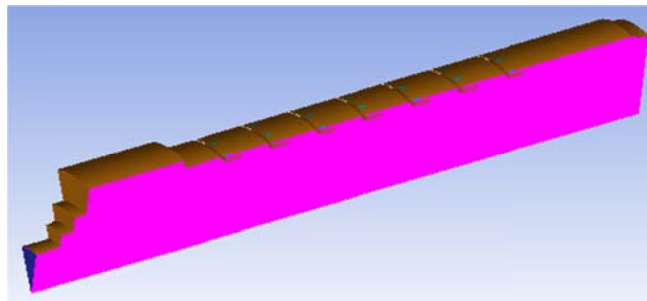


Figure 7: Can combustor picture showing the dilution holes and primary air slot

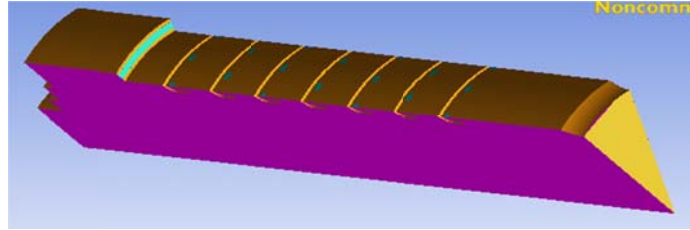


Figure 8: Backside of can combustor

The dark blue surface is the inlet for the primary air. The pink surfaces represent symmetry boundary conditions which are used to approximate the 3-dimensional flow field. The brown surface represents the liner walls and cooling vanes. The teal colored circles represent dilution holes. A scale drawing for the can type combustor is shown in Figure 9

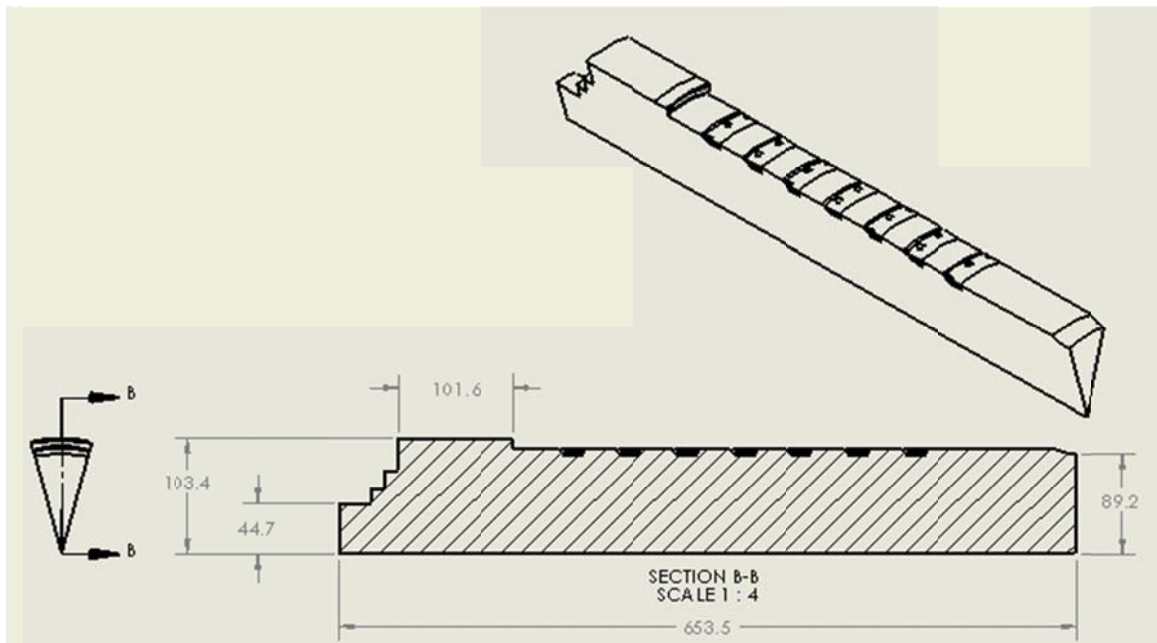


Figure 9: Scale drawing of the can type combustor (units in mm)

Figure 10 shows a side view of a sample calculation of the liquid droplet trajectories to show the arrangement of all the fuel injectors:

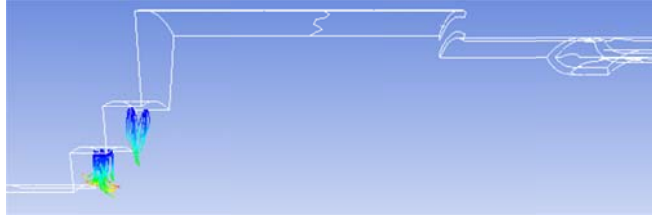


Figure 10: Side view of liquid droplet trajectories

Figure 11 shows a view if one were to look downstream of the combustor.

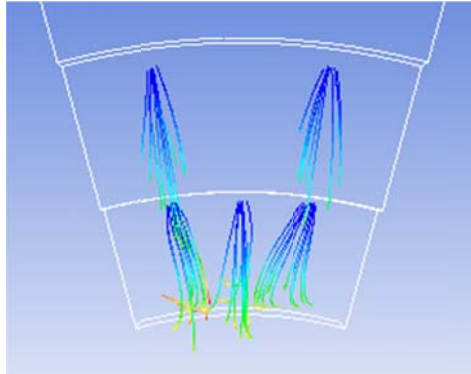


Figure 11: Downstream view of droplet trajectories

For the can combustor, there are 5 injection points. The bottom three injectors are spaced 10 degrees apart and the top two are spaced 7.5 degrees.

The annular combustor is shown in Figure 12 and 13

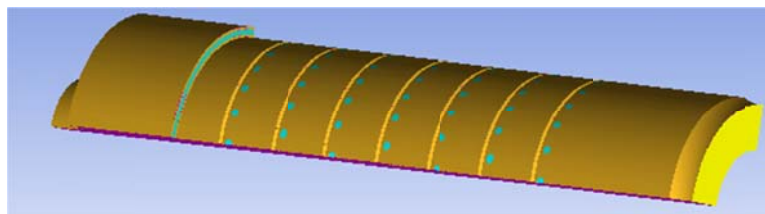


Figure 12: Annular combustor isometric view

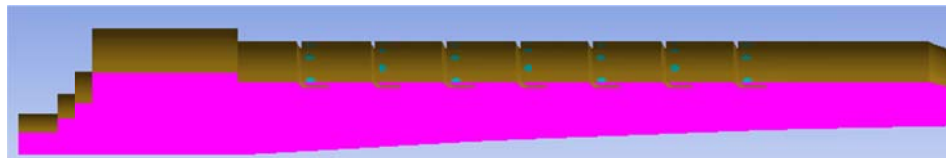


Figure 13: Annular combustor side view

Instead of modeling the whole combustor, a 90 degree sector of the combustor is modeled. A scale drawing is shown below is Figure 14

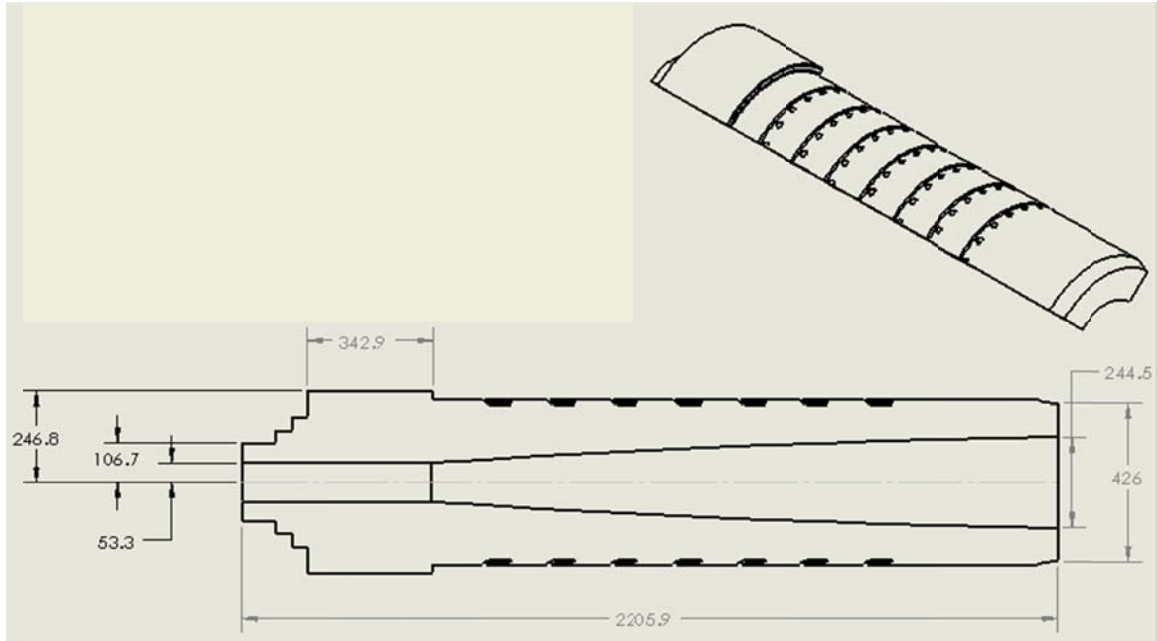


Figure 14: Scale drawing of the annular type combustor (units in mm)

The fuel injection configuration is shown in Figure 15

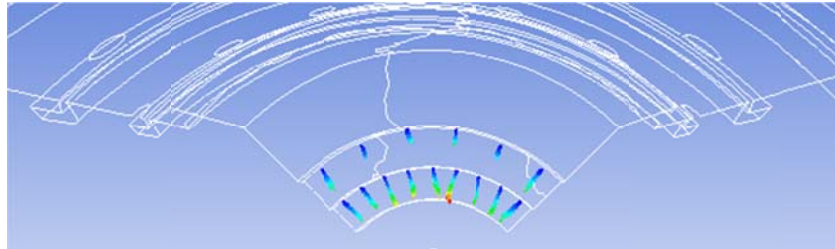


Figure 15: Annular combustor fuel injection arrangement

Here, there are 15 injectors, 6 on the top step spaced 10 degrees apart and 9 on the bottom spaced 7.5 degrees apart.

### 3.2 Mesh

The mesh is generated using ICEM CFD. Since the geometry is quite complex, an unstructured mesh is used. Several types of elements were tested and the tetrahedral elements produced the best results. The mesh for the can combustor is shown below:

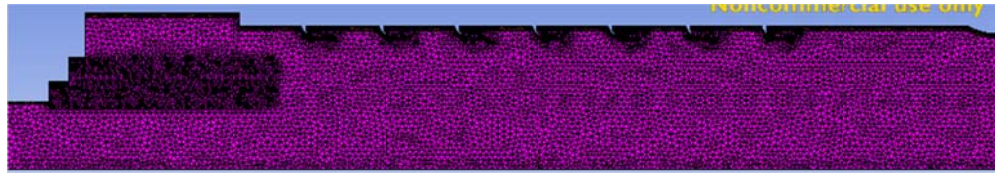


Figure 16: Can combustor mesh side view

648,000 elements are used in Figure 16. An additional mesh was created with 1.9 million elements so a mesh independent study can be performed. Contours of velocity magnitude and temperature are shown in Figures 17-18 for both meshes.

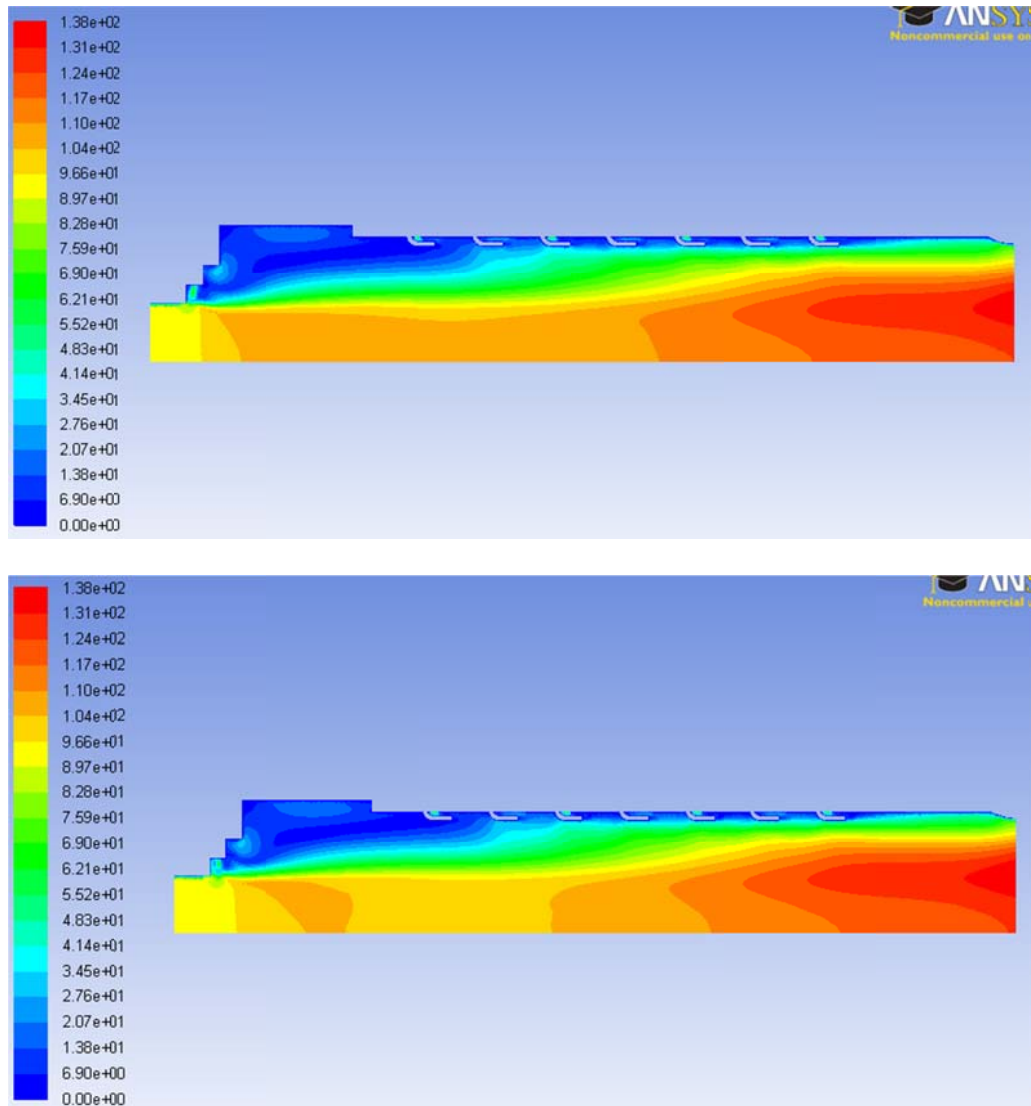


Figure 17: Contours of velocity magnitude (m/s) The top picture shows the mesh with 600,000 elements and the bottom shows the mesh with 1.9 million elements

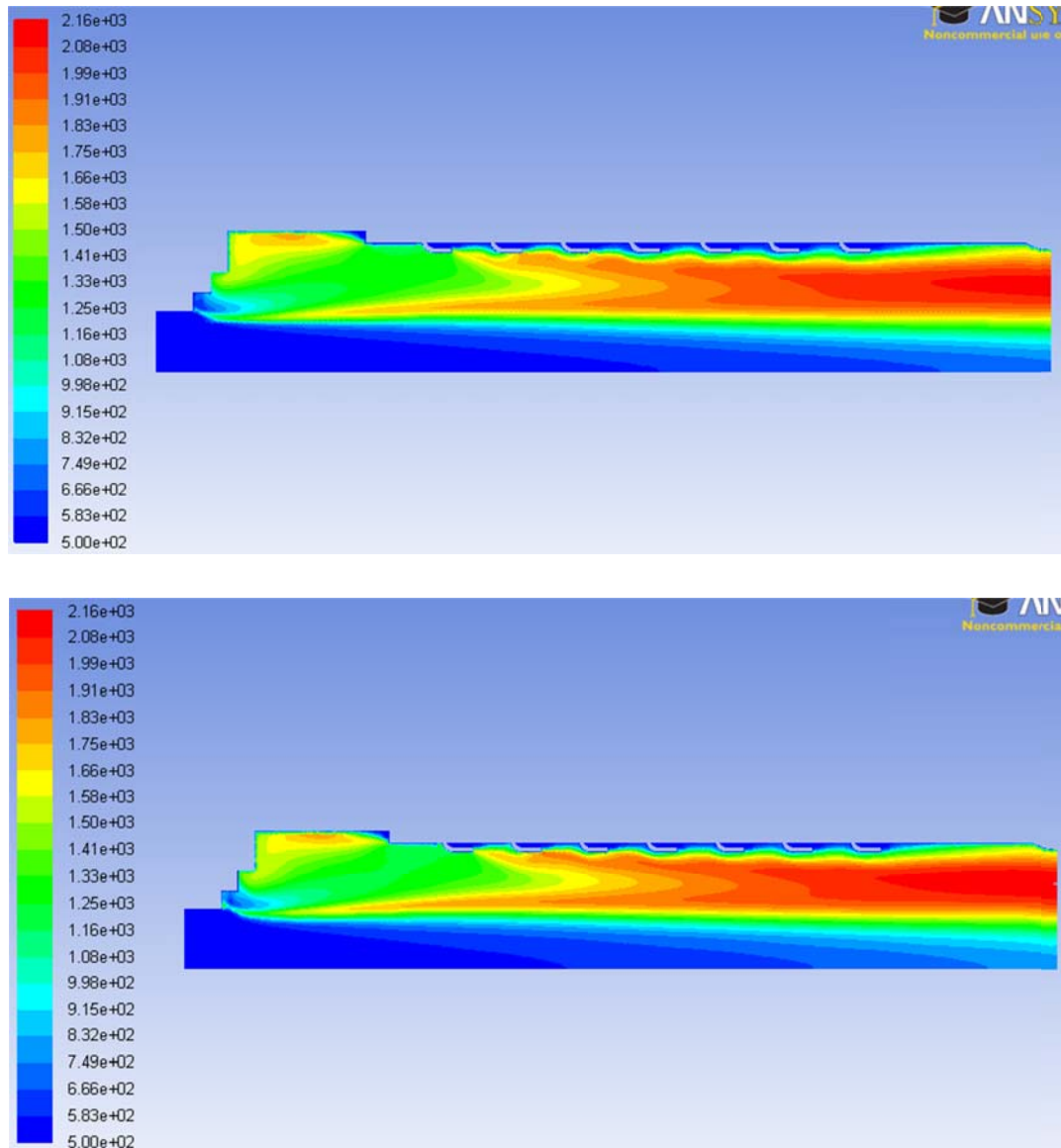


Figure 18: Contours of temperature (K) The top picture shows the mesh with 600,000 elements and the bottom shows the mesh with 1.9 million elements

Observing Figures 17 and 18, one sees that the results are very similar for both meshes.

Therefore, the 600,000 mesh is considered sufficient to resolve the flow field.

The mesh for the annular combustor is shown below in Figure 19:



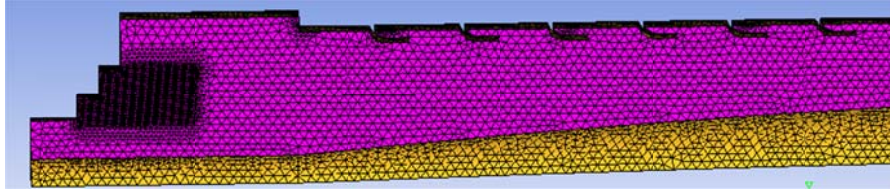


Figure 19: Annular combustor mesh

The mesh for the annular combustor is composed of 906,000 elements. A mesh independent study was performed for this mesh as well; the corresponding contours of velocity and temperature are shown below in Figures 20-21

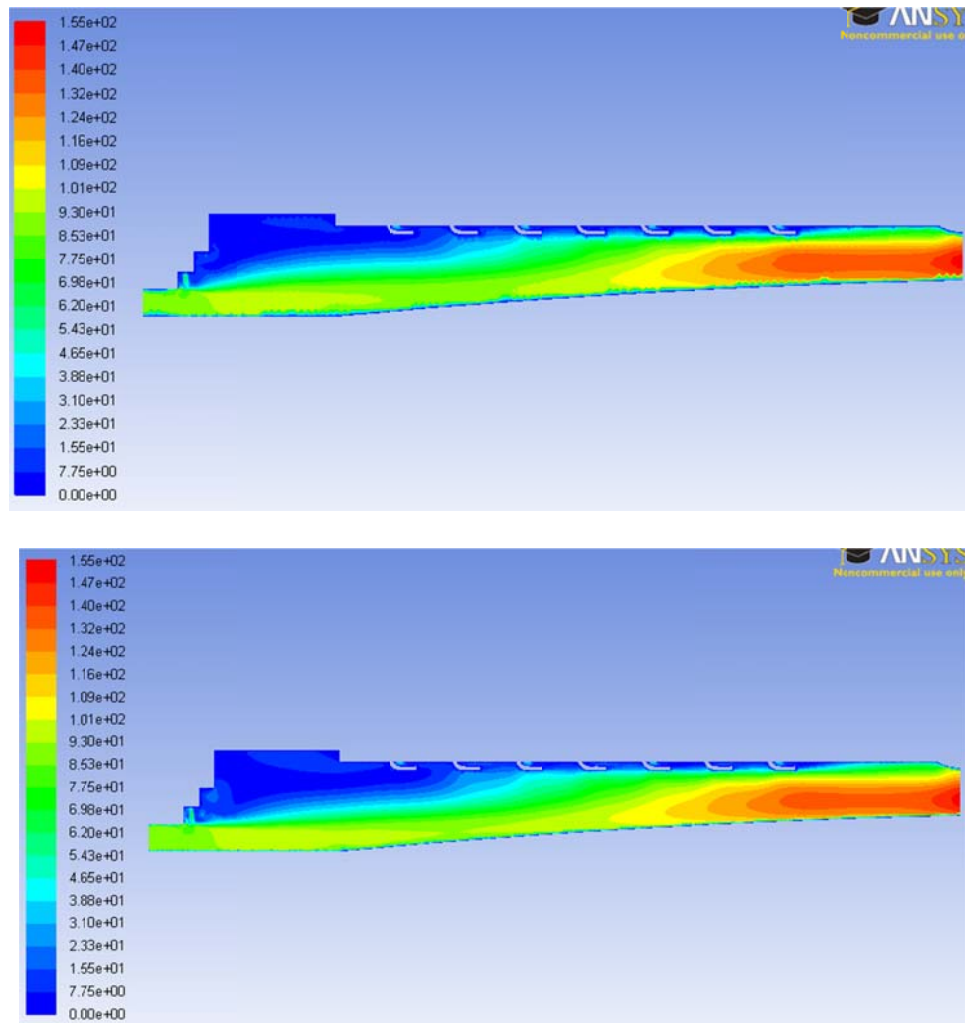


Figure 20: Contours of velocity magnitude (m/s) The top picture shows the mesh with 900,000 elements and the bottom shows the mesh with 4.5 million elements



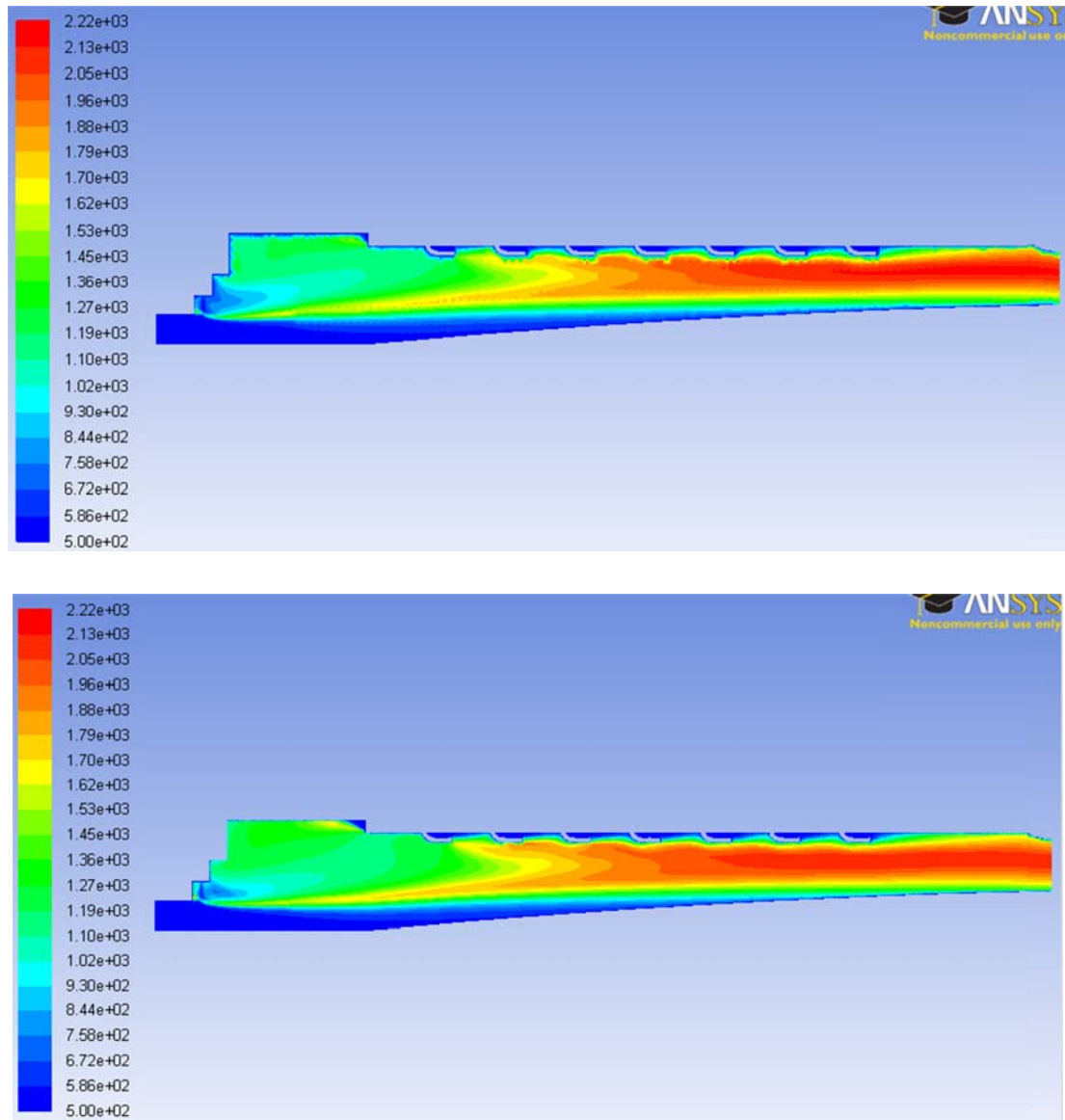


Figure 21: Contours of temperature (K) The top picture shows the mesh with 900,000 elements and the bottom shows the mesh with 4.5 million elements

There is little change between the 900,000 element mesh and the 4.5 million element mesh, so the results are considered mesh independent.

### *3.3 Boundary Conditions*

The boundary conditions common to both combustors is shown below in Table 1

Turbulence Intensity	10%
Air Inlet Temperature	556 K
Wall Temperature	556 K
Droplet Diameter	10 $\mu\text{m}$
Droplet Temperature	300 K
Cone Angle	30°
Cone Radius	0.03125 in (0.79 mm)
Initial Fuel Velocity	600 ft/s (183 m/s)
% Primary Air	65.50%
% Secondary Air	3.13%
% Dilution Air	31.40%

Table 1: Boundary conditions common to both combustors

The turbulence intensity represents the ratio of the root-mean square velocity to the mean velocity and is taken to be 10% to represent moderately turbulent flow coming from the diffuser. The integral length scale is taken to be 7% of the hydraulic diameter [14]. The air and wall temperature is taken to be 556 K to be representative of the temperature of the air exiting a high pressure compressor. The velocity, temperature, and turbulence quantities are all assumed to be uniform at the inlets. % Primary Air, % Secondary Air, and % Dilution Air represent how much of the total airflow is split among the air coming from the inlet, the annular cooling slot, and the dilution holes respectively. The air

distribution was chosen so that a fuel-rich flame can exist in the primary zone, and a fuel-lean region is present towards the exit of the combustor as per the RQL methodology.

The kerosene droplets are injected into the computational domain in the shape of a solid cone as shown in Figure 22

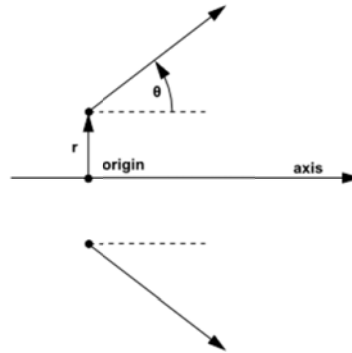


Figure 22: Fuel injection diagram [2]

$r$  represents the Cone Radius in Table X and  $\theta$  represents the Cone Angle. The diameters of the droplets are specified as  $10\text{ }\mu\text{m}$  as to represent a finely atomized spray as done in reference 29. The particles are all injected at a velocity of  $600\text{ ft/s}$  ( $183\text{ m/s}$ ) with a temperature of  $300\text{ K}$ .

The velocities for the inlets for the can type combustor and annular type combustor are shown below in Table 2 and Table 3:

Can Combustor Velocity	
Primary Air Velocity	300 ft/s (91 m/s)
Dilution Air Velocity	170 ft/s (52 m/s)
Secondary Air Velocity	30 ft/s (9 m/s)

Table 2: Can Type Combustor Inlet Velocities

Annular Combustor Velocity	
Primary Air Velocity	280 ft/s (85 m/s)
Dilution Air Velocity	120 ft/s (37 m/s)
Secondary Air Velocity	12 ft/ (4 m/s)s

Table 3: Annular type Combustor inlet velocities

The operating pressure is changed from 300 psi (20.7 bar) to 100 psi (6.9 bar) in increments of 50 psi (3.4 bar). Each of the five operating pressure cases to be studied has different mass flow rates for each inlet since the density changes with operating pressure. For a fixed operating pressure, the global equivalence ratio is changed from 0.9 to 0.5 in increments of 0.1. To change the equivalence ratio for a fixed operating pressure, the fuel flow rate was varied while the air mass flow rates were kept constant.

## 4. RESULTS

The CFD analysis of the can type and the annular type combustor are presented in this section. The results of different turbulence models, combustion models, and radiation models are presented to show the differences between the models. Finally, the results of the parametric study are presented for both combustor types.

### *4.1 Reacting Flow Fields of the Can Type and Annular Type Combustors*

Detailed results for the can and the annular type combustors are shown for the case of an operating pressure of 300 psi (20.7 bar) and a global equivalence ratio of 0.7. Various contour information shown about the mid-plane of each combustor type. Contours of velocity magnitudes are shown first for both combustors:

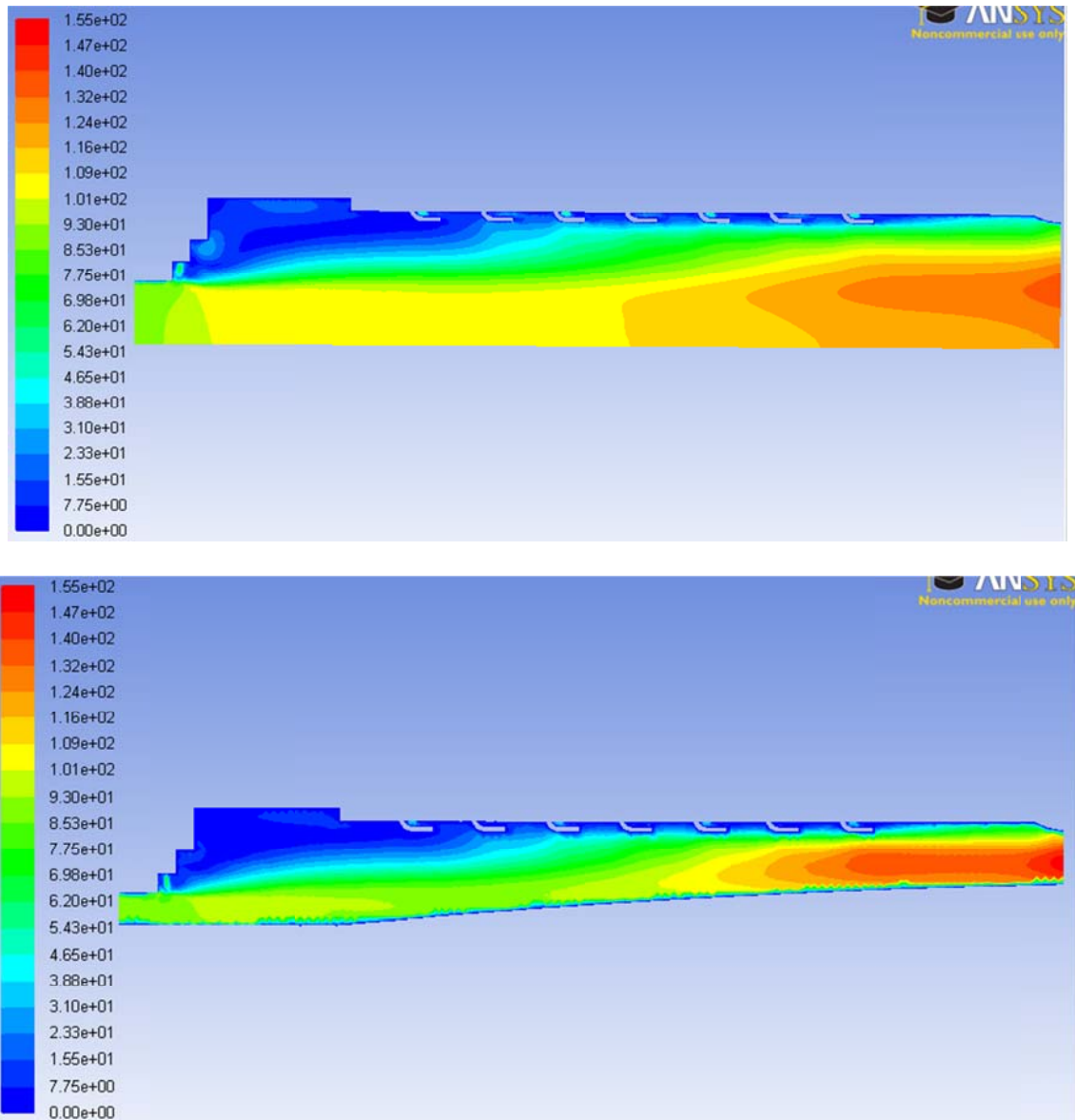


Figure 23: Contours of velocity magnitude for both combustors (m/s). The top picture shows the can type combustor and the bottom figure is the annular type combustor.

The low velocity region after the step expansion can clearly be seen in Figure 23. The high velocity region in the first step is due to the liquid spray entraining the air around it. The Mach numbers at the exit plane for both the can combustor and annular combustor are no greater than 0.15 and 0.16 respectively, justifying the use of the incompressible

flow assumption. The corresponding velocity vector fields for the sudden expansion primary zone regions are shown below for velocities between 0 and 61 m/s:

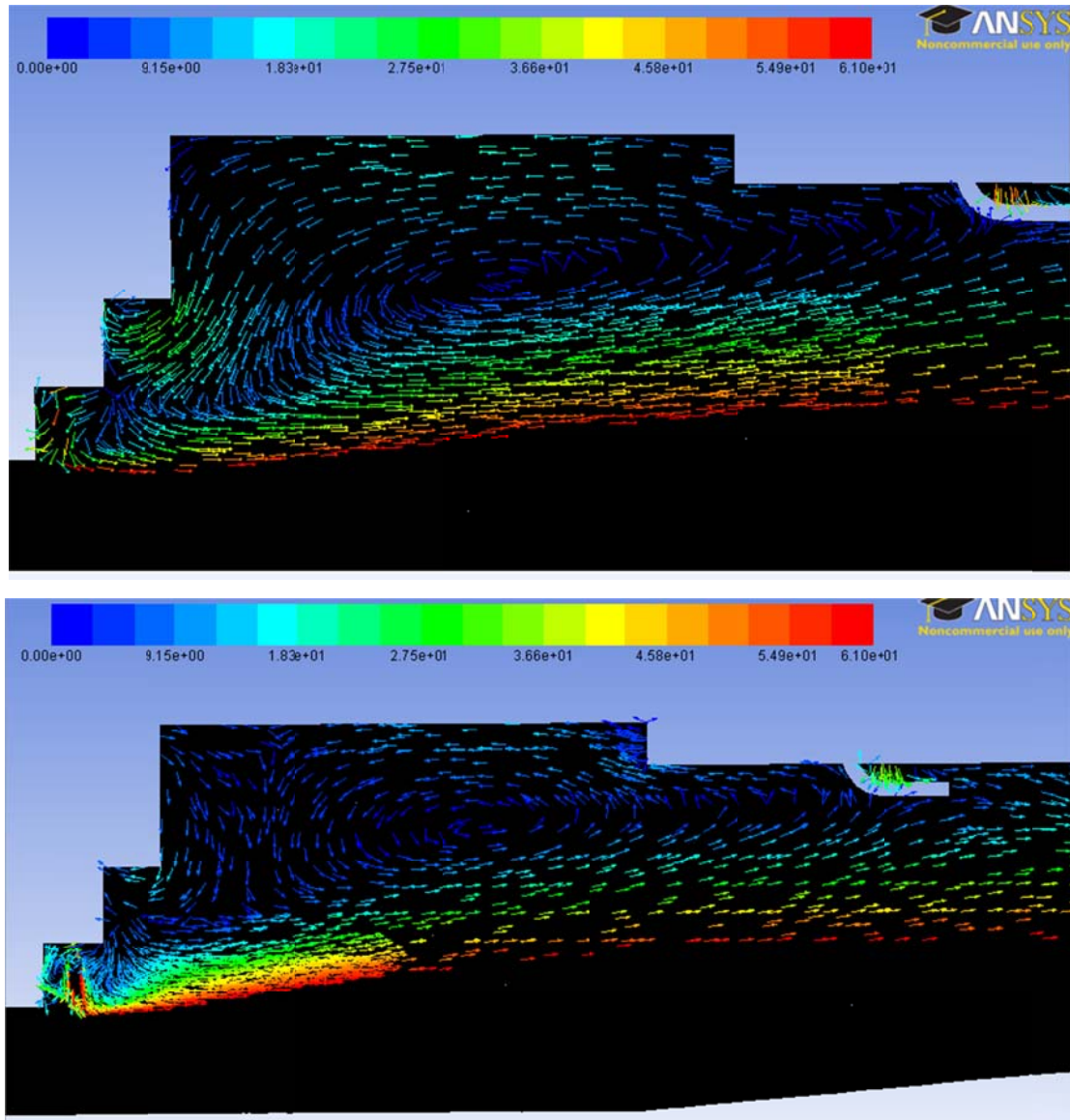


Figure 24: Vector field colored by velocity magnitude (m/s). The top picture shows the can type combustor and the bottom figure is the annular type combustor.

In these above figures, one sees the recirculation region that is designed for anchoring the flame in both combustors. The velocity that flows inward radially near the second step in the can combustor is much higher than the flow in the second step in the annular

combustor due to the higher velocity of the secondary air jets in the can combustor. The velocity fields for the entire primary region are shown below in Figure 25:

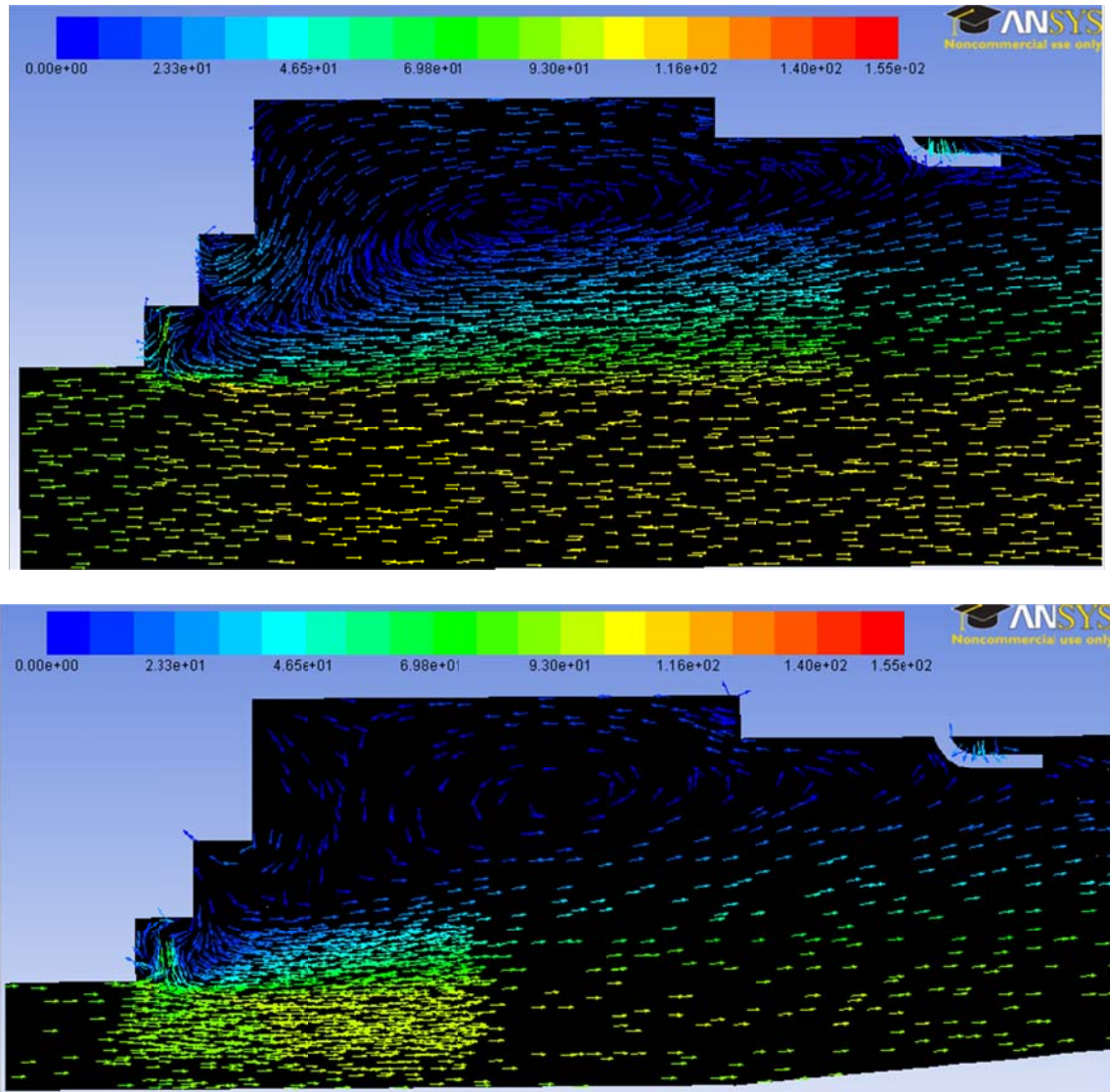


Figure 25: Primary zone velocity vectors (m/s). The top picture shows the can type combustor and the bottom figure is the annular type combustor.

For both combustors, the high velocity air entering from the primary inlet keeps its forward momentum after passing the sudden expansion step region. Air from the secondary jet, in each case, is directed towards the step region to mix with the vaporized fuel. The high velocity air from the primary inlet and the low velocity air from the



secondary inlet create a strong shear flow that mixes the air and fuel vapor escaping the primary region. This can also be deduced from the contours of corresponding turbulent kinetic energy shown in Figure 26:

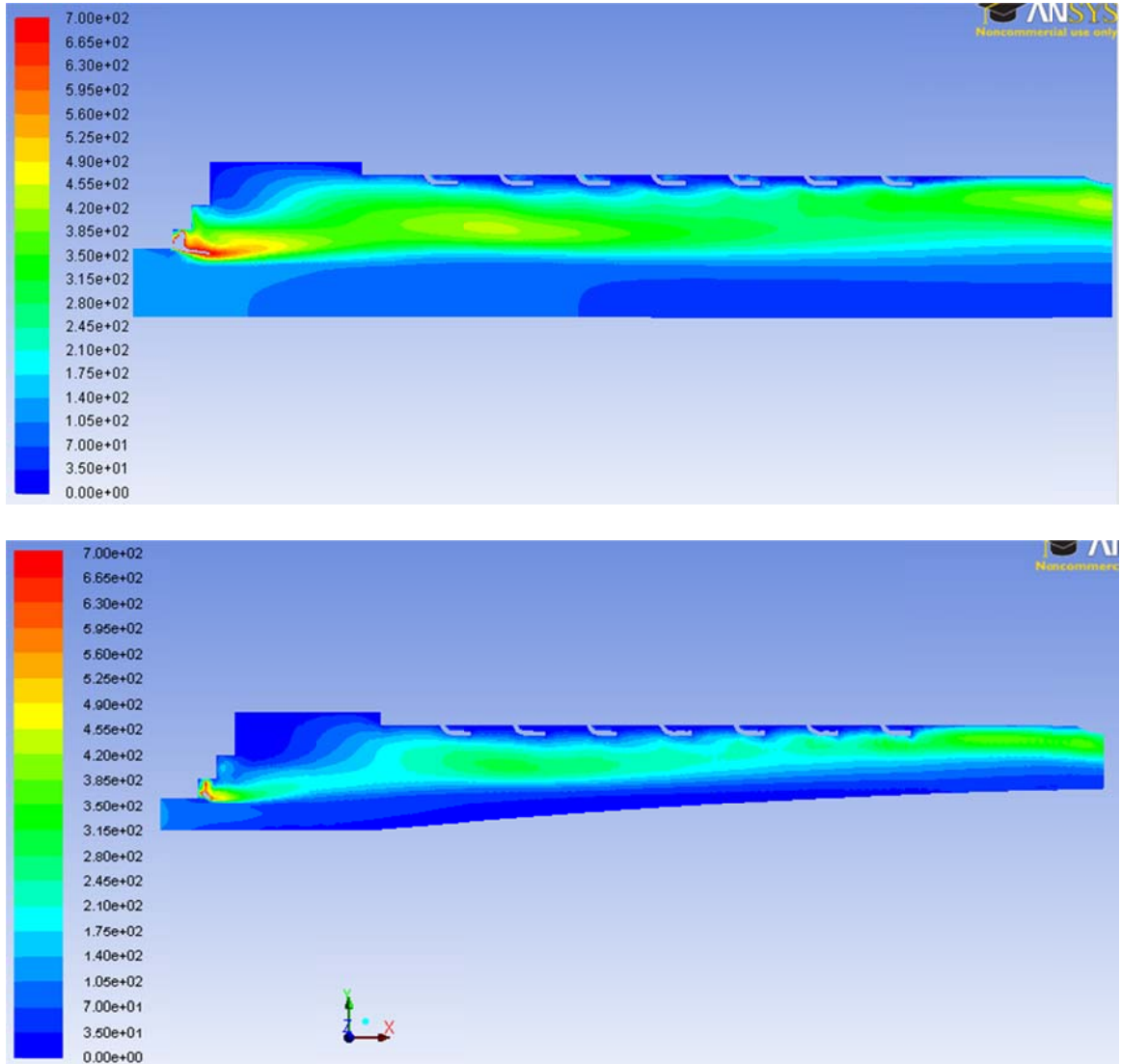


Figure 26: Contours of turbulent kinetic energy ( $\text{m}^2/\text{s}^2$ ). The top picture shows the can type combustor and the bottom figure is the annular type combustor.

From the above figure, one can see that the region of high turbulent kinetic energy for the annular combustor is far less than the can combustor due to the lower wall in the annular combustor.

The velocity field near for the cooling vanes are shown below in Figure 27:

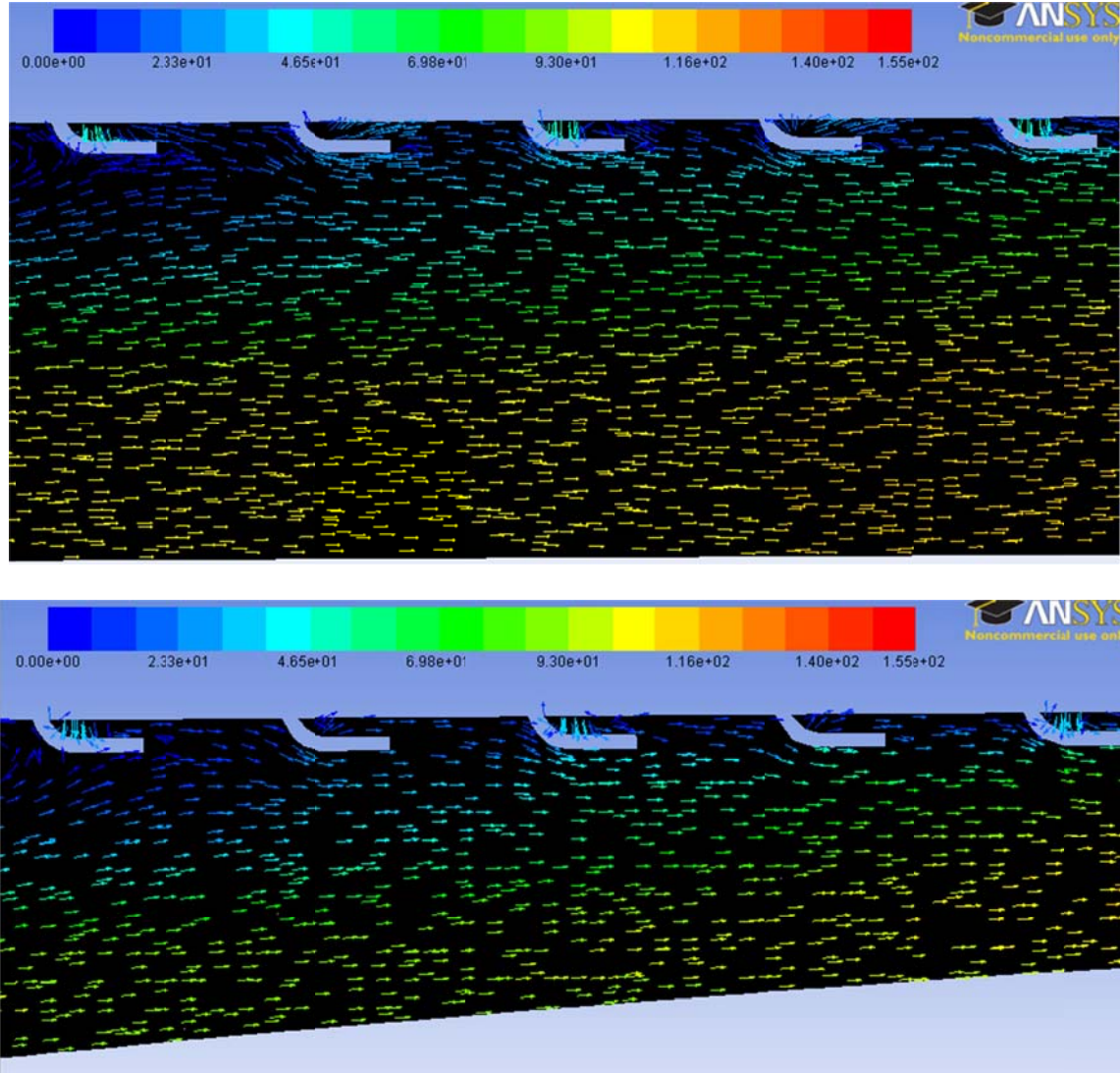


Figure 27: Vector field for cooling vanes (m/s). The top picture shows the can type combustor and the bottom figure is the annular type combustor.

The air from the cooling vanes does not penetrate into the main flow like in other conventional combustors to lower the temperature of the combustion products. Rather, the air from one vane brushes the back of the vane in front of it. The primary purpose of the cooling vanes in the preliminary design of the SUE combustor was to keep the liner temperature as low as possible.

The contours of local equivalence ratio are shown below in Figure 28:

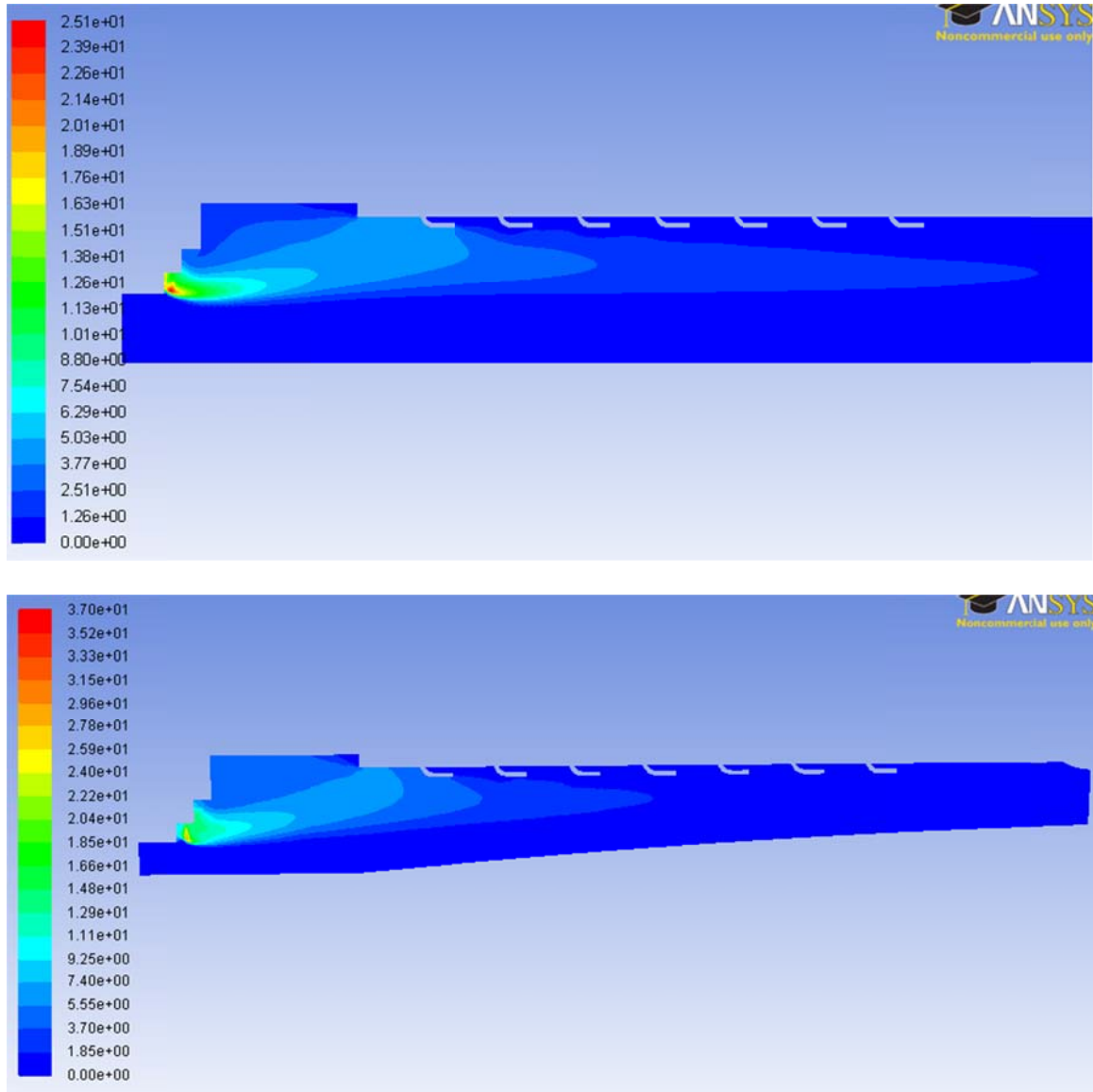


Figure 28: Contours of local equivalence ratio. The top picture shows the can type combustor and the bottom figure is the annular type combustor.

The fuel rich region extends far away from the primary zone for both combustors: the situation is worse for the can type combustor. In conventional RQL combustors, the rich region is much smaller than the SUE combustor's rich region, and the lean region is much larger than in the SUE combustor. The demarcation between the fuel-rich region and the fuel-lean region is better shown in Figure 29:

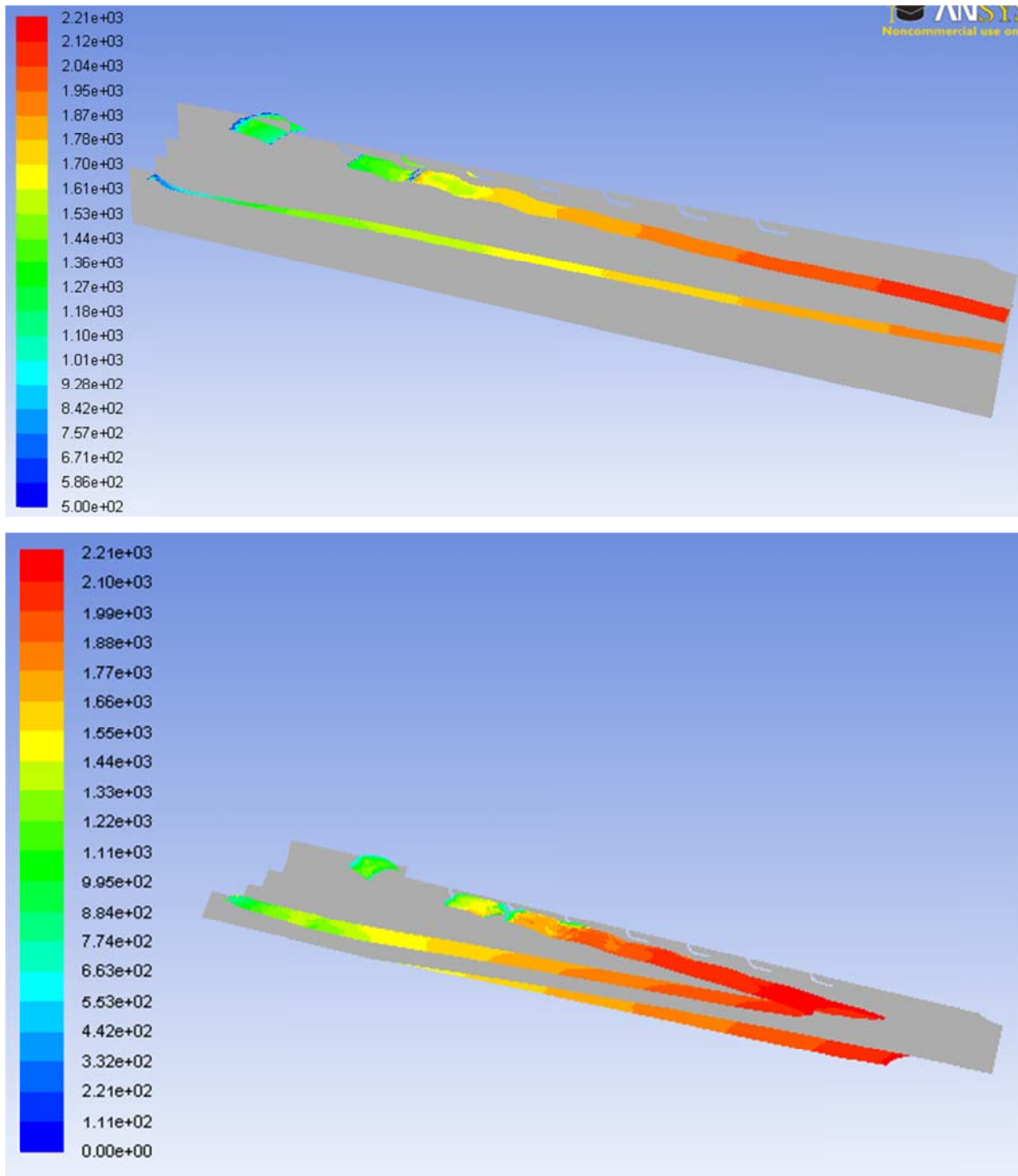


Figure 29: Iso-surface of equivalence ratio equal to unity. Temperature contours (in units of kelvin) are plotted on this iso-surface. The top picture shows the can type combustor and the bottom figure is the annular type combustor.

In Figure 29, an iso-surface of equivalence ratio equal to unity is plotted with temperature contours on its surface. The region bounded between the upper and lower surface is fuel rich while the region outside it is fuel lean. It can be seen the fuel rich region for the can

type combustor extends to the exit plane, which means there is a large region where fuel is unburned. Since the annular type combustor is 3.33 times longer than the can type combustor, the annular type combustor has more length to mix the fuel-air mixture so that a lean mixture is produced in the exit plane.

Contours of  $C_{12}H_{23}$  mass fraction are shown below in Figure 30. It can be seen that the strength of the recirculation region in the primary zone is insufficient to contain the fuel vapor within the primary region.

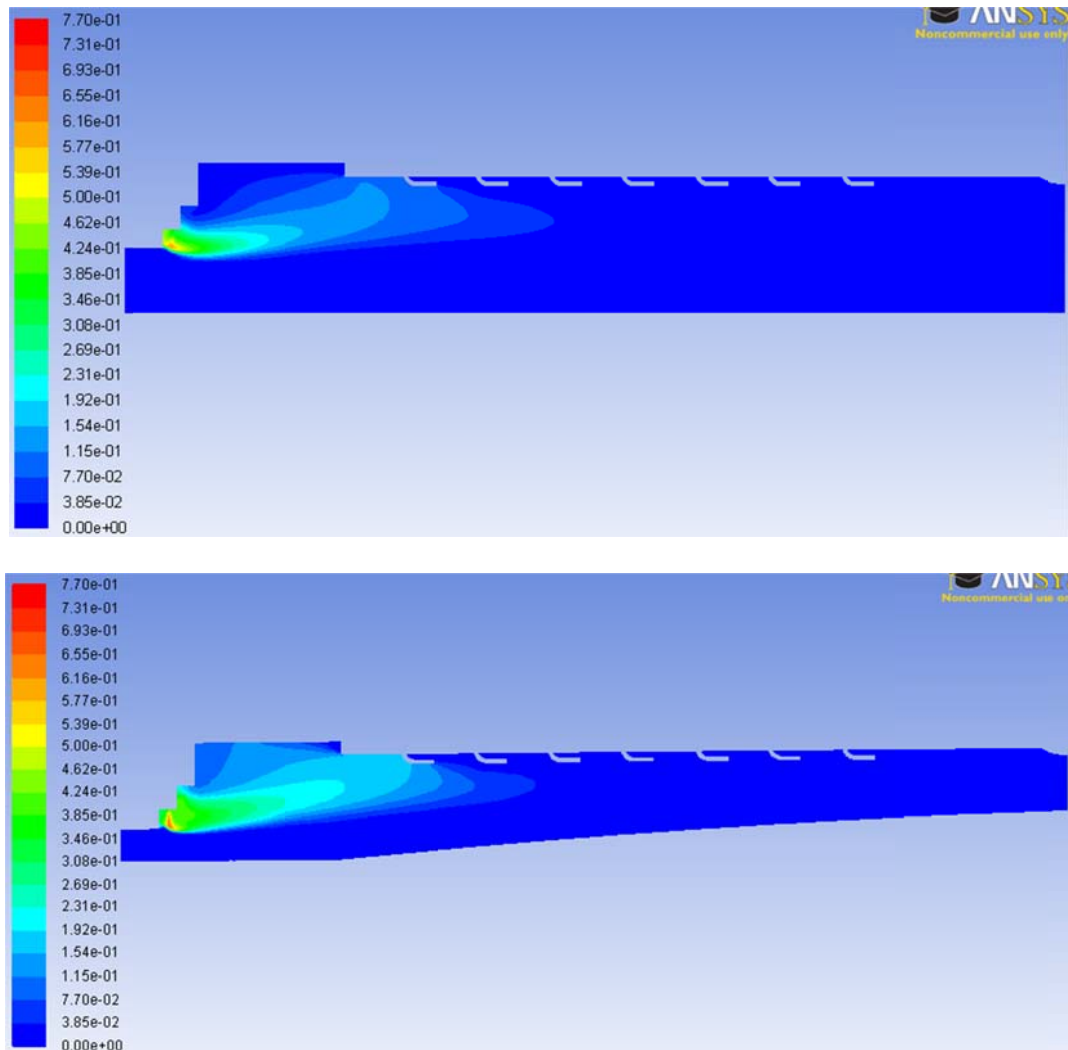


Figure 30: Contours of  $C_{12}H_{23}$  mass fraction. The top picture shows the can type combustor and the bottom figure is the annular type combustor.

The temperature contours for both the can type combustor and the annular type combustor are shown below in Figure 31. Due higher velocity of the secondary inlet jets in the can combustor, the top portion of the primary region has a leaner mixture than that of the annular combustor. Since both regions are above an equivalence ratio of 1, the lower equivalence ratio region has a higher temperature. This explains why the temperature of the primary region of the can combustor is at a higher temperature than the annular combustor. Since the primary region is rich, the temperatures there are lower which produces lower  $\text{NO}_x$  levels as compared to the case where combustion takes place closer to stoichiometry. However, for inlet flow conditions chosen for the primary inlet, secondary inlet, and cooling holes, no quick-quenching takes place. Combustion takes place in the dilution region which produces high temperatures. This is in stark contrast to conventional RQL combustors which have a lean, homogenous dilution zone.



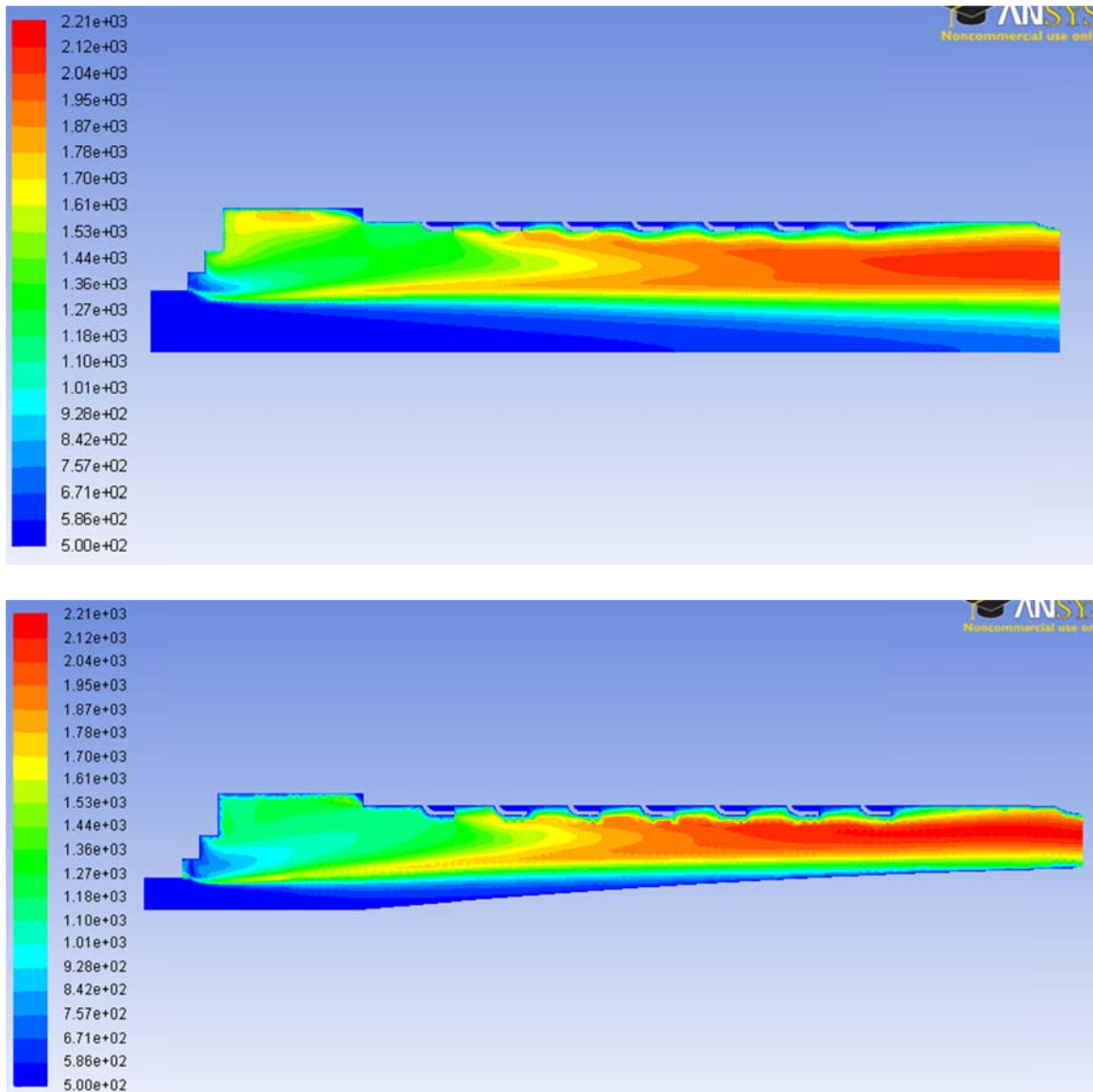


Figure 31: Contours of temperature (K). The top picture shows the can type combustor and the bottom figure is the annular type combustor.

The exit plane temperature profile of a combustor should be cooler towards the periphery of the combustor to preserve the life of the turbine blades. The annular combustor's exit temperature profile displays this behavior. The can type combustor, however, does not display this behavior. This is more clearly shown below. The temperature is much higher towards the top and bottom of the combustor as compared to the center of the combustor, which is the opposite of what is required to preserve the life

of the turbine blades. The temperature distribution is quite poor and some design modifications need to be made for the can type combustor if this combustor is to be used with a turbine.

The maximum temperatures of the can combustor and the annular combustor are 2120 K and 2205 K, respectively. From the literature, the adiabatic temperature of kerosene is between 2300-2500 K, which is above the maximum temperature calculated here. This provides a certain level of confidence in the results (although experimentation is still required for true validation).

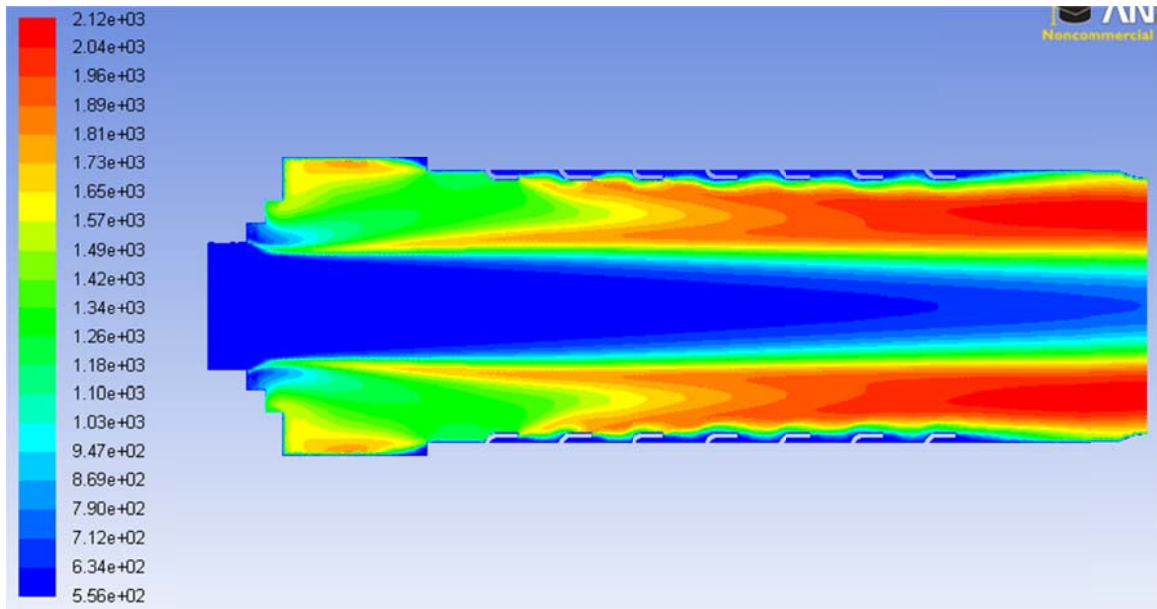


Figure 32: Temperature contours (K) of the full can type combustor. The temperature contours are mirrored about the centerline to show the full can combustor.

Figure 33 shows the fuel droplet trajectories for both combustors. It can be seen that the droplets evaporate very quickly and do not leave the step area. This is due to the high temperatures in the primary region. The droplets in the annular type combustor take longer to evaporate than the droplets in the can type combustor because the fuel vapor mass fraction is higher in the annular type combustor. A fuel droplet evaporates slower



when the gas surrounding the droplet has a higher concentration of fuel vapor. The situation depicted in Figure 33 is what is expected to happen when fuel atomization is satisfactory.

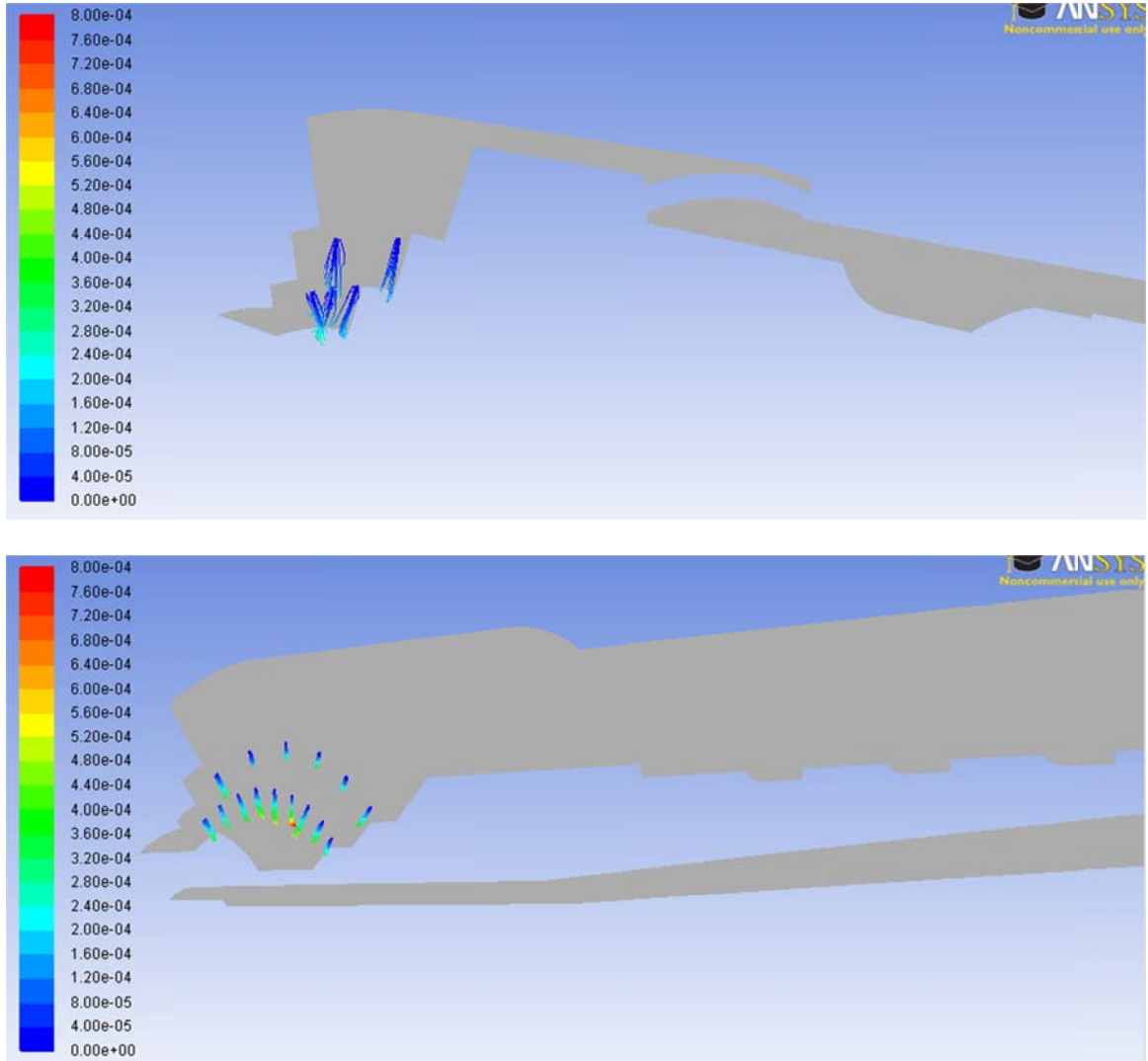


Figure 33: Fuel droplet residence time (s). The top picture shows the can type combustor and the bottom figure is the annular combustor

Figure 34 shows the corresponding contours of  $O_2$  mass fraction. It can be seen that the primary zone has very little  $O_2$  which leads to low  $NO_x$  production.

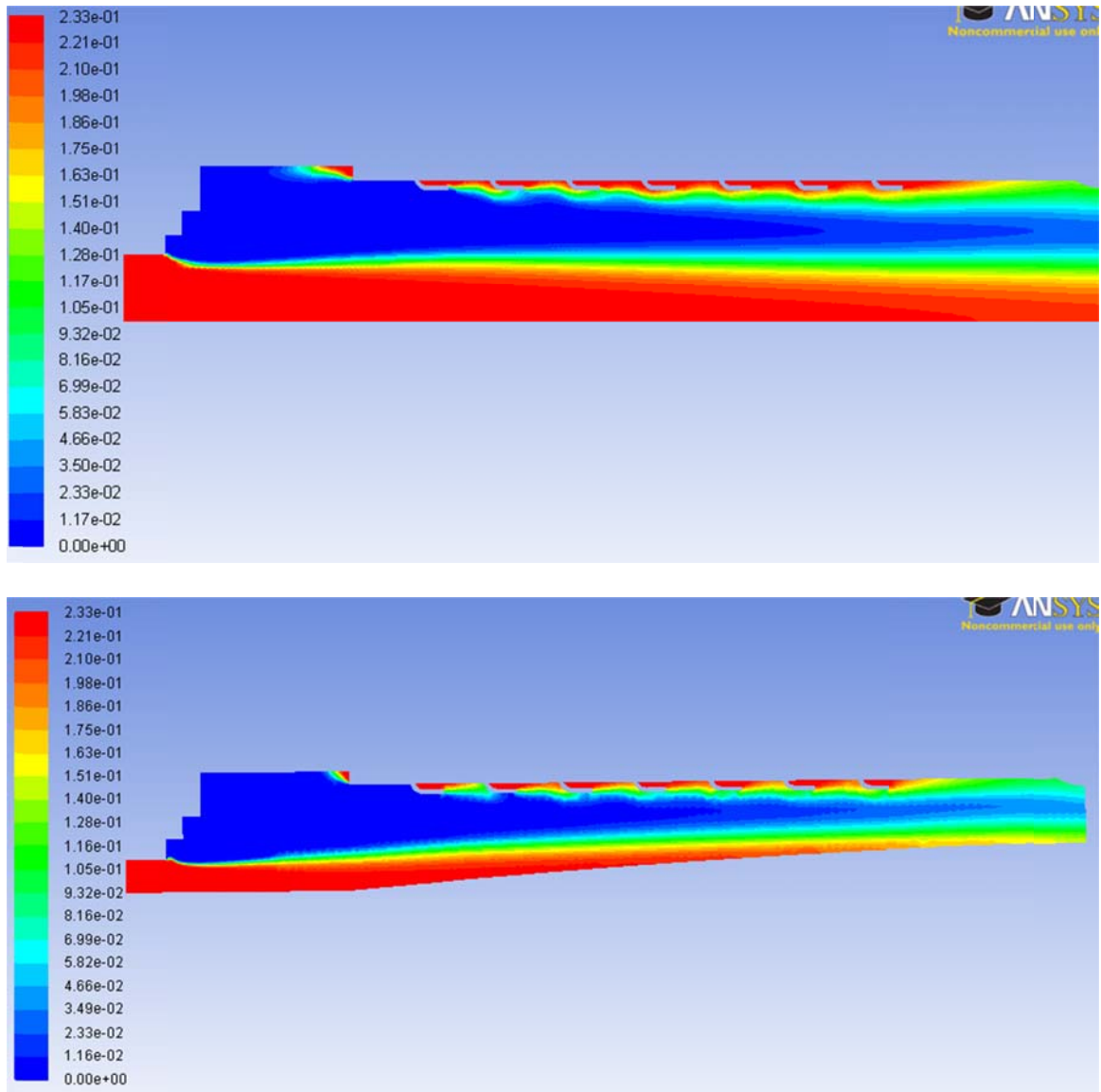


Figure 34: Contours of O<sub>2</sub> mass fraction. The top picture shows the can type combustor and the bottom figure is the annular type combustor.

Figure 35 shows the CO mass fractions. Since there is not enough oxygen to complete combustion in the primary zone, large levels of CO form there. There still remains some CO, however, in the dilution zone.

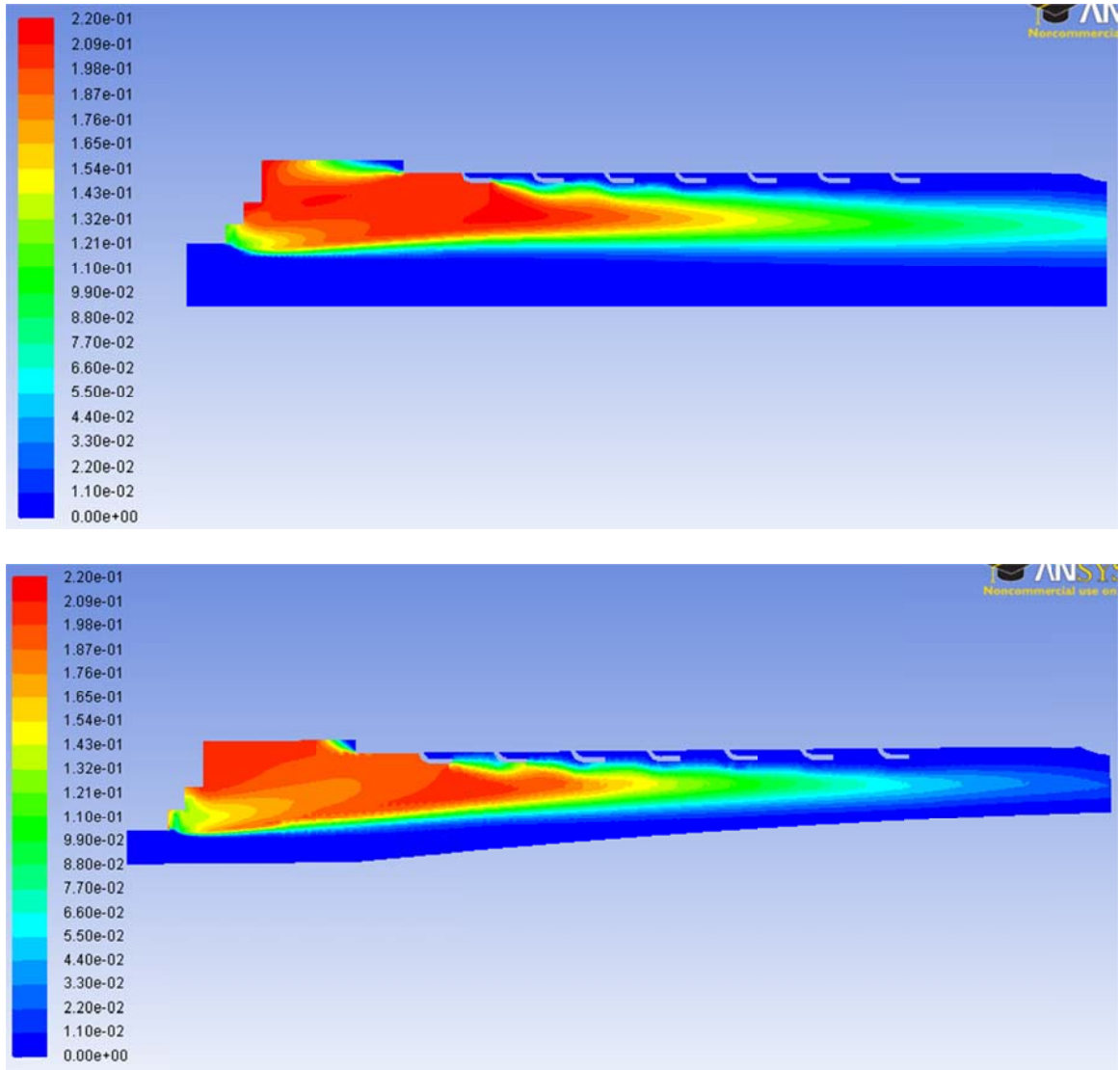


Figure 35: Contours of CO. The top picture shows the can type combustor and the bottom figure is the annular type combustor.

Figure 36 shows the contours of dry  $\text{NO}_x$  in ppm.  $\text{NO}_x$  levels are moderate in the top region of the steps because stoichiometric conditions exist there due to the secondary air stream.  $\text{NO}_x$  levels also start to rise when oxygen concentrations and temperature rise towards the exit of the combustor. Maximum  $\text{NO}_x$  concentration for the can type combustor occurs there.

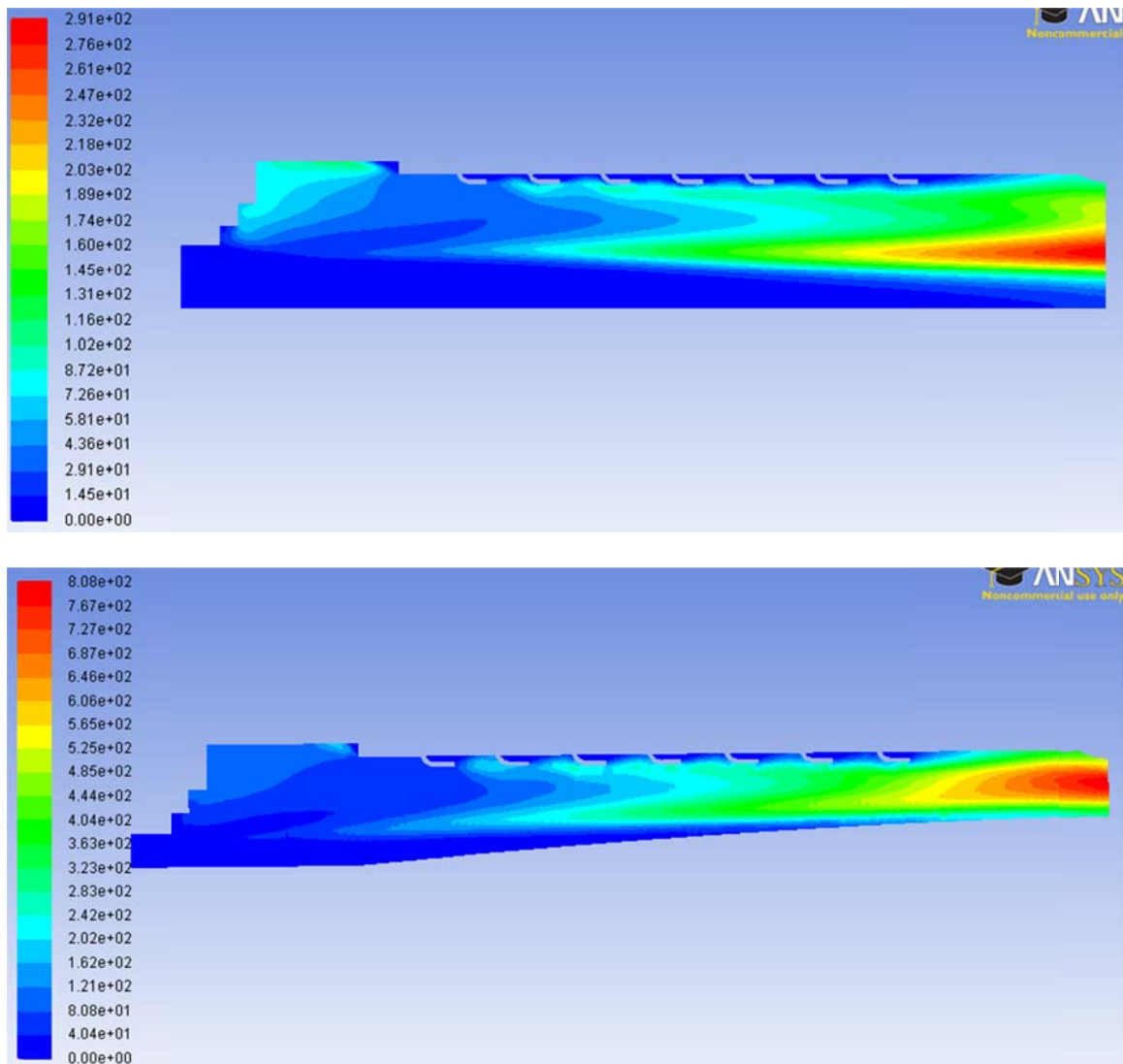


Figure 36: Contours of dry NO<sub>x</sub> (ppm). Note: the contour levels are different for each picture. The top picture shows the can type combustor and the bottom figure is the annular type combustor.

The maximum concentration of NO<sub>x</sub> occurs where the temperatures are highest and the mixture is leanest. This can better be seen for the can type combustor in Figure 37 where the contours of NO<sub>x</sub> are plotted with an iso-surface of equivalence ratio equal to unity.

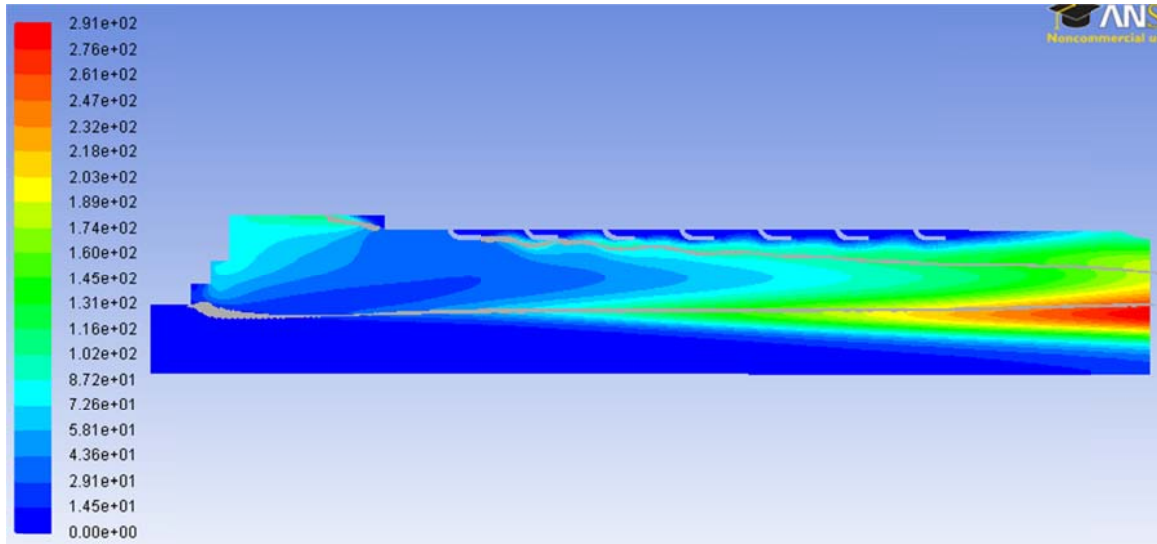


Figure 37: Contours of dry  $\text{NO}_x$  concentrations (ppm) with an iso-surface of equivalence ratio equal to unity

The surface of unity equivalence ratio intersects the area of maximum  $\text{NO}_x$  concentration. Below this surface, lean conditions exist which explains why the majority of region of maximum  $\text{NO}_x$  occurs below the iso-surface. For the annular type combustor, the fuel-air mixture is entirely lean approximately midway between the last cooling vane and the exit of the combustor. Temperatures are also the highest in that region which is why the  $\text{NO}_x$  levels are at maximum level there.

Contours of  $\text{CO}_2$  and  $\text{H}_2\text{O}$  are shown in Figures 38 and 39. Notice that the  $\text{CO}_2$  concentration is low in the primary zone because of the incomplete combustion resulting from local rich equivalence ratios.

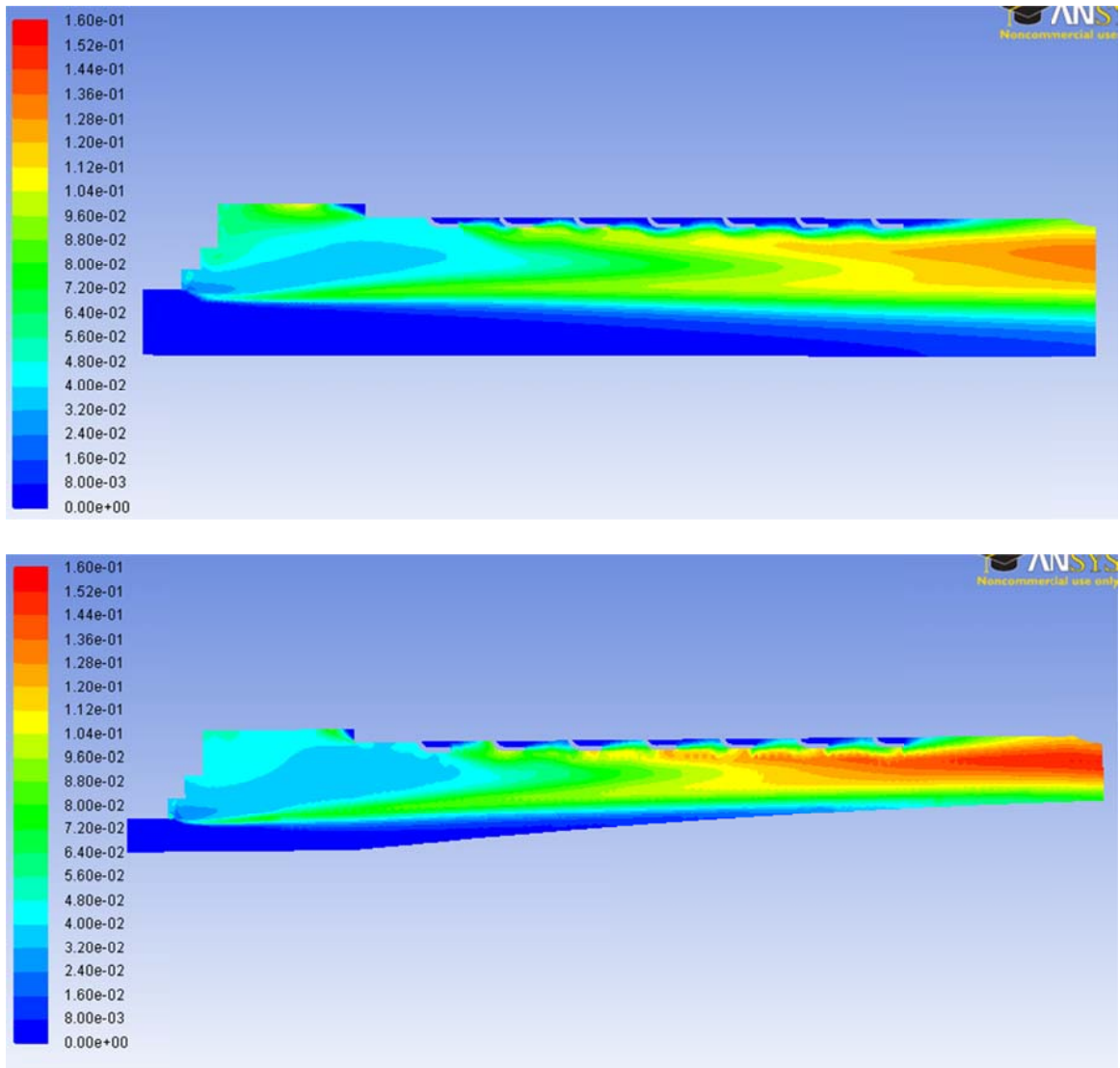


Figure 38: Contours of CO<sub>2</sub> mass fraction. The top picture shows the can type combustor and the bottom figure is the annular type combustor.

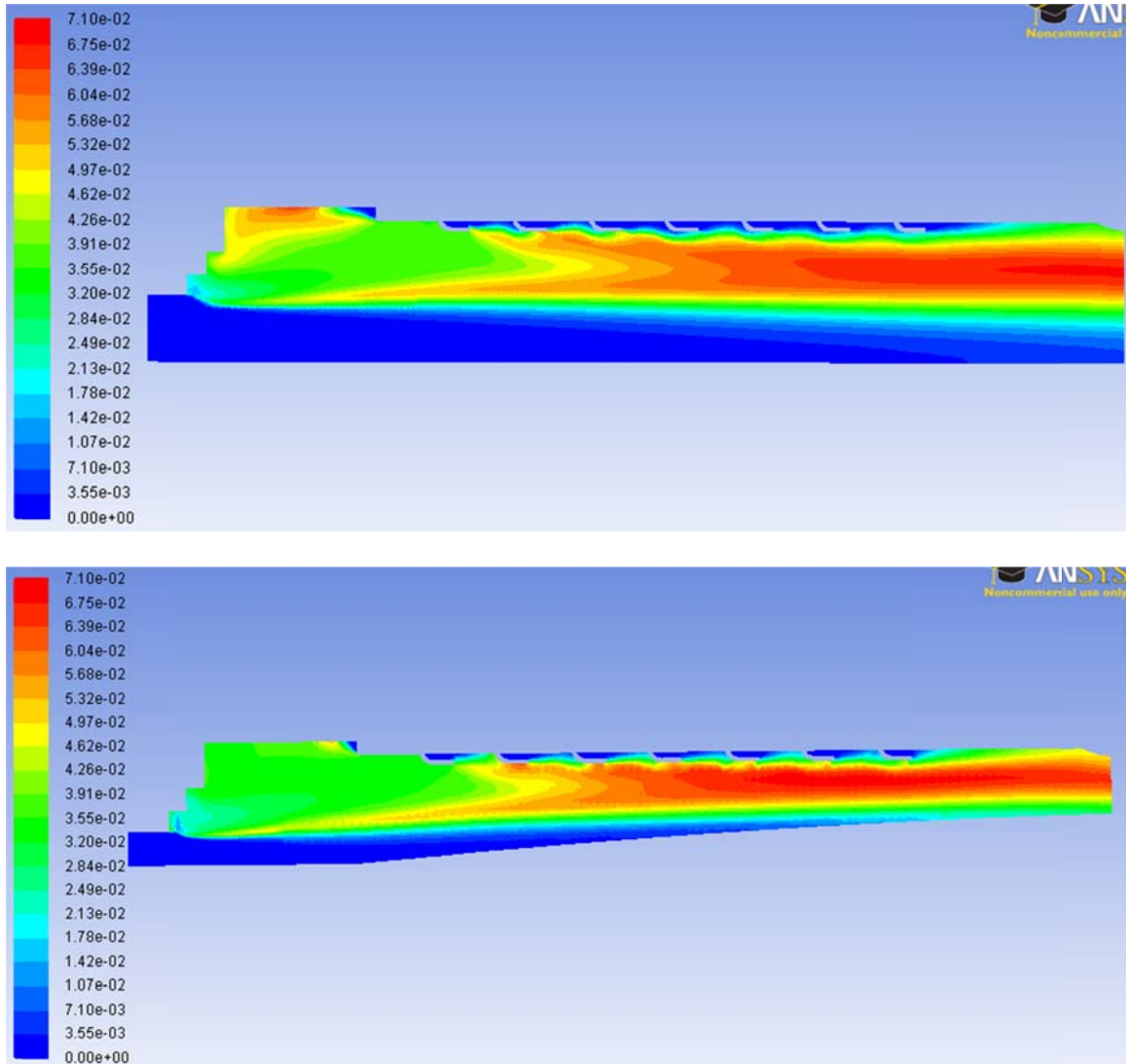


Figure 39: Contours of H<sub>2</sub>O mass fraction. The top picture shows the can type combustor and the bottom figure is the annular type combustor.

Table 4 summarizes some of the resulting performance levels for both combustors:

	Can	Annular
Combustor Pressure Drop	3.28%	3.09%
Combustion Efficiency	98.70%	99.97%
NO <sub>x</sub> (ppm)	178	699
NO <sub>x</sub> Emission Index	3.6	12
CO (ppm)	29774	11235
CO Emission Index	559	205
Residence Time (ms)	7.24	25.8

Table 4: Comparison between annular type combustor and can type combustor for an operating pressure of 300 psi (20.7 bar) and a global equivalence ratio of 0.7

The annular combustor has a higher NO<sub>x</sub> emission index than the can type combustor, but its CO emission index is lower. This can be attributed to the residence time of both combustors. CO emissions increase with a decrease in residence time which is why the can type combustor has worse CO emissions than the annular type. NO<sub>x</sub> levels increase linearly with residence time for many combustors. Looking at Table 4, the residence time of the annular combustor is 3.6 times that of the annular combustor. Assuming the sudden expansion combustor follows the same linear trend, the NO<sub>x</sub> emission index in the annular type combustor is:

$$3.6 * 3.6 \text{ g NO/kg fuel} = 12.96 \text{ g NO/kg fuel}$$

which is approximately the same result calculated for the annular type combustor.

The calculated values for pressure drop are below that quoted in the literature for a typical combustor. Also, the annular combustor pressure drop is lower than the can combustor pressure drop, which is consistent with the literature, although the difference is minute.

The RQL combustor studied by Bank had the highest NO<sub>x</sub> emission index of 7g NO/kg fuel and the highest CO emission index of 66 g CO/kg fuel. The can type combustor has a NO<sub>x</sub> emission index lower than this value, but the CO emission index is far too high. The annular type combustor's CO emission index is too high as well, although it is better than the CO emission index of the can type combustor.

#### *4.2 Comparison of Results for Various Models*

This section compares different turbulence, combustion, and radiation models that are frequently used in the literature to model combustion problems. The results using the eddy dissipation model are compared to the PPDF model. Then a case utilizing the RSM



model is compared to the results using the  $k-\epsilon$  model. Finally the results for all the models are summarized and compared at the end of the section. All cases are computed with an operating pressure of 300 psi (20.7 bar) and a global equivalence ratio of 0.7. The models are compared only for the can type combustor.

Figure 40 shows temperature contours resulting from using the eddy dissipation model. The temperatures obtained from the eddy dissipation model are much lower than the predicted values from the PPDF model. The PPDF model therefore represents a more conservative estimate of the flow field because it predicts higher temperatures.

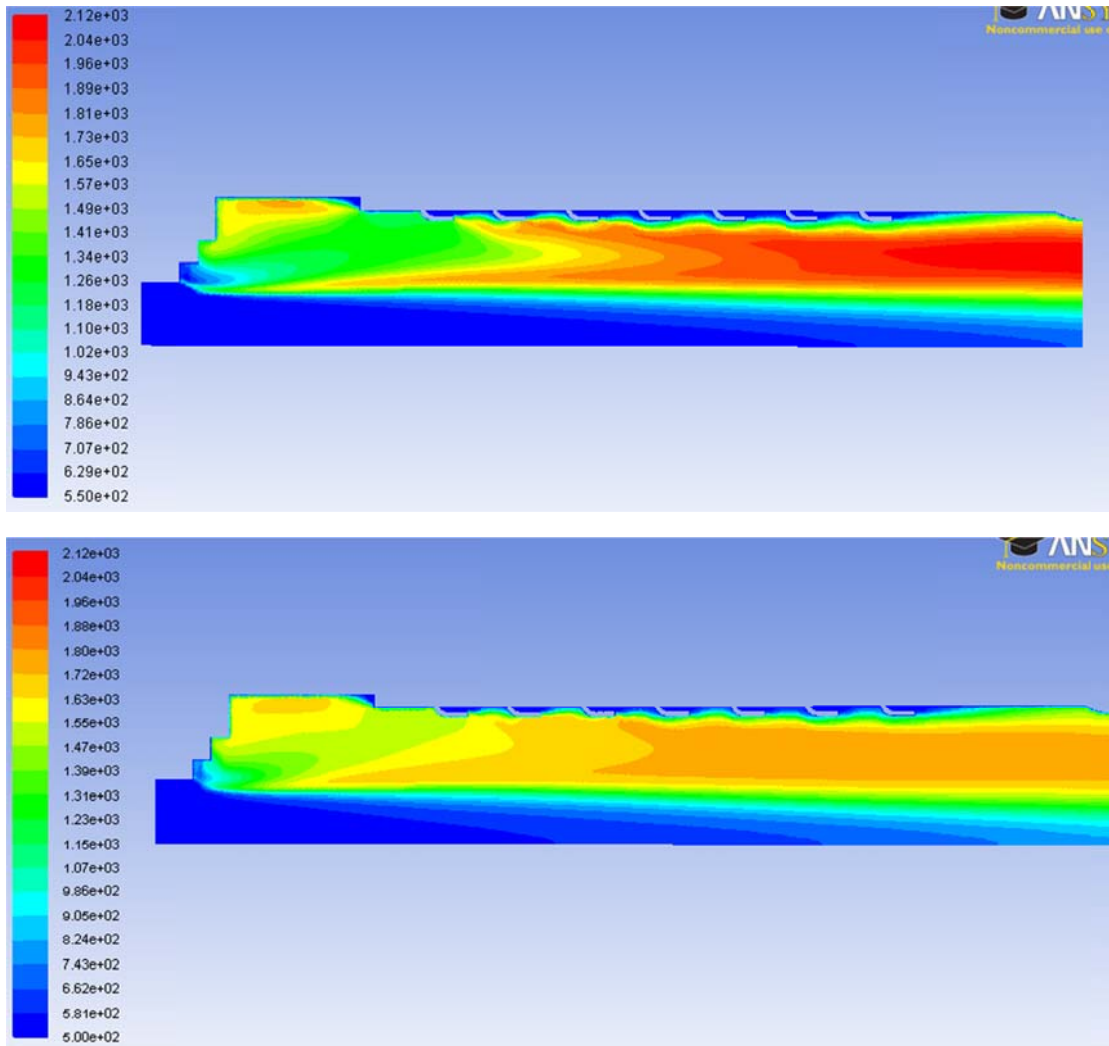


Figure 40: Contours of temperature (K) for the eddy dissipation model. The top picture shows the results obtained from the PPDF model, the bottom picture shows the results obtained from the eddy dissipation model.

The contours of  $\text{NO}_x$  concentrations are shown in Figure 41. Since the temperatures are much lower than in the PPDF model, the  $\text{NO}_x$  levels are also much lower with the eddy dissipation model. The region of maximum  $\text{NO}_x$  concentration is wider for the eddy dissipation case because the region of maximum temperature is wider for the eddy dissipation case.

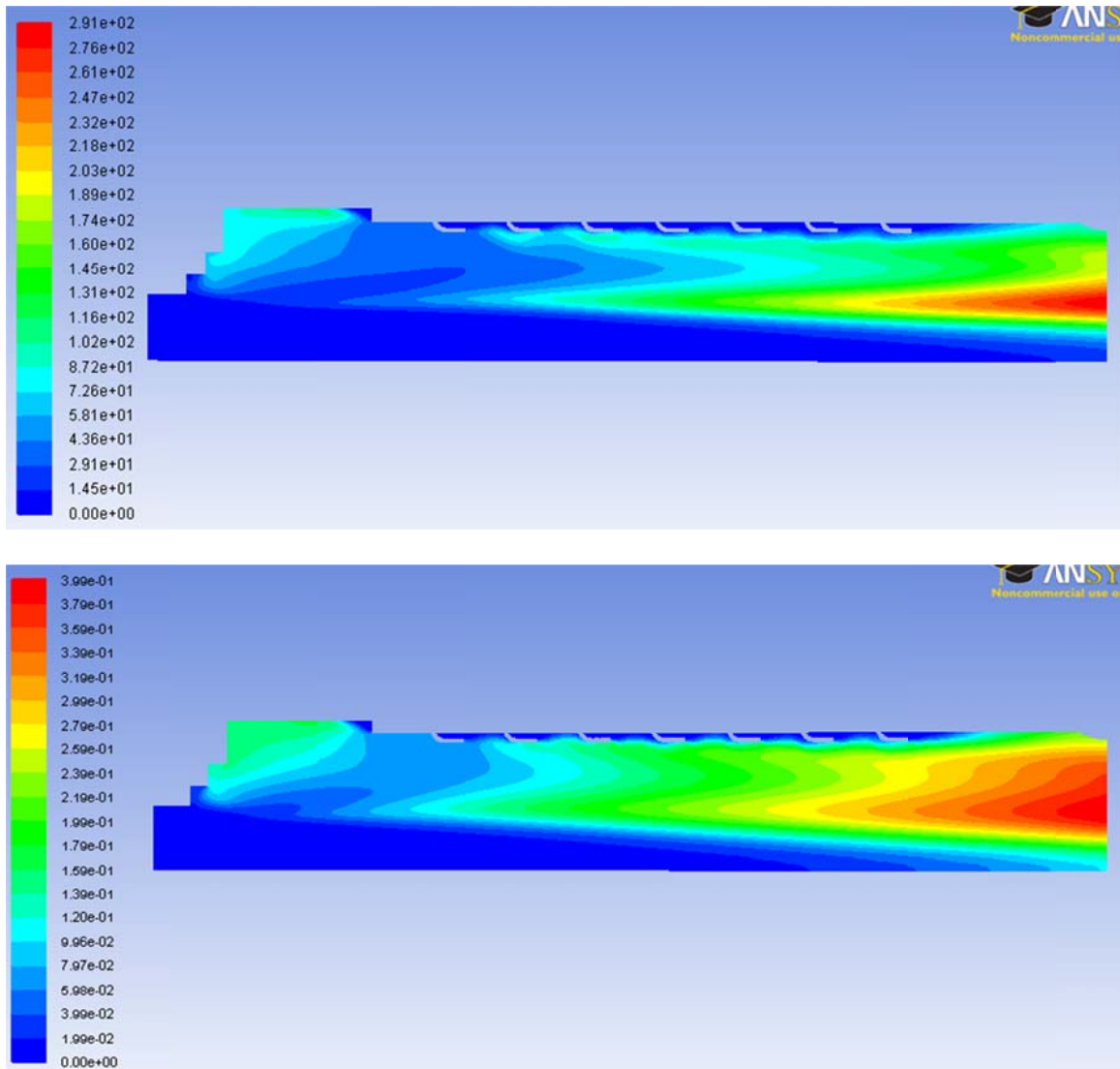


Figure 41: Contours of  $\text{NO}_x$  concentration (ppm). The top picture shows the results obtained from the PPDF model, the bottom picture shows the results obtained from the eddy dissipation model.

The realizable  $k$ - $\epsilon$  model produces similar results to the standard  $k$ - $\epsilon$  models, so no contours are shown. The discrete ordinates model results are very similar to the P-1 radiation model, so no contours are shown for that model as well. Only the emissions levels and combustion efficiency are reported.

The temperature contours with the Reynolds stress model are shown below in Figure 42. The RSM model calculations predict a mixture in the primary zone that is

closer to stoichiometry as compared to the standard k- $\epsilon$  case. Close to the upper left corner of the primary zone, the local equivalence ratio computed by the RSM model is between 1.7-2.0, while the equivalence ratio predicted by the k- $\epsilon$  is between 2.0-2.3.

The leaner mixture produces higher temperatures in the primary zone.

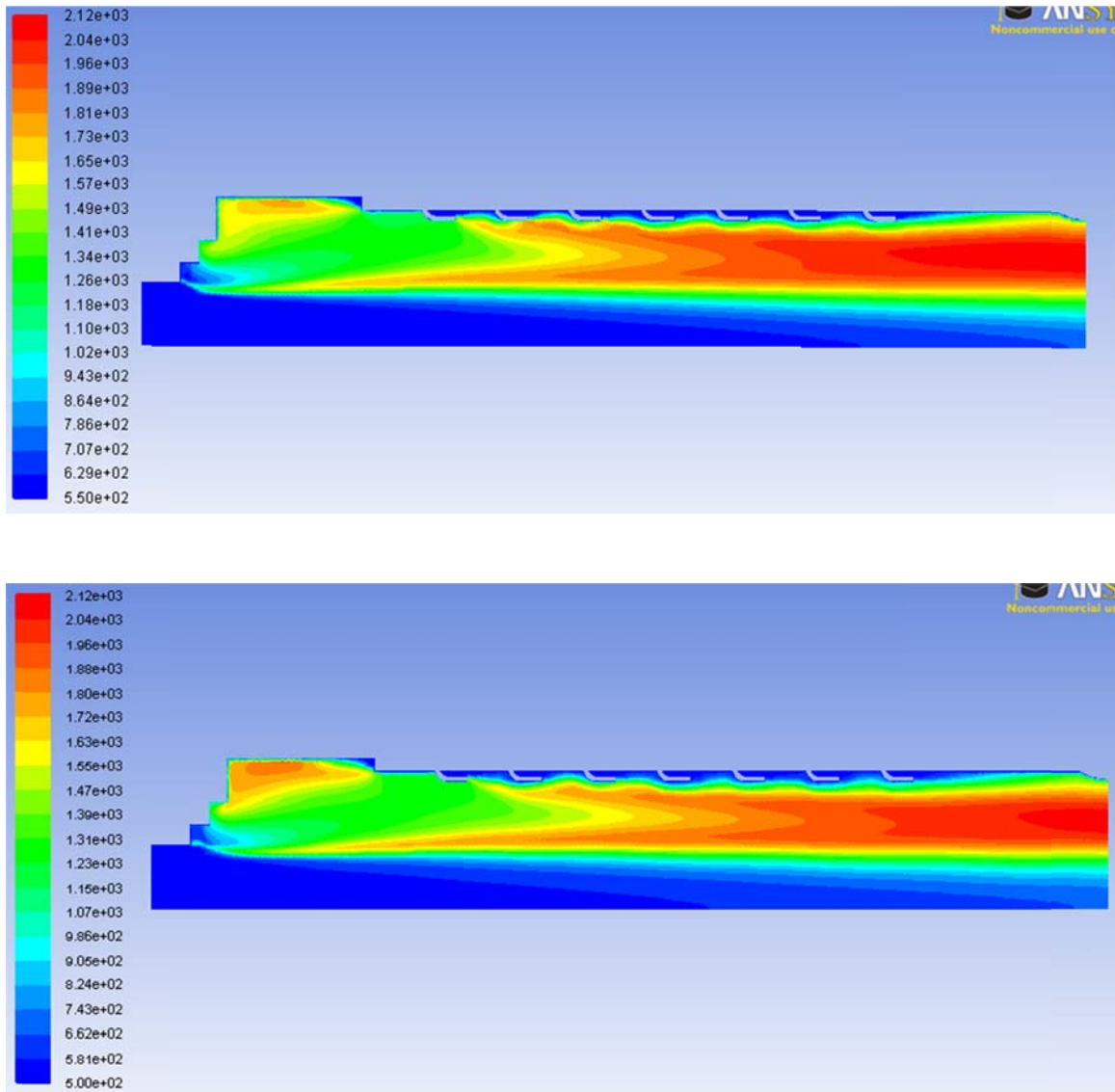


Figure 42: Temperature contours (K). The top picture shows the results obtained from the PPDF model, the bottom picture shows the results obtained from the RSM model.

The  $\text{NO}_x$  concentrations of the RSM model are shown below. The RSM model produces more  $\text{NO}_x$  in the primary zone due to the higher temperatures in the primary zone, and this attributes to its higher overall  $\text{NO}_x$  levels in the exit plane.

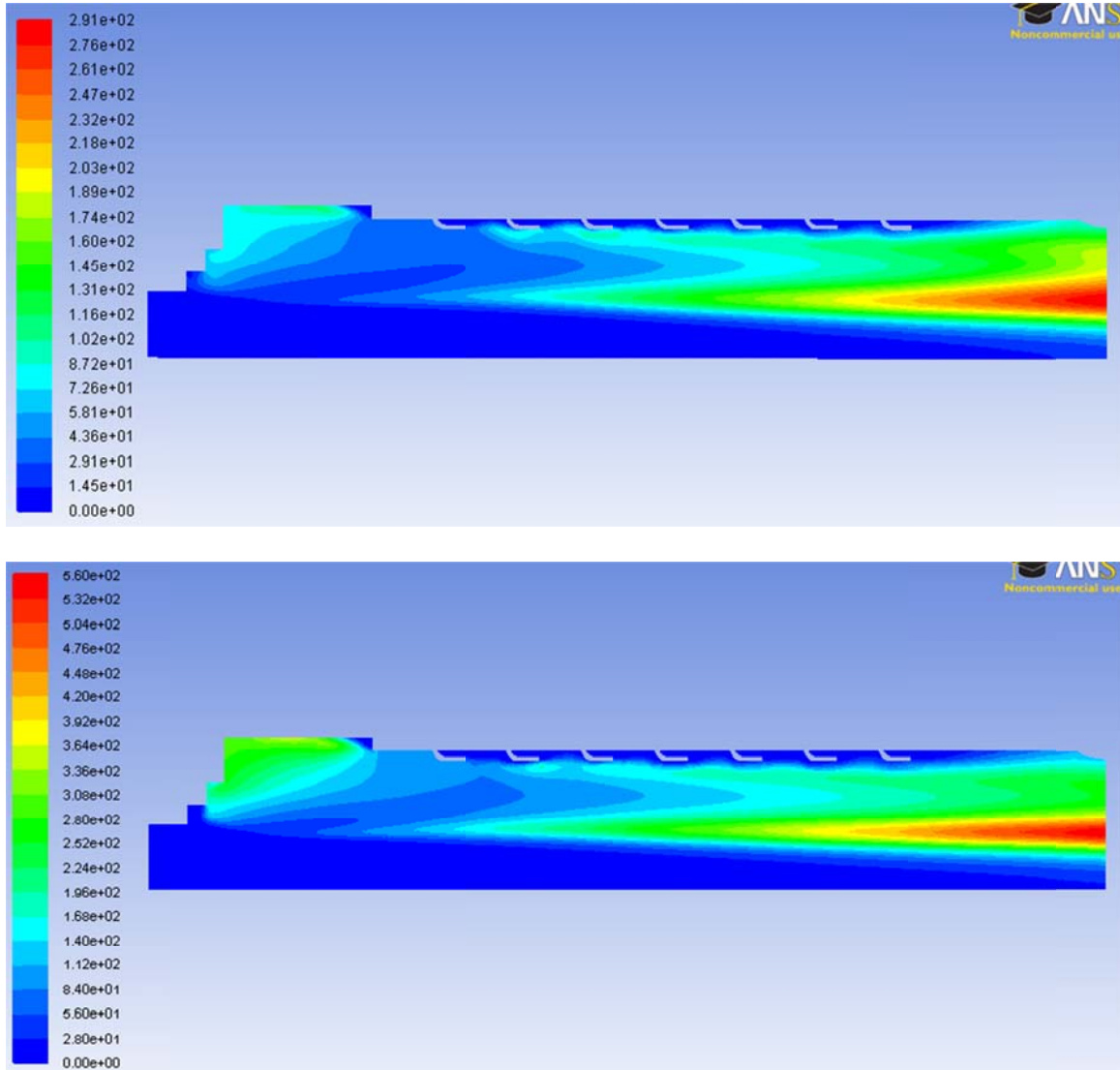


Figure 43: Contours of  $\text{NO}_x$  concentration (ppm). The top picture shows the results obtained from the PPDF model, the bottom picture shows the results obtained from the RSM model.

A summary of all the models tested are presented in Table 5. The standard and realizable  $k-\epsilon$  models, RSM model, and DO all produced similar flow fields with minor differences. The eddy dissipation model produced a different temperature field which

predicted much lower temperatures than the other models, and it predicts a wider area of maximum temperature. The RSM predicts noticeably higher emissions and lower combustion efficiency than the other models due to its different prediction of mixing in the primary zone. Note how a difference in equivalence ratio of about 0.3 constitutes an increase of about 100 ppm of NO<sub>x</sub> in the exit plane. The k-  $\epsilon$  models and the DO model produced all produced similar emission levels and combustion efficiency.

300 psi, 0.7 ER	Standard k- $\epsilon$ PPDF P-1	Realizable k- $\epsilon$ PPDF P-1	RSM PPDF P-1	Standard k- $\epsilon$ PPDF DO	Standard k- $\epsilon$ EDM
Combustion Efficiency	98.70%	98.90%	97.70%	98.90%	99.30%
NO <sub>x</sub> (ppm)	178	118	280	180	0.3
NO <sub>x</sub> Emission Index	3.6	2.39	5.73	3.6	0.006
CO (ppm)	29774	28527	34882	28128	N/A
CO Emission Index	559	535	663	529	N/A

Table 5: Summary of results from various models

#### *4.3 Results of the Parametric Study*

The variation in NO<sub>x</sub> concentrations and emission index in the exit plane for the can type combustor for varying operating pressure and global equivalence ratio are shown in Figures 44 and 45:

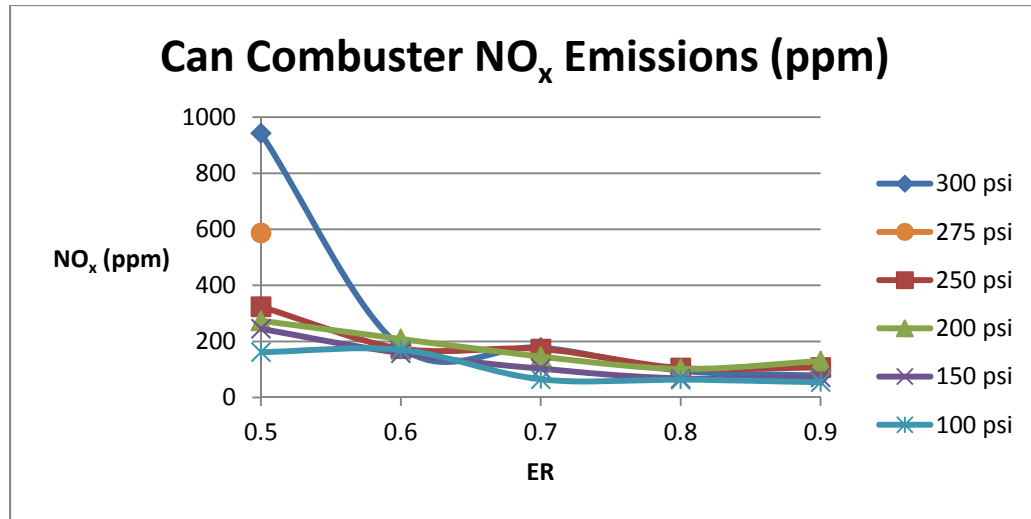


Figure 44: NO<sub>x</sub> exit concentration variation with operating pressure and equivalence ratio for the can type combustor.

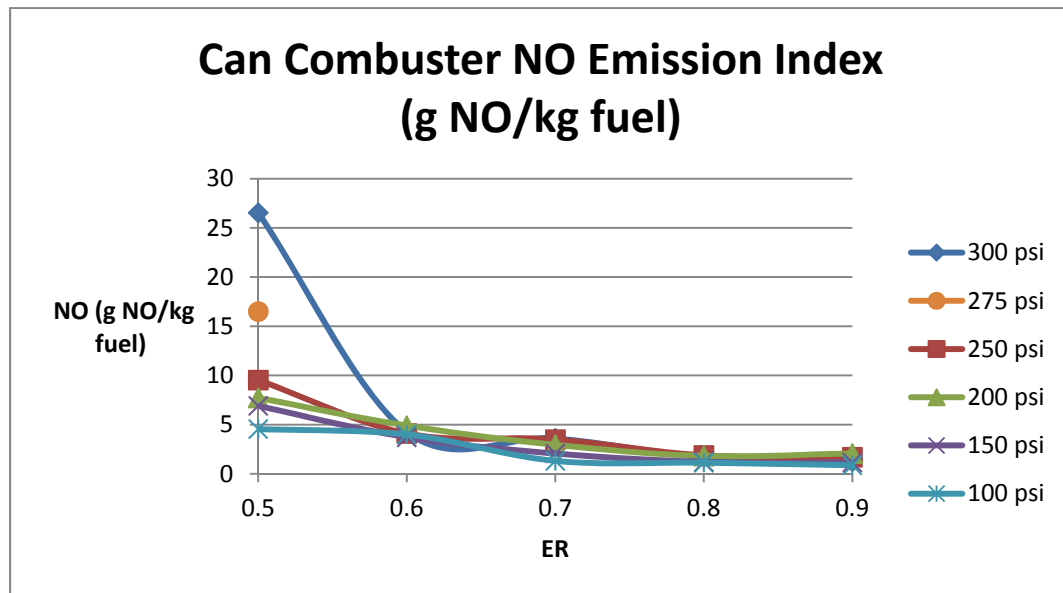


Figure 45: Variation of NO emission index with operating pressure and equivalence ratio for the can type combustor.

The NO<sub>x</sub> levels decrease very slightly with increasing equivalence ratio as expected, since there is less oxygen available to dissociate. Pressure seems to have no effect on the NO<sub>x</sub> levels for the can combustor above an equivalence ratio of 0.6. However, at an equivalence ratio of 0.5, the NO<sub>x</sub> concentrations in the exit plane increase with pressure.

At an equivalence ratio of 0.5 and an operating pressure of 100 psi (6.9 bar), the primary zone equivalence ratio is close to unity, more so than the other cases with higher equivalence ratios. When the operating pressure is increased with a fixed equivalence ratio of 0.5, the primary zone equivalence ratio reduces to unity, and thus higher temperatures are encountered in the primary zone. These higher temperatures produce higher  $\text{NO}_x$  concentrations in the primary zone. An additional case is run with an operating pressure of 275 psi (19 bar) to see how the pressure varied between the case of 250 psi (17.2 bar) and 300 psi (20.7 bar). This is represented by the orange dot in Figures 44 and 45.

Similar  $\text{NO}_x$  data for the annular type combustor are shown in Figure 46 and 47

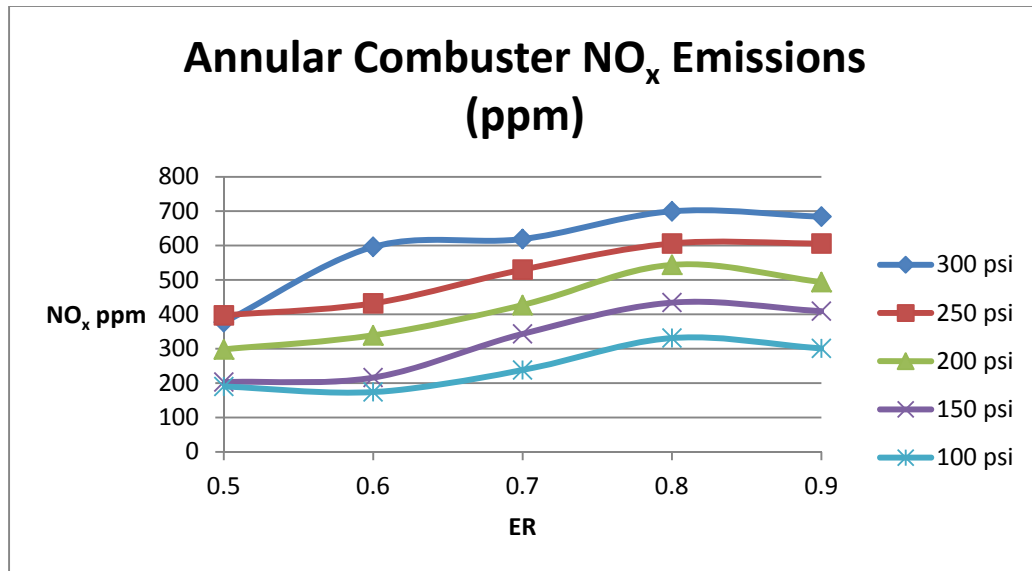


Figure 46:  $\text{NO}_x$  exit concentration variation with equivalence ratio and operating pressure for the annular type combustor



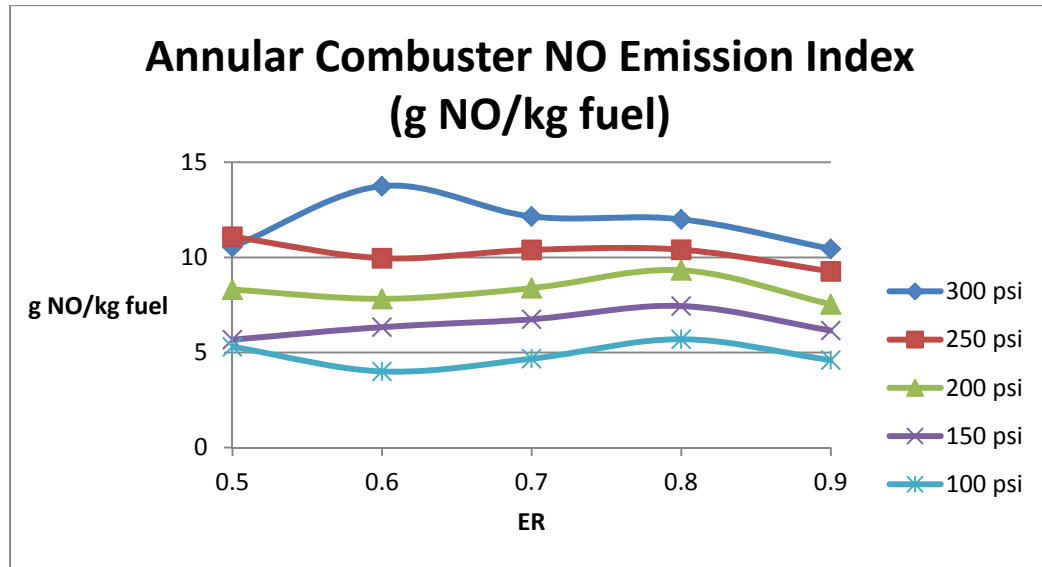


Figure 47: Variation of NO emission index with operating pressure and equivalence ratio for the annular type combustor

The curves in Figures 46 and 47 display little change in  $\text{NO}_x$  concentration with equivalence ratio for a given operating pressure. Furthermore, there is a more pronounced effect of operating pressure on  $\text{NO}_x$  concentration as compared to the can type combustor. The reason is as follows: a lean mixture is able to develop in the annular type combustor due to its longer length. Fuel-lean mixtures are more sensitive towards pressure variations with regards to  $\text{NO}_x$  production, so the annular combustor's  $\text{NO}_x$  production is effected by pressure. The can type combustor, due to its smaller length and poor mixing characteristics, cannot develop a completely lean mixture unless the global equivalence ratio is sufficiently low (i.e. less than or equal to 0.5). Since fuel-rich mixtures are not sensitive to operating pressure, the can type combustor displays little sensitivity to operating pressure beyond an equivalence ratio of 0.5.

The leanest primary zone equivalence ratio for the annular type combustor is between 3 and 3.7. Because the primary zone stays far away from stoichiometric conditions, the annular type combustor  $\text{NO}_x$  concentrations do not vary with pressure in

the same way as the can type combustor. When the equivalence ratio is less than about 1.3 in the primary region the  $\text{NO}_x$  concentrations grow rapidly with leaner mixtures.

The CO emissions in ppm and in g CO/g fuel for the can type combustor are shown in Figures 48 and 49.

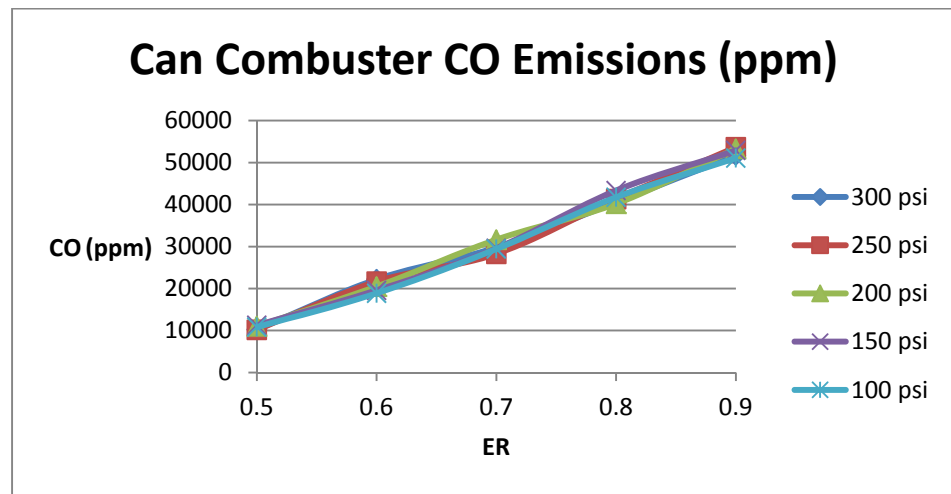


Figure 48: CO exit concentration variation with equivalence ratio and operating pressure for the can type combustor

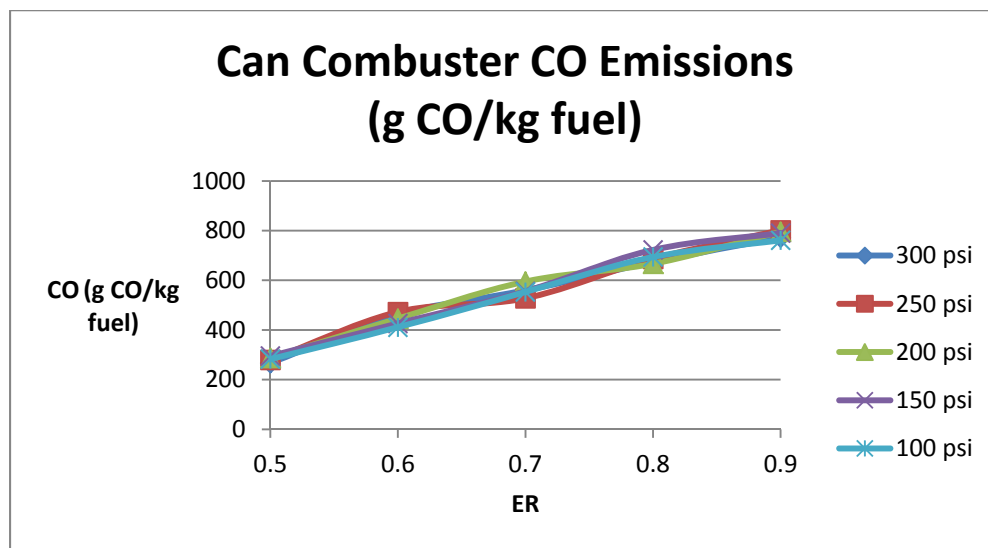


Figure 49: Variation in CO emission index concentration with operating pressure and equivalence ratio for the can type combustor

CO emissions increase with equivalence ratio because of incomplete combustion. Operating pressure shows no noticeable effect on the CO emissions. Normally, higher pressures suppress the dissociation of  $\text{CO}_2$  into CO, which lowers CO emissions. However, since the regions of appreciable concentrations of  $\text{CO}_2$  are small due to the large regions of incomplete combustion, the amount of CO formed from  $\text{CO}_2$  is small. Any increase in pressure decreases the CO dissociated in this small region, but its effect is negligible due to the large amounts of CO formed due to incomplete combustion.

The CO emissions for the annular type combustor are shown in Figures 50 and 51.

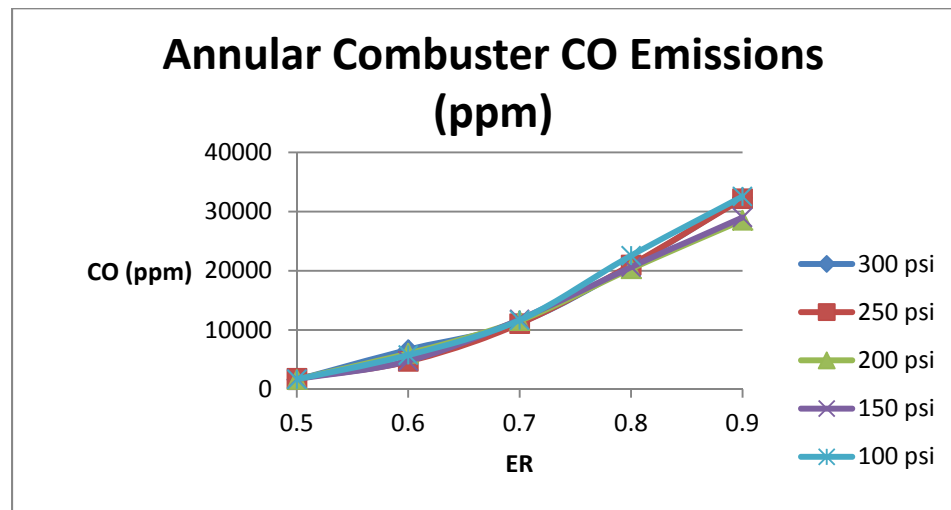


Figure 50: Variation in CO exit plane concentration with operating pressure and equivalence ratio

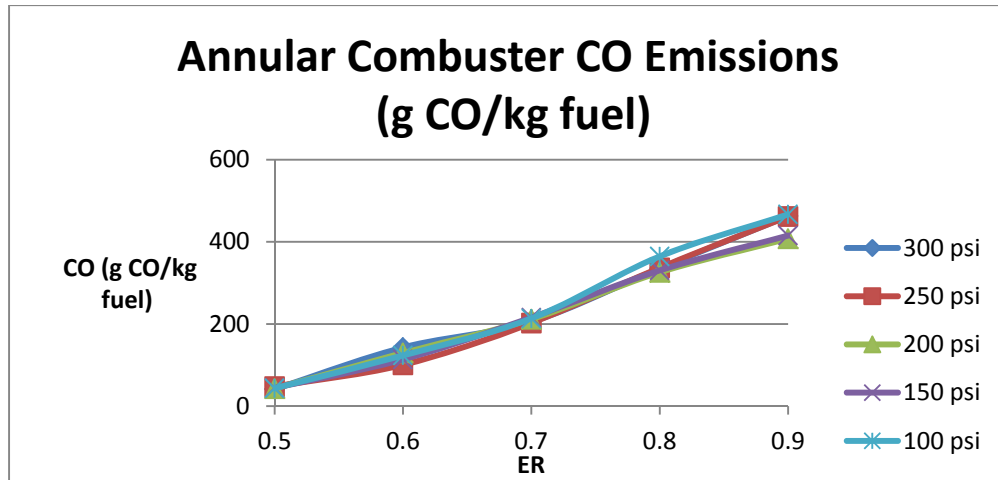


Figure 51: Variation in CO emission index concentration with operating pressure and equivalence ratio

The variation of CO concentration with operating conditions for the annular combustor is identical to that of the can combustor.

To summarize the literature on representative NO Emission indexes, LPP and LDI combustors achieve between 2 g NO/ kg fuel to 6 g NO/ kg fuel. RQL combustors NO emission index's ranged from 9 g NO/ kg to 16 g NO/ kg. Typical NO emission levels representing take-off conditions range from 25 g NO/ kg to 30 g NO/ kg [40]. The annular type combustor achieves between 5 g NO/ kg fuel and 14 g NO/ kg fuel through its operating range. The can type combustor shows NO<sub>x</sub> emissions below 5 g NO/ kg fuel for the majority of its operating range, which is comparable to the performance of the LPP combustor. The annular combustor performs slightly better than the other RQL combustors quoted in the literature, but does not perform as well as the lean type combustors, keeping in mind that the operating conditions are not identical.

Typical CO emission levels range from 60-100 g CO/ kg fuel for RQL combustors. For an equivalence ratio between 0.5 and 0.6, the CO emission index is about 47 g CO/ kg fuel and 142 g CO/ kg fuel respectively. Anywhere beyond an

equivalence ratio of 0.6, the CO emission index becomes way beyond the value of typical combustors for the annular type combustor. Throughout the operating conditions for the can type combustor, the CO emissions are unacceptable, with the lowest value being slightly above 200 g CO/ kg fuel.

The combustion efficiency for both combustors are shown in Figures 52 and 53:

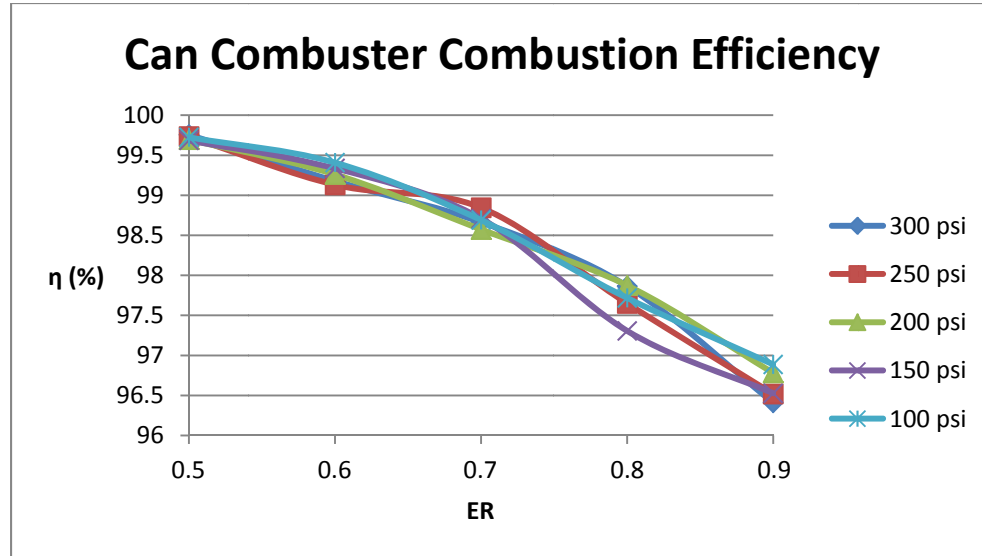


Figure 52: Can combustor combustion efficiency variation with operating conditions

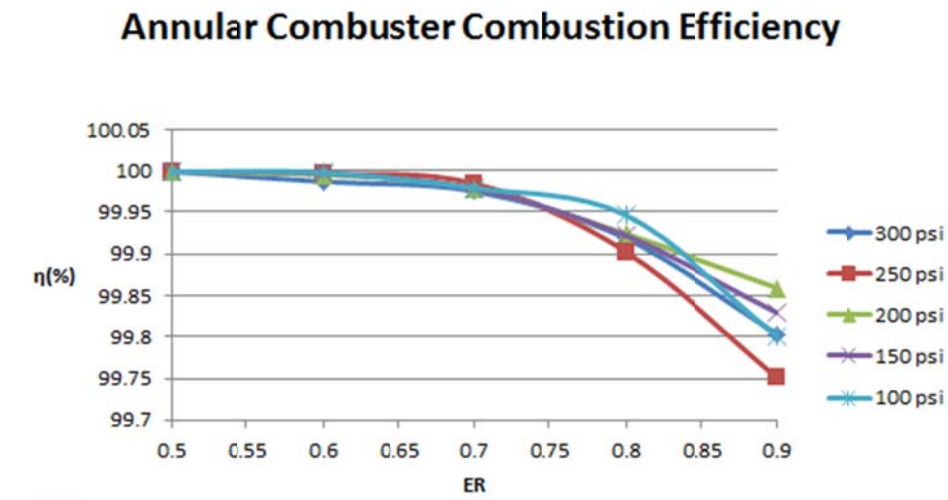


Figure 53: Annular combustor combustion efficiency variation with operating conditions

The can type combustor's efficiency is satisfactory for a global equivalence ratio of 0.6 and drops off to unacceptable values after that. The annular type combustor displays acceptable combustion efficiency throughout its operating range.

## 5. CONCLUSIONS AND RECCOMENDATIONS

A sudden expansion combustor was analyzed using CFD to see how the operating characteristics effect the  $\text{NO}_x$  and CO emissions. A can type combustor and an annular type combustor were tested over a range of operating conditions to see how they affected emission levels. It was found that the can type combustor was able to achieve low  $\text{NO}_x$  emissions compared to lean type combustors due to its low residence time and rich primary zone. However, the exit temperature distribution, CO emission levels, and combustion efficiency were unacceptable. The high CO emission levels for both combustor types are due to poor mixing in the primary region. The annular type combustor showed higher  $\text{NO}_x$  emissions, higher combustion efficiency, and lower CO emissions than the can type combustor due to its longer residence time. The annular combustor's  $\text{NO}_x$  emissions are comparable to other RQL type combustors, but the CO emissions are still too high except for lean global equivalence ratios.

It was found that increasing the global equivalence ratio decreased  $\text{NO}_x$  emissions due to a depletion of oxygen and lower temperatures for both combustors. Increasing the pressure in the annular type combustor increased  $\text{NO}_x$  emissions. Increasing the operating pressure in the can type combustor had little effect on  $\text{NO}_x$  from an equivalence ratio of 0.6 to 0.9 because most of the volume in the can type combustor is fuel-rich. At an equivalence ratio of 0.5, the  $\text{NO}_x$  emissions grew with pressure because the increase in

pressure made the primary zone close to stoichiometric conditions, which raised the temperature of the primary zone.

It is recommended that the design of both combustors be further refined via CFD calculations prior to experimental work. Specifically, three design modifications should be considered. The first modification is adjusting the flow of the secondary jets so that they strengthen the recirculation region in the primary zone to trap the vaporized fuel there. The equivalence ratio within the primary zone should not fall below 1.3 or else the  $\text{NO}_x$  emissions will increase rapidly. The second design modification has to do with the dilution zone. The cooling air in the dilution zone cannot penetrate deep into the main core. As a result, the SUE contains no quick-quench step. The air must be admitted in such way that the rich combustion gases are brought to lean conditions as fast as possible. This can be done by changing the angle of the cooling vanes, or completely eliminating the cooling vanes all together. The final design modification is to shorten the length of the annular combustor. Its length is far too great to be used in aircraft.

A question arises whether or not the SUE combustor is a viable alternative to combustors which utilize swirlers. The answer is it is too early to tell. The above recommendations must be implemented tested first before such a question can be answered.



## REFERENCES

- [1] R. Puster, M. Egoavil, P. Gregory, D. Moslemian, "A Gas Turbine Combustor With a Double Step Combustor and a Captured Vortex Chamber," *AIAA*, 2009-1251.
- [2] ANSYS, Inc. (2012) ANSYS FLUENT Theory Guide.
- [3] S. Kamnis, S. Gu, "3-D modelling of kerosene-fuelledHVOF thermal spray gun," *Chemical Engineering Science*, 2006.
- [4] S. Pope, *Turbulent Flows*. Cambridge University Press, 2000.
- [5] H. Tennekes, L. Lumley, *A First Course in Turbulence*. The MIT Press, 1972.
- [6] D. Wilcox, *Turbulence Modeling for CFD*. DWC Industries, 2006.
- [7] R. E. Malacki, C. M. Rhie, R. G. McKinney, "Application of an Advanced CFD-Based Analysis System to the PW6000 Combustor to Optimize Exit Temperature Distribution- Part 1: Description and Validation of the Analysis Tool," *ASME Turbo Expo*, 2001.
- [8] M. Talpallikar, M. Lai, J. Holdeman. "CFD Analysis of Jet Mixing in Low NO<sub>x</sub> Flametube Combustors," *NASA Technical Memorandum*, 1991.
- [9] A. Frassoldati , A. Cuoci , T. Faravelli, "Experimental and Modeling Study of a Low NO<sub>x</sub> Combustor for Aero-EngineTurbofan," *Combustion Science and Technology*, 2010.
- [10] ANSYS, Inc. (2012) ANSYS FLUENT Best Practice: Scale-Resolving Simulations in ANSYS CFD.

- [11] ANSYS, Inc. (2010) ANSYS FLUENT Best Practices for Large Eddy Simulations (LES) in ANSYS FLUENT.
- [12] S. Turns, *An Introduction to Combustion: Concepts and Applications*. McGraw-Hill, 2012.
- [13] J. Warnatz, U. Maas, R.W. Dibble, *Combustion: Physical and Chemical Fundamentals, Modeling and Simulation, Experiments, Pollutant Formation*. Springer, 2010.
- [14] T. Poinso, D. Veynante, *Theoretical and Numerical Combustion*. Edwards, 2005.
- [15] P. Hill, C. Peterson, *Mechanics and Thermodynamics of Propulsion*. Prentice Hall, 1991.
- [16] N. Peters, *Turbulent Combustion*. Cambridge University Press, 2000.
- [17] ANSYS, Inc. (2012) ANSYS FLUENT User's Guide.
- [18] Y. R. Sivathanu and G. M. Faeth, "Generalized State Relationships for Scalar Properties in Non-Premixed Hydrocarbon/Air Flames," *Combustion and Flame*. 82. 211–230, 1990.
- [19] K. Kuo, R. Acharya, *Fundamentals of Turbulent and Multiphase Combustion*. Wiley & Sons, 2012.
- [20] A. Lefebvre, *Atomization and Sprays*. Taylor & Francis, 1989.
- [21] L. Opfer, I. V. Roisman, C. Tropea, "Primary Atomization in an Airblast Gas Turbine Atomizer," *Springer*, 2012.
- [22] S. A. Morsi and A. J. Alexander, "An Investigation of Particle Trajectories in Two-Phase Flow Systems," *J. Fluid Mech.*. 55(2). 193–208. September 26 1972.

- [23] M. Bidi, R. Hosseini, M.R.H. Nobari,” Numerical analysis of methane–air combustion considering radiation effect,” *Energy Conversion and Management*, 2008.
- [24] H. Versteeg, *An Introduction to Computational Fluid Dynamics: The Finite Volume Method*. Prentice Hall, 2007.
- [25] Y. Cengel, *Heat and Mass Transfer: A Practical Approach*. McGraw-Hill, 2007.
- [26] M. Modest, *Radiative Heat Transfer*. Academic Press, 2003.
- [27] C. Baukal. *The John Zink Combustion Handbook*. CRC Press, 2001.
- [28] A. Lefebvre, D. Ballal, *Gas Turbine Combustion: Alternative Fuels and Emissions*. CRC Press, 2010.
- [29] H. Saravanamuttoo, *Gas Turbine Theory*. Prentice Hall, 2009.
- [30] T. Blacha, M. Di Domenico, M. Rachner, “Modeling of Soot and NO<sub>x</sub> in a Full Scale Turbine Engine Combustor with Detailed Chemistry,” *Proceedings of ASME Turbo Expo*, 2011
- [31] R. Flack, *Fundamentals of Jet Propulsion with Applications*, Cambridge University Press, 2005.
- [32] D. Dewanji, “Flow Characteristics in Lean Direct Injection Combustors,” Birla Institute of Technology, India Master’s Thesis 2012
- [33] T. J. Rosfjord. “Evaluation of synthetic fuel character effects on rich-lean stationary gas turbine combustion systems. Vol. 1: Subscale test program,” *Technical Report AP-2822, Electric Power Research Institute*, Feb. 1981.
- [34] U.S. Hussain, G.E. Andrews, W.G. Cheung, A.R. Shahabadi. “Low NO<sub>x</sub> Primary Zones Using Jet Mixing Shear Layer Combustion,” *ASME*, 1988

- [35] R. Tacina, "Low NO<sub>x</sub> potential of gas turbine engines," *AIAA Paper 90-0550*, 1990.
- [36] T. Valachovic, "Numerical Power Emissions of Idle Power Emissions from Gas Turbine Combustors," *ASME*, 1993.
- [37] J. Meisl, R. Koch, R. Kneer, "Study of NO<sub>x</sub> Emission Characteristics in Pressurized Staged Combustor Concepts," *Twenty-Fifth Symposium on Combustion*, 1994
- [38] A. Datta, S. Som. "Combustion and emission characteristics in a gas turbine combustor at different pressure and swirl conditions," *Applied Thermal Engineering*, 1998.
- [39] N. Zarzalas, T. Ripplinger, S. Hohmann. "Low-NO<sub>x</sub> Combustor Development pursued within the scope of the Engine 3E German national research program in a cooperative effort among engine Manufacturer MTU, University of Karlsruhe and DLR German Aerospace Research Center," *Aerospace Science and Technology*, 2002
- [40] R. Tacina, C. Wey, P. Laing, and A. Mansour, "A low NO<sub>x</sub> lean-direct injection, multipoint integrated module combustor concept for advanced aircraft gas turbines," Technical Report NASA/TM2002-211347, NASA, 2002.
- [41] R. Bank, T. Schilling, "Development of an Ultra-Low NO<sub>x</sub> LP(P) Burner," *ASME Turbo Expo*, 2004.
- [42] D. Straub, K. Casleton, R. Lewis. "Assessment of Rich-Burn, Quick-Mix, Lean-Burn Trapped Vortex Combustor for Stationary Gas Turbines," *ASME*, 2005
- [43] N. Patel, M. Kirtas, V. Sankaran. "Simulation of spray combustion in a lean-direct injection combustor," *Proceedings of the Combustion Institute*, 2007

- [44] T. Yamamoto, K. Shimodaira, Y. Kurosawa, “Combustion Characteristics of Fuel staged Combustor for Aeroengines at LTO Cycle Conditions,” *ASME Turbo Expo*, 2011